Design, Modeling and Control of a Lightweight 3D Printed Fixed Wing VTOL UAV

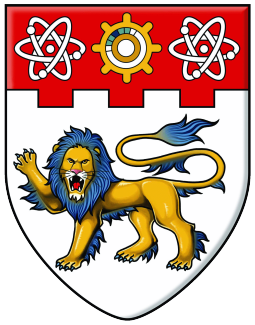

NANYANG TECHNOLOGICAL UNIVERSITY

YUNUS GOVDELI

School of Mechanical and Aerospace Engineering

A thesis submitted to Nanyang Technological University
in the partial fulfillment of the requirements for the degree of

Doctor of Philosophy

2020

Abstract

This thesis covers topics in additive manufacturing (AM), dynamic modeling and control of fixed-wing vertical take-off and landing unmanned aerial vehicles (VTOL UAVs). For AM, a guideline for AM of aircraft wings is developed. Two design methodologies were considered, namely a conventional design using ribs-spar-skin and an unconventional design using skin-periodic cellular structures. For a conventional rib-spar structure, the effects of skin thickness, number of ribs, additive building as well as printing orientations on the wing strength and weight are investigated. Among the obtained wing structures, the best performing wing configuration, i.e., a combination of number of ribs, skin thickness, printing and building orientations, is selected based on weight and strength. This selected structure is manufactured and tested. To exploit the design freedom provided by AM, periodic cellular structures were investigated. The bending stiffness was experimentally tested for diamond honeycomb and 3D-Kagome structures with various infill rates and truss diameters. The experimental results favored honeycomb structures and hence a second wing model was manufactured and compared to the conventional manufacturing model. The benefit of periodic cellular structures achievable by AM was the reduction of weight of 35%.

For mathematical modeling of fixed-wing VTOL UAV dynamics, the aerodynamic forces are modeled using two techniques. In the first technique, a tilt-rotor flying wing is modeled using the quasi-steady approximation where the aerodynamic forces are calculated from DATCOM and CFD data. This implies that a linearization technique is implemented for the controller via gain scheduling. Considering the different characteristics of the vehicle with increasing rotor tilting angles, the transition flight between the level flight and hovering phases is linearized at 10° intervals. For each linear model, linear controllers are designed by minimizing a cost function based on attitude and position error. To enhance the model further, a thrust model was implemented to account for the propeller wake over the flying wing surfaces. In the second technique, an unsteady aerodynamic model is presented for two quad-

plane models, a tilt-rotor and a pusher, to account for the unsteady forces generated by acceleration of the vehicle. In this model, a gain scheduling is not needed as the controller is applied to the nonlinear dynamics of the vehicle. It is observed that the unsteady model is able to represent the transient forces at the start and end of transition flight as well as in the cases of disturbances.

The performance of the linear controllers designed is compared with a type-2 fuzzy neural network (T2FNN) based controller for level flight under disturbances, where the T2FNN based controller learns the effects of disturbances over time and reduces the tracking error. First, this is implemented for the flying wing vehicle configuration. To reduce the oscillations while switching from one controller to the other during transition flight, the tilting rate is manipulated by a fuzzy switching algorithm. When compared to a fixed tilting rate, the fuzzy algorithm reduces the total tracking error by 45.2%. Second, the T2FNN based controller is implemented for the quadplane configuration. Under disturbances, the altitude change during transition flight is reduced by 34.16% when compared to the PID controlled case. Finally, for the sake of completeness, full flight envelope control results for both quadplane configurations are presented. The results indicate that the altitude hold during transition is more challenging for the tilt-rotor configuration compared to the pusher configuration.

Acknowledgements

I would like to express my sincerest gratitude to my advisor Professor Basman Elhadidi for his guidance and instruction during my doctoral study. In the time of being his student, I have learned many different aspects of aerodynamics, aircraft control and design, but, most importantly, he has changed my understanding of research and helped me to develop a new way of thinking and attitude toward academics. I am also grateful for his patience and support during hard times. He has always been approachable, especially when I did not know where to look for a solution. I deeply appreciate his enthusiasm, knowledge, and experience which helped me to receive constructive feedback and suggestions.

Secondly, I would like to thank my co-supervisor Associate Professor Erdal Kayacan for showing me different subjects of graduate level research. I appreciate his efforts and motivation to improve the publicity of my work. Also, I am grateful Dr. Chen Songlin for his valuable suggestions at the beginning of my study in NTU.

Thirdly, I would like to thank Singapore Centre for 3D Printing (SC3DP) for their support and giving me the opportunity to conduct my research. Without their support, I would not be able to be a part of such a high quality research environment.

Last but not least, I would like to express my heartfelt appreciation to my wife, my parents, my brother and my friends for being supportive, encouraging and patient during my studies.

Statement of Originality

I hereby certify that the work embodied in this thesis is the result of original research, is free of plagiarised materials, and has not been submitted for a higher degree to any other University or Institution.

23 August 2019

. . . . . .
Date

. . . . . .
Yunus Govdeli

Supervisor Declaration Statement

I have reviewed the content and presentation style of this thesis and declare it is free of plagiarism and of sufficient grammatical clarity to be examined. To the best of my knowledge, the research and writing are those of the candidate except as acknowledged in the Author Attribution Statement. I confirm that the investigations were conducted in accord with the ethics policies and integrity standards of Nanyang Technological University and that the research data are presented honestly and without prejudice.

23 August 2019

. . . . . .

Date

Dr. Basman Elhadidi

Authorship Attribution Statement

This thesis contains material from 6 papers published or under review in the following peer-reviewed journals and from papers accepted at conferences in which I am listed as an author.

Chapter 3 has material from the paper published as Suraj Ravindrababu, Yunus Govdeli, Zhuo Wei Wong, and Erdal Kayacan, "Evaluation of the Influence of Build and Print Orientations of Unmanned Aerial Vehicle Parts Fabricated Using Fused Deposition Modeling Process", Journal of Manufacturing Processes, vol. 34, Part A, pp. 659-666, August 2018.

The contributions of the co-authors are as follows:

- I prepared the manuscript drafts with our research associate Suraj Ravindrababu. The manuscript was revised by Dr Erdal Kayacan.
- I co-designed the study with our research associate Suraj Ravindrababu and performed the laboratory work at the School of Mechanical and Aerospace Engineering with him together. Therefore, I claim equal contribution to the paper with him.
- I designed the UAV model in the paper, provided the aerodynamic load distribution and the point masses on the body.
- Zhuo Wei Wong was responsible for the categorization of collected data for Anova analysis in the paper.
- The graphic work was enhanced by Suraj Ravindrababu for a better visual representation of the layer arrangement issues.

Chapter 3 has material from the conference paper published as Jing Ming Low, Yunus Govdeli, Suraj Ravindrababu and Erdal Kayacan, "On The Comparison of Diamond Honeycomb and 3D-Kagome Structures for 3D Printed UAVS", 3rd International Conference on Progress in AM (Pro-AM 2018), pp. 341-346, Singapore, May 15-17, 2018.

The contributions of the co-authors are as follows:

- I prepared the manuscript drafts with our final year project student Low Jing Ming. The manuscript was revised by me and Dr Erdal Kayacan.
- I co-designed the study with our research associate Suraj Ravindrababu.
- All the experimental work is conducted by Low Jing Ming and me together as I was his mentor for his final year project. Therefore, I claim equal contribution to the paper with him.
- The implementation of the collected data, their analysis is carried out by me.
- For repetitive/iterative tasks, Low Jing Ming helped as far as his project is concerned.

Chapter 4 and 6 have material from the conference paper published as Yunus Govdeli, Sheikh Moheed Bin Muzaffar, Raj Raunak, Basman Elhadidi and Erdal Kayacan, "Learning Control of a Tandem-Wing Tilt-rotor UAV with an Unsteady Aerodynamic Model", IEEE International Conference on Fuzzy Systems (FUZZ-IEEE 2019), 2019.

The contributions of the co-authors are as follows:

- The paper writing procedure is supervised by Dr. Basman Elhadidi.
- I wrote the drafts of the manuscript. The manuscript was revised together with Dr. Basman Elhadidi and Dr Erdal Kayacan.
- Sheikh Moheed Bin Muzaffar and Raj Raunak helped with obtaining the trim conditions for the vehicle and providing the initial layout for the simulations.
- For visualizations, Sheikh Moheed Bin Muzaffar helped with the drawings.
- I conducted the simulations with the proposed controllers. I collected the data, implemented the disturbance rejection simulations.
- I analyzed the whole data and noted down the conclusions.

Chapter 4 and 6 have material from the paper under review as Yunus Govdeli, Sheikh Moheed Bin Muzaffar, Raunak Raj, Basman Elhadidi, Erdal Kayacan, "Unsteady Aerodynamic Modeling and Control of Pusher and Tilt-Rotor Quadplane Configurations", Aerospace Science and Technology (submitted).

The contributions of the co-authors are as follows:

- The paper writing procedure is supervised by Dr. Basman Elhadidi.
- I wrote the drafts of the manuscript. The manuscript was revised together with Dr. Basman Elhadidi.
- Sheikh Moheed Bin Muzaffar and Raj Raunak helped with obtaining the initial results.
- After the initial results, I conducted the whole simulations, made the comparisons between the two configurations in the paper.
- I collected the data, developed the autopilot with Dr. Basman Elhadidi's suggestions.
- I analyzed the whole data and noted down the conclusions under Dr. Basman Elhadidi's supervision.

Chapter 4 and 6 have material from the paper under review as Yunus Govdeli, Raunak Raj, Sheikh Moheed Bin Muzaffar, Basman Elhadidi, Erdal Kayacan, "Learning Control and Safe Transition for Fixed-Wing VTOL Vehicles", Aerospace Science and Technology (submitted).

The contributions of the co-authors are as follows:

- The paper writing procedure is supervised by Dr. Erdal Kayacan.
- I wrote the drafts of the manuscript.
- Since the model is developed in the earlier study together with Raunak Raj and Sheikh Moheed bin Muzaffar, they are listed as authors. They did not have any other contribution to this paper.
- I conducted the whole simulations, made the comparisons between the two nominal and perturbed conditions.
- I collected the data with the learning controller, showed its performance with respect to the conventional controllers.
- I analyzed the whole data and noted down the conclusions.

Chapter 4 and 5 have material from the from the conference paper published as Yunus Govdeli, Anh Tuan Tran, and Erdal Kayacan, "Multiple Modeling and Fuzzy Switching Control of Fixed-Wing VTOL Tilt-Rotor UAV", IFSA - NAFIPS 2019 2019 IFSA World Congress and NAFIPS Annual Conference, 2019.

The contributions of the co-authors are as follows:

- The paper writing procedure is supervised by Dr. Erdal Kayacan.
- I wrote the drafts of the manuscript.
- Dr. Anh Tuan guided me throughout the project. He taught me how to approach the optimization problem for gain selections and provided a template to work on. I asked my questions to him whenever I had doubts.
- I conducted the whole simulations, designed the gain-scheduling controllers, wrote the carrot-chasing algorithms.
- I carried out the CFD analyses for modeling in the paper.
- I collected the data with the learning controller, showed its performance with respect to the conventional controllers.
- I analyzed the whole data and noted down the conclusions.

23 August 2019

. . . . . .
Date

. . . . . .
Yunus Govdeli

Table of Contents

List of Tables

List of Figures

List of Publications

Journal Papers

– Suraj Ravindrababu, Yunus Govdeli, Zhuo Wei Wong, and Erdal Kayacan, "Evaluation of the Influence of Build and Print Orientations of Unmanned Aerial Vehicle Parts Fabricated Using Fused Deposition Modeling Process", **Journal of Manufacturing Processes**, vol. 34, Part A, pp. 659-666, August 2018.

– Yunus Gövdeli, Sheikh Moheed Bin Muzaffar, Raunak Raj, Basman Elhadidi, Erdal Kayacan, "Unsteady Aerodynamic Modeling and Control of Pusher and Tilt-Rotor Quadplane Configurations", Aerospace Science and Technology (submitted).

– Yunus Gövdeli, Raunak Raj, Sheikh Moheed Bin Muzaffar, Basman Elhadidi, Erdal Kayacan, "Learning Control and Safe Transition for Fixed-Wing VTOL Vehicles", Aerospace Science and Technology (submitted).

Conference Papers

– Yunus Govdeli, Anh Tuan Tran, and Erdal Kayacan, "Multiple Modeling and Fuzzy Switching Control of Fixed-Wing VTOL Tilt-Rotor UAV", **IFSA - NAFIPS 2019 2019 IFSA World Congress and NAFIPS Annual Conference**, 2019.

– Yunus Govdeli, Sheikh Moheed Bin Muzaffar, Raj Raunak, Basman Elhadidi and Erdal Kayacan, "Learning Control of a Tandem-Wing Tilt-rotor UAV with an Unsteady Aerodynamic Model", **IEEE International Conference on Fuzzy Systems (FUZZ-IEEE 2019)**, 2019.

– Jing Ming Low, Yunus Govdeli, Suraj Ravindrababu and Erdal Kayacan, "On The Comparison of Diamond Honeycomb and 3D-Kagome Structures for 3D Printed UAVS", **3rd International Conference on Progress in AM (Pro-AM 2018)**, pp. 341-346, Singapore, May 15-17, 2018.

Other Papers

– Zi Quan Gerard Ong, Yunus Govdeli, Suraj Ravindrababu and Erdal Kayacan, "Feasibility Studies of Postprocessing Techniques to Strenghten 3D Printed UAV Wing Structures", **3rd International Conference on Progress in AM (Pro-AM 2018)** , pp.244-249, Singapore, May 15-17, 2018.

– Yunus Govdeli, Zhuo Wei Wong, Erdal Kayacan. "Additive Manufacturing of Unmanned Aerial Vehicles: Current Status, Recent Advances, and Future Perspectives", **Proceedings of the 2nd International Conference on Progress in Additive Manufacturing**, 2016.

Chapter 1

Introduction

1.1 Background and Motivation

Recently, there has been a drastic paradigm shift of use of unmanned aerial vehicles (UAVs) from military operations to civilian and urban applications. In this context, one of the popular UAV applications is package delivery. When it comes to a delivery operation, accessibility of delivery location is a decisive factor. Figure 1.1a depicts a sample delivery vehicle where the main arrival point is on Pulau Ubin, Singapore. Delivering daily items from Singapore to such areas with ground vehicles would be problematic, whereas aerial delivery may be attractive. However, endurance of the aerial vehicle plays a critical role as it determines the range of the UAV. Therefore, conventional multirotors may not have sufficient flight endurance for long range applications and thus inspirational designs with wings such as in Fig. 1.1b will help to deliver items to wider ranges including the routes above seaways. It can be seen that the novel systems are not similar to classical multirotors or fixed–wing vehicles.

In addition to civilian applications, military missions, e.g. surveillance, may require the vehicle to remain airborne for longer duration. Besides, the ability to take–off and land vertically to a limited area such as on a ship would be of great advantage (see

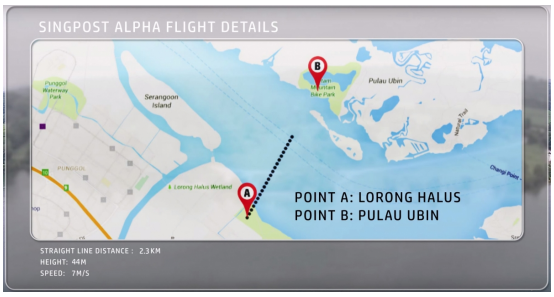

(a) A parcel delivery route by Singpost [1].

(b) DHL Delivery Drone [2].

Figure 1.1: UAV delivery applications.

Fig. 1.2). Therefore, VTOL UAVs may be a solution to the problem of endurance and lack of runway in military missions. From this perspective, achieving a successful transition flight without stalling between the two steady conditions is a requirement for these systems. Hence, this research is motivated by the need for understanding the transition flight dynamics as well as its control, especially under varying flight conditions.

Maintenance or replacement of damaged components of a UAV poses a challenge for operational success. Most UAV users do not have access to large machine shops or specialized equipment at the mission area. To this end, a study for the suitability of use of additive manufacturing (AM) is conducted. Since on-demand manufacturing is an option with AM, maintenance or repair work can be carried out when necessary, which allows for less amount of stock parts, especially for off-shore UAV applications. In this context, various means of manufacturing are examined for different parts to assess the weight-to-strength reductions.

1.2 Challenges

1. **Operational maintenance and ease of manufacturing.** Structural complexity is inevitable with added value and multi-functionality, increasing the cost of UAV production. Conventional UAV manufacturing methods, e.g. injection

Figure 1.2: Aerial vehicle landing on a ship [3].

molding for plastics, machining, drilling, lathe for metals, result in excessive usage of raw materials and are labor-intensive due to multiple manufacturing stages [4]. Besides, these methods limit the engineer to the available design approaches which hinder the design of unconventional and original multi-functional systems. An alternative to the traditional approaches is to employ composite materials such as carbon-fiber composites [5]. Due to their high strength to weight ratio, they are one of the most preferred materials for multi-rotor UAV structures. However, high material cost, multiple processing steps along with the limitations of carbon-fiber manufacturing are the biggest drawbacks of this kind of composites. Furthermore, critical design details such as internal structures of wings cannot be accomplished in this method of fabrication.

AM has an advantage due to its free-form fabrication ability. Firstly, it is a layer-by-layer manufacturing technique. This enables the designers to manufacture intricate structures which may not be achievable with conventional manufacturing techniques [6]. Secondly, it does not require multiple steps to cast, mold or to apply any manufacturing process for additional product details. Furthermore, any necessary design modification is executed on the CAD file without a need for a change on the manufacturing line. In summary, along with on-demand manufacturing option, this leads to less labor demand and much shorter manufacturing

time when compared to conventional manufacturing processes. Therefore, AM is a promising candidate to cut-down the production costs for multi-functional, intricate products for novel UAVs.

2. **Aerodynamic modeling of transition flight.** The flight regime of a hybrid UAV consists of multiple stages including vertical take-off, hover, transition from hover to steady level flight, backward transition from steady level flight to hover, and landing. Mathematical modeling of hybrid UAVs is another point of discussion. In this thesis, the discussion focuses on the convertiplane UAVs, where the aircraft motion is not only limited to low angles of attack and linear aerodynamics but also extends to the nonlinear aerodynamics behind the propeller stream [7]. In addition, switching from hovering to level flight and vice versa result in sudden changes in aerodynamic forces and moments. The significance of this rapid change should also be evaluated in the context of unsteady and quasi-steady aerodynamics [8, 9].

3. **Transition control.** Apart from the modeling problem, another aspect of transition flight is the control between the two flight modes. In most cases, transition flight modeling is avoided and it is carried out in a simplified manner, where the controllers are tuned for level flight and hovering. However, the method of transition, e.g. altitude holding, rapid transitioning and available control inputs define the trajectory followed by the vehicle [10, 11] Therefore, transition flight control is a motivating research problem. To this end, full flight control of hybrid UAVs under disturbances such as wind gusts or rotor malfunctioning should be addressed. In this context, efficiency of conventional PID controllers with respect to advanced controllers can be discussed.

1.3 Objectives and Contributions

1. **To develop a design methodology for AM of UAVs and develop an approach to reduce structural weight.** As the printable thermoplastic materials have low specific strength, traditional design processes need to be tested and checked for their applicability. In the cases where they are unsatisfactory, new methods should be evaluated and proposed for designing with AM.

   To identify the design requirements imposed by AM, material characterization studies with American Society for Testing and Materials (ASTM) standard specimens are conducted. The critical parameters affecting the structural integrity and weight are determined. As a result of the analyses, diamond honeycomb structures are found to be useful for wing structures with minimal skin thickness. To the best of our knowledge, this is the first time that a design methodology for AM of UAVs with both conventional and unconventional structures are proposed.

2. **To characterize the aerodynamic characteristics of the system in order to have a reliable simulation.** Hybrid vehicles have various configurations. Depending on the configuration selection, aerodynamic models vary. Therefore, an appropriate aerodynamic model should be selected and tested for accuracy as this model will be used for motion control.

3. **To model the transition flight.** Transition flight is the most challenging phase of a hybrid vehicle. As will be reflected in the literature review in detail, in most of the applications, this phase is completed quickly and lacks sufficient modeling as the aerodynamic forces are transient and usually neglected.

   Transition from hover to forward flight is a flight phase in which propeller thrust is replaced with the lift generated from the wings to remain airborne. This change is very rapid and significant, especially at the beginning of the transition motion.

To the best of our knowledge, this is the first time that an unsteady aerodynamic model is developed for the transition flight of hybrid vehicles.

4. **Implementation of a mission profile via an autopilot.** An autopilot that can account for a complete transition including aerodynamic disturbances is a challenge.

   (a) **A complete control over the transition regime and a fuzzy switching algorithm for smoother transition.** Multiple models covering the transition regime is designed and gain-scheduled controllers are implemented. For modeling, a fuzzy logic based algorithm is proposed, which reduces the oscillations during transition flight by manipulating the transition speed.

   (b) **The development of a control framework for transition period.** An intelligent controller capable of learning the changes in the dynamics of the motion is implemented and tested with the designed mathematical models of hybrid UAVs. The basic structure of the controller consists of a type-2 fuzzy neural network (T2FNN) and a PD controller, where the learning is carried out by the neural network and the PD controller is employed to keep the vehicle stable. The details of this controller structure and its performance under disturbances are discussed and compared with conventional controllers. It is shown that the proposed controller outperforms its counterpart under disturbances during transitions.

1.4 Thesis Layout

The motivation of the research, challenges, objectives, and contributions are defined in **Chapter 1**. The organization of other chapters is as follows.

Chapter 2 includes the literature review of the suitable AM techniques, candidate wing structures, quasi-steady and unsteady aerodynamic modeling as well as the model–

free/model–based control approaches.

Chapter 3 introduces AM system design with conventional methods, its model, manufacturing and analysis of its parameters. Further, to exploit the advantages of AM, intricate 3D-Kagome and honeycomb structures are explored and tested as internal structures for wings.

Chapter 4 includes the equations of motion, quasiy-steady and unsteady aerodynamic modeling methods for flying wing and quadplane configurations, respectively.

Chapter 5 includes an application of the quasi–steady aerodynamic model with multiple linear models and gain–scheduling control. The performance of a fuzzy switching algorithm is compared with a constant–speed transition method.

Chapter 6 includes the implementation of an unsteady aerodynamic model for transition flight of quadplane vehicles. A T2FNN-based learning controller, which is proposed for improved transition flight under disturbances, is implemented and the corresponding control results for the full flight envelope are highlighted.

Chapter 7 presents the conclusion of this research along with several future directions and recommendations.

Appendix A includes the design of the 3D printed model using XFLR5 along with its static and dynamic characteristics.

Appendix B includes the wind tunnel tests carried out to determine aerodynamic characteristics of the 3D printed model.

Appendix C includes the CFD analyses conducted to review the accuracy of the XFLR5 results.

Chapter 2

Literature Review

2.1 UAV Design Configurations

Over the past two decades, the interest in UAV has increased rapidly since they serve for the missions which can be dull, dangerous or harmful to humans, and the number of commercially available UAVs for both military and civilian purposes keeps growing. Numerous UAV applications such as 3D mapping, intelligence-surveillance-reconnaissance, border patrol and security missions, precision agriculture, parcel-delivery and first-aid practices are currently available in the market. The versatile use of UAVs increases the significance of their practicality and multi-functionality. Clearly, selection of a pertinent UAV configuration depends on the application. In this context, from the flight dynamics point of view, UAVs can be classified into two main categories: rotary wing (multirotor), and fixed–wing UAVs [12]. The main difference between these two classes is the approach to the generation of the lift force. With embodying the vertical take-off, landing, and hovering capabilities, rotary wing aircraft are able to perform their missions on challenging areas without requiring runways. Also, having redundant rotors can enable fault tolerance capability in which the system can continue functioning in case of a rotor system failure [13] (see Fig. 2.1). Nevertheless, they have a limited

(a) (b)

Figure 2.1: A sample quadrotor (a) and its coaxial counterpart (b).

endurance due to the excessive energy consumption to produce the necessary lift. On the other hand, fixed–wing aircraft have longer endurance at higher speeds and cover larger areas for surveillance. However, they cannot hover like multirotor UAVs and need consistent forward flight speed to generate lift force from wings. Thus, hybrid UAVs, which combine the capabilities of a multirotor and a fixed–wing UAV, can benefit from both designs. Despite an upsurge in the design complexity, hybrid UAVs emerge as a valuable concept providing VTOL, hover, and forward flight qualities simultaneously while keeping operational assets such as endurance, range and practicality. Several hybrid UAV design configurations such as quadplanes, tailsitter and tilt systems are currently available.

Quadplanes are the simplest method of obtaining VTOL feature with a fixed–wing system by attaching vertically–positioned rotors along with a thruster on the aircraft fuselage line [14]. Basically, it is a direct combination of a multirotor with the fixed–wing vehicle. The control problem of this setup is simpler; however, it has added weight and drag by the extra rotors.

Tailsitters enable a simple form of transition from hover to forward flight by only changing the pitch angle. Due to embodying fixed–positioned rotors, these systems drastically decrease mechanical complexity. However, tailsitter systems are not robust against disturbances due to the direct exposure of the whole body to cross-wind in the

air [15].

Tilted Systems apply thrust vectoring to create forces on various directions. When it is applied with an aerodynamic surface, it provides additional force particularly on horizontal axis [16]. There are two main concepts: (i) rotor tilting; (ii) tilting of rotor–wing system. While the former is exposed to more downwash effect, control of the tilting motion of the latter one is more challenging as the whole wing mechanism needs to be rotated which results in an instantaneous change of angle of attack of the aircraft wing (see Fig. 2.2).

(a) (b) (c)

Figure 2.2: A sample quadplane (a), a tailsitter (b) and a tilt-wing (c).

2.2 Design Loads and Conventional Structure Components

All unmanned vehicles are exposed to static and dynamic loads during different phases of a mission. The magnitude and distribution of these loads are critical for a vehicle design. The maximum and minimum loads at a flight envelope are shown by the V-n diagram, where V is the flight speed and n is the ratio of aerodynamic lift to vehicle weight. A designed model should be capable of withstanding these loads on this diagram. Dynamic loads during maneuvers actually shape the boundaries on a V-n diagram, which define the strength limits of an airframe. Before proceeding to airframes producible with AM, conventional structures should be explored, which have evolved over time from heavy metal trusses to monocoque and semi-monocoque structures (see

Fig. 2.3). Most early aircraft used Pratt or Warren trusses to form the fuselage, which were heavy and soon replaced by the monocoque and semi-monocoque designs. In a monocoque, stressed-skin structure, the skin is the primary load bearing member of an airframe, in which thin shells of material are "wrapped" around the fuselage frames. In a semi-monocoque, the skin is not the only load bearing member. It is mainly supported by ribs, spars, stiffeners and other longitudinal and transverse internal support structures, which help the loads to be distributed depending on the support member orientation. Most modern vehicles manufactured via conventional techniques utilize this method. Accordingly, materials used in aerospace applications have high specific stiffness. However, material types also differ with respect to the vehicle size and use. In most cases, large aircraft has (i) orders of magnitude of development costs, (ii) structural complexity imposed by fuselage pressurization, (iii) much powerful propulsion methods, (iv) different rankings of design objectives and safety concerns when compared to small scale aerial vehicles [17]. Thus, unlike large scale aircraft, there are numerous material alternatives for small scale vehicles ranging from plywood, fiberglass to Al alloys and composites with conventional manufacturing. Common materials used for airframes are tabulated in Table 2.1.

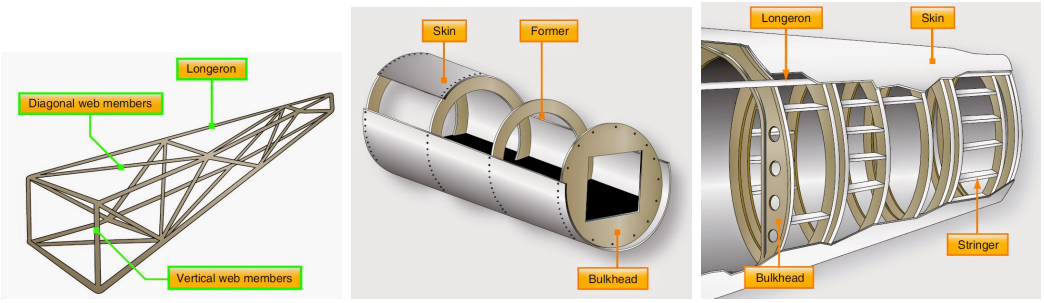

(a) (b) (c)

Figure 2.3: A sample truss (a), a monocoque (b) and a semi-monocoque (c), adapted from [18].

Table 2.1: Common materials used for airframes [17, 19].

Structure Type	**Materials**
Pratt and Warren trusses	wooden or steel tubes or beams
Monocoque	initially, molded plywood skin; later, fiberglass enhanced with polyester/epoxy resin
Semi-monocoque	*large aircraft:* aluminum-alloy sheets joined by rivets as skin, and Al or composite materials as load-bearing elements; *smaller aircraft:* foam cladded with thin glass-/carbon-fiber-reinforced tissue as skin, carbon-fiber-reinforced tubes as load-bearing elements, occasionally, plywood as ribs

2.3 Additive Manufacturing

AM is initially utilized as a prototyping tool. As prototyping helps a designer to rectify dimensional inaccuracies, structural deficiencies or conceptual design problems while showing most of the features of the final product, it is an indispensable component of the product development chain [6]. In this context, AM provided fast and rapid models due to its convenient general procedure and also benefited in the tooling industry. With the development of material and machine performances, the new trend in AM is to apply it for final products with targeting to cut down the manufacturing cost and duration. One of the major advantages of AM is the manufacturing duration and cost for intricate and complex structures. AM requires less number of manufacturing steps while, in most cases, eliminating the need for tools and reducing scrap materials [20]. Therefore, the efforts are focused in lattice structures, which are challenging to form with conventional manufacturing.

The most dominant feature of AM is that the only necessary item in the design stage is an accurate solid surface model of the object [21], which shortens the design phase of product development process when compared to subtractive or formative methods. However, this also requires a thorough evaluation of any design as any faulty process

affects the whole model, especially when the intricacy and complexity increase. Nevertheless, the rectifications are directly carried out on the CAD file without a need of molds, which makes AM advantageous for low volume manufacturing. The main limitation is that all AM techniques are constrained in size, which leads to multiple parts for a product. Large-scale modeling with AM is therefore an unsolved engineering problem. Besides, most of the AM methods require various strategies for post processing, which also affects the part quality. For UAV applications, surface roughness of wings has direct effect on lift and drag generation, hence should be considered for when AM is used as a means of manufacturing.

2.3.1 AM Structures

Lattice structures are sandwich structures with periodic cellular core construction. They have several advantages, such as lightweight and high stiffness/strength-to-weight ratio properties, which makes them preferable in aerospace and automotive industries. Among high-strength lightweight structures, honeycombs, foams, and truss lattices stand out.

Topology optimization is a mathematical approach to achieve an optimized distribution of material on any structure, such as the wing in [23]. Optimizations are generally carried out at part-level, e.g., aerospace brackets [24]. Although computationally expensive, this technique allows for achieving maximum stiffness with a minimum weight.

Bio-mimicking structures are used for producing optimal geometries by mimicking the nature. Considering airframes, resistance to the aerodynamic forces on a wing is of high significance. In this case, designs inspired by the nature reduce the excessive material use while keeping structural efficiency [26]. The proper selection of bio-inpired shapes may help UAV wings to have high stiffness with the least amount of material [27].

Infill modification approach makes use of the inbuilt function of a 3D printer by

modifying the amount of printing infill for a structure. Experiments are based on the adjustment of infill density, pattern and orientation to obtain the UAV structures with the required stiffness and minimum weight [28]. By infill reduction, material usage is reduced. However, the reduction in this approach is generally uniform which results in a decrease in strength all over the structure [29].

2.3.2 Periodic Cellular Structures

Cellular structures consisting of periodic geometries are a promising class of high-performance structures. They can be classified as 2D and 3D solid structures whereas 2D cellular solids include honeycomb structures with various core shapes. Studies show that honeycombs are lightweight structures with high energy absorption capabilities [67], superior in-plane stiffness than other periodic cellular structures [68] with a high fracture toughness, which can help prevent crack propagation in 3D printed systems. Depending on the core shape, the properties of the honeycomb structure vary significantly. In Fig. 2.4, the comparisons of elastic and shear moduli between several core shapes are presented. The diamond core shape is the most consistent core type for both elastic and shear behaviors. Besides, its shape is more printing-friendly due to the angles between its lines as removal of support material is also challenging when placed in-between the unit cells. In this context, the diamond core shape outperforms its counterparts.

3D cellular structures can be classified into lattice, syntactic porous and foam types [69]. There are two fundamental approaches of obtaining three-dimensional cellular structures. In the first approach, a 2D pattern is propagated along a horizontal plane and this pattern is extruded along the third dimension. Their structural properties are mainly affected by the 2D main core shape. In the second approach, a 3D object, also called a cellular solid, is repeated in a volume such that the structure consists of multiple polyhedral shapes. Figure 2.5 represents one example of 2D and 3D cellular

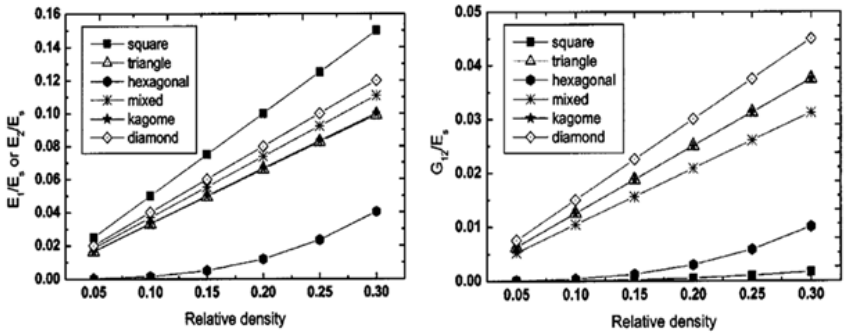

Figure 2.4: Effective Young Modulus vs Relative Density and Shear Modulus vs Relative Density [68].

structures, respectively [72]. It is highlighted in literature that single-layered Kagome lattice structures have superior strength, stiffness and stability properties than other lattice trusses [70]. Considering the necessity of the weight reduction for UAVs, Kagome lattice is an important candidate for UAV wings. In addition, Kagome lattice shows superior performance in energy absorption with high impact resistance [71], which can facilitate the durability of a 3D printed UAV during crashes.

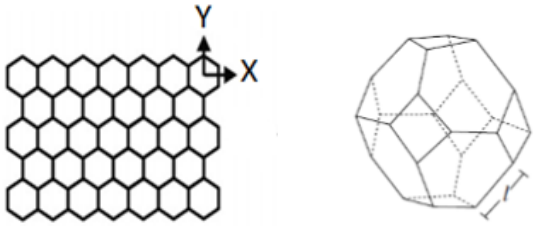

(a) (b)

Figure 2.5: A 2D hexagonal pattern (a) and a 3D thetrakaidecahedron (b) unit cell [69].

2.3.3 Evaluation of AM Methods for UAV Manufacturing

There are several techniques used for AM of UAVs. These can be summarized as

1. **Polyjet:** Multiple polymer jetting methods (MJM) are liquid-based AM techniques enabling parts to have much smoother surfaces with higher printing precision when

compared to any other techniques. Various lattices [22] and bio-mimicking structures, like bat or insect wings [30, 31] are constructed successfully with Polyjet. However, weight and low strength still remain as challenges for this technology. Besides, they are not able to withstand the fluctuating loads such as air flow or impact loads as in the case of a deep landing, which makes them incompatible for UAV structures [32].

2. **Stereolithography (SLA):** Since SLA printed parts lose a significant portion of their strength with time [33, 34] and require post-curing after support material removal, their use for building bulk structures such as wings or fuselage are limited. Instead, SLA is used for intricate but lightweight structures, e.g., ornithopter wings [35].

3. **Selective Laser Sintering (SLS):** SLS is widely exploited to manufacture UAV structures. The first UAV by SLS is an elliptic-wing spy aircraft from WWII with complicated internal structure running spirally along the body [36]. In other applications [37, 38], a fuel tank of a twin-body aircraft and a test vehicle body are manufactured via SLS. The materials utilized for SLS are generally various nylon types. Except for material density, the only drawback of SLS components are their high surface roughness, almost [39]. This sets a requirement for post-processing of the surface for better quality [6]. Nevertheless, the self-supporting mechanism is one of the most significant assets of SLS manufacturing since it eliminates the need for additional support material while the residual powder can be reused for upcoming manufacturing sessions.

4. **Fused Deposition Modeling (FDM):** FDM is a strong candidate for UAV structure manufacturing as it has fast reprinting ability. For example, 80% of the body of the first jet-powered AM aircraft and two other vehicles are constructed with FDM [22, 40]. One important parameter is the layer attachment quality, which determines the durability of an FDM printed part [41]. This is affected by the printing orientation as well as support types [42] and should be investigated before printing an aircraft frame. Cooling rate also decides on the dimensional accuracy of printed components,

which causes shrinkage or warping at the sharp edges and corners that reduce the reliability for mass airframe production [44]. Acommon approach is to support the printed parts by carbon frames or rods such as the flying wing aircraft in [45] and [46].

5. **Molten Metal Fusion:** This method shows much higher accuracy and strength compared to SLS printed parts as the voids between the powder grains are decreased drastically [47]. Hence, it is one of the most promising AM techniques providing this level of quality. The drawback is, however, the material density which increases the weight and thus reduces the applicability to lightweight aerospace structures.

6. **Electron Beam Melting (EBM):** EBM processes high quality metals and their alloys such as Ti alloys, Inconel and Cobalt. Due to the vacuumed printing room, non-uniformities on printed parts are cleared at a higher grade which helps to reduce the residual stresses [48]. Nevertheless, the powder grains are generally larger than SLM powders, decreasing the maximum achievable surface quality significantly. Also, material cost and printing room dimensions limit its use for lightweight aerial applications.

7. **Laminated Object Manufacturing (LOM):** The drawback of LOM is the dependence of the component strength on the adhesives used between the layers combining the structure. Therefore, component strength varies significantly along all three axes [50]. In addition, due to the loss of their lamination/sheet form, supporting cubes cannot be reused, either. In this context, it is an unfavorable method for airframe manufacturing.

A summary of the discussed candidate strategies is given in Table 2.2.

2.3.4 Decisive Parameters for Airframe Manufacturing with AM

Evaluating the general characteristics of AM techniques, some factors affecting the airframe manufacturing are:

1. **Strength-to-weight ratio:** The biggest limitation for AM of a UAV is the structural weight. Weight reduction is always desired as it increases endurance, enhances maneuverability and allows for a higher range of payloads. Plastic-based AM techniques generally utilize low strength-to-weight ratio thermoplastic materials, which results in bulky bodies [4]. With metal printing, desired strength could be achieved. However, the minimum printable thickness is high for lightweight aerial applications, leading to larger weight. This makes plastic-based methods more preferable.

2. **Homogeneity of material:** Strength of the component may be aligned and non-homogeneously distributed in the printed part [51, 52]. This concept will be discussed further in detail in Chapter 3.

3. **Support material:** Support removal affects the surface quality significantly. Wing surfaces of any aircraft should be smooth and clean. Therefore, removal of the break-away support structures from the outer mold shapes should be avoided as much as possible [53]. Alternatively, self-supporting AM techniques may be selected.

4. **Scale the vehicle and building volume:** Due to the limited printing volumes, the dimensions of a design has a substantial effect on which AM method to select for manufacturing. Most printed parts require joint mechanisms, fixtures or adhesives to assemble a larger functional part. Consequently, metal printing, where the build volume is limited, is generally preferred for manufacturing of smaller parts such as brackets; or they are used for specific applications such as spar bars, turbine blades [54] or engine chambers [55], which are already expensive with conventional manufacturing. For small scale UAVs, SLS and FDM allow for larger components. Varying sizes of fixed–wing models up to 2 m wingspan and many multi-rotors are produced with these methods [28, 56].

5. **Volume of production:** Since AM techniques cut out the need for tooling, the manufacturing cost per unit becomes relatively constant and more economical when

limited number of products is produced [4]. AM materials cost significantly more than that of the conventional techniques as they go through special processes to be brought to a printable format. This reduces the benefit of AM for larger build volumes.

6. **Structure type:** AM structures are generally unconventional, intricate structures which are challenging or sometimes impossible to obtain with conventional methods. Hence, they comprise free-form bodies, bio-inspired/organic-like structures, lattices/periodic cellulars and topology optimized components discussed in Section 2.3.1.

7. **Need for in–situ manufacturing:** As the focus is generally towards AM of expensive parts, manufacturing on-demand is also a reason for AM, which reduces the transportation and storage costs significantly [4]. If the intended application of the aerial vehicle falls into this category, AM would be a useful strategy to implement.

8. **Other AM parameters:** Quality standards for AM is one of the current research focuses since AM parts are strongly affected by the material quality, e.g,. degradation over time, humidity absorption, powder grain sizes, as well as the manufacturing parameters such as printing volume, part size, temperature, material feeding method or combinations of those [6]. Hence, for the safety critical applications in aerospace engineering, AM remains an exploratory method whereas for prototyping and research setups, it is a convenient strategy. Adding functional complexity is also another focus of AM in aerospace, such as achieving conductivity on skin-like covers or embedding of electronics to the structures, which could contribute to the reduction of wiring effort in UAV design process and allow for more payload and space on a vehicle [57].

Table 2.2: A brief summary of evaluation of AM methods for UAV manufacturing.

Process	Resolution	Materials	Material Type	Support	Remarks
FDM	±0.197 mm	ABS, PLA, Nylon & some other thermoplastics	Filament	Soluble or breakaway thermoplastic material	Moderate material strength Moderate surface roughness Feasible impact resistance Layer separation problems Stair stepping problems Variable cost of materials Acceptable resolution **Widely used for UAVs**
SLS	±0.381 mm	Carbon fiber, nylon, plastics, metal, ceramic, glass	Powder	Self–supported	Easy removal of support material High material strength Cost–efficient input material Comparably lower resolution High surface roughness Extensive post–processing Minimal waste High demand for initial input material **Widely used for UAV structures** **Widely used for functional part manufacturing**
SLA	± 0.05 mm	Photopolymers	Liquid resin	Liquid resin	High resolution Feasible surface quality Break–away support material Loss of material strength over time Time–consuming curing process Post–heat treatment to strengthening Cost–inefficient resin–based material High demand for initial input material Fragile against loading responses **Unfavorable for UAV manufacturing** **Favorable for simple component manufacturing**
LOM	±0.203 mm	Paper, wood, plastic, metal	Sheets	Self–supported	Adhesive dependent quality Layer separation problem Cost–efficient input material Dimensional accuracy problems Tough support removal process **Inefficient for UAV manufacturing**
MJM	±0.076 mm	Acrylic (liquid) plastics	Liquid	Soluble or dissoluble wax–based support	Feasible surface quality High resolution Expensive input material Plastic deformation Suitable for multi–material process Fragile against loading responses **Unfavorable for UAV manufacturing** **Favorable for component manufacturing**

2.3.5 Effects of Build and Print Orientations with FDM

The variation of the manufacturing orientations within the printer volume results in variations in the microstructural design, thus affecting the mechanical behavior of the printed components [58, 59]. Several researchers have studied the effect of print [60, 61] and build orientations [62, 63] for mechanical capability of FDM parts, concluding that printing parameters induce anisotropy in the mechanical response on a varying scale depending on the printer type and materials used.

Simulating FDM printed parts using the finite element (FE) method requires a material model which must be robust; and the method adopted in deriving this model has to consider the effect of print and build orientations. In [64], the FE method is implemented to compare isotropic and anisotropic material models to simulate FDM parts and is concluded that an FDM part must be considered anisotropic. In [65], where an orthotropic material model computes the stiffness matrix to simulate FDM printed polycarbonate parts at various build orientations. It concludes that an isotropic material model is sufficient to simulate FDM parts with different build orientations. The mean values of the elastic mechanical properties in different build directions are given as an input to the FE solver. Another closely related study conducted in [51, 66] on ABS and ULTEM parts respectively concludes that the arrangement of the layers or the build orientation to the direction of the application of load is critical to the mechanical response of an FDM printed part.

2.4 Quasi–Steady and Unsteady Aerodynamic Forces and Moments

The flight regime of a fixed–wing VTOL UAV consists of multiple stages including vertical take-off and hover, transition from hover to steady level flight, backward transition from steady level flight to hover, and finally landing. In this context, the math-

ematical model must account for all transient aerodynamic forces that occur during transition phases. While switching from hover to forward flight, the effect of unsteady aerodynamics changes significantly [73]. Hence, accurate prediction of aerodynamic forces is a necessity for transition flight. Previously in literature, unsteady forces are accounted for by assuming quasi-steady flows. In this approach, the unsteady angle of attack is used to predict the forces which can be tabulated either by computational fluid dynamics (CFD) analyses [74] or experimental results from wind tunnel tests [10, 75]. Also, curve fittings as in [76, 77] are also used, in which aerodynamic forces at different angles of attack are estimated by mathematical formula obtained by using the available data. There are also empirical software such as XFLR5 or DATCOM [78], which provide approximate aerodynamic coefficients in a much shorter time when compared to CFD analyses. However, the quasi-steady approach neglects the unsteady transient effects which are significant in rapid transitions from a stationary state to a forward flight.

Unsteady aerodynamic forces can be obtained numerically by CFD analyses [79, 80]. These models are computationally expensive to apply and implement in a coupled control simulation. Since viscous effects can be negligible for transients [9], an attractive alternative to CFD is the unsteady vortex lattice method, which has been successfully used to model flapping wings and bio-inspired flight [81, 82]. While vortex lattice models account for full three dimensional unsteady motion, they also require significant numerical resources. Recently, a simpler technique, the unsteady lumped vortex model, which accounts for the unsteady aerodynamic forces, has been used for the aeroelastic modeling of helicopter blades [83]. This type of an unsteady aerodynamic model can be considered to calculate the unsteady forces during transition flight with higher accuracy when compared to a quasi-steady model.

2.5 Transition Flight Control

During transition flight, aerodynamic loads of fixed–wing VTOL vehicles change drastically; hence, control during transition is more challenging than the other flight phases. Moreover, transition flight is carried out from hover mode to a stable level flight mode, which further complicates the control problem as it is not possible to assume a single linear model representing the complete transition. Overall in literature, quasi-steady aerodynamic models are assumed, which is a significant reduction in the aerodynamic complexity of transition flight.

Conventional model–based controllers are widely used for transition flight. Single or multiple gain-scheduled proportional-integral-derivative (PID) controllers are frequently implemented. To simplify the problem, some of the control surfaces are removed [84, 85] or thrust is input as the only control parameter [86]. For example, a linear quadratic integral controller is proposed for only attitude stability of a tilt–wing system in [87]. Otherwise, more advanced nonlinear controllers are employed to overcome the above-mentioned nonlinearity To improve the control performance, nonlinear dynamic inversion [88], trim manifold generation at multiple flight speeds [89] or control mixing between the rotor and control surface effectiveness [90] are some of the methods used in literature. Another promising method is proposed in [78] using gain scheduling for PI, where the vehicle model switches from one to another during transition flight. This approach is further extended in [11] to handle the control problem under wind gusts. In this article, the controller uses an output regulation method to feedforward the error, in which the system updates the controller depending on the differences from the nominal plant models. Although this increases the model complexity, it is an efficient way of accounting for disturbances.

In addition to the conventional methods, some numerical techniques are proposed in [91, 92], where dynamic changes such as misalignment of center of gravity during

transition flight and inaccurate estimation of aerodynamic parameters are taken into account. As these approaches try to formulate the dynamic changes mathematically in a linear time invariant manner, they should be tested for failure on a real-time implementation. In [93, 94], a backstepping algorithm is applied on a tilting bi–rotor system in simulation environment. Although the controllers based on the Lyapunov functions help with an in-depth stability analysis, finding the suitable functions requires excessive amount of work, especially for the convoluted nonlinear dynamics.

In literature, model–free controllers are not used for transition flight control as commonly as the model–based controllers. They are generally used for compensating the disturbances, which are difficult to include in dynamic models. Model–based controllers are quite sensitive to disturbances due to the same reason. For instance, the artificial neural network (ANN) developed in [95] improves the robustness of PID controlling the transition maneuver under varying model parameters. In some other examples [96, 97], instead of gain scheduling, an ANN is implemented so that the dynamic inversion error and external disturbances are alleviated for the control of tilt–rotor vehicles. A similar strategy is utilized in [98] where a multi-layer ANN helps to estimate the model error by the state observer.

Among model–free controllers, fuzzy logic control (FLC) has already shown its effectiveness to the stated problems for many robotic applications. [99, 100]. However, to handle disturbances, its tuning can be supervised by a learning algorithm, an ANN, to avoid human intervention and manual tuning [101]. The use of FLC with ANN, namely, fuzzy neural network (FNN), can be classified as type-1 (T1FNN) and type-2 (T2FNN) depending on the type of membership functions. T2FNN is proven to outperform its T1FNN counterpart when the collected data is noisy or under varying disturbances [102, 103]. In this context, a learning controller consisting of a T2FNN with PD may be a solution for the full flight envelope control problem of VTOL UAVs. T2FNN helps PD to “learn” the dynamic changes during flight and is able to perform

under perturbed conditions.

In short, the literature reflects that ANNs are used together with the traditional model–based controllers so that the model variations and problems associated with the linear controllers such as PID tuning and gain-scheduling are reduced. However, one should account for the increasing complexity of controller design process or off-line training needed for an ANN. Having said that, selected approaches for transition modeling and control strategies are summarized in Table 2.3.

Table 2.3: Comparison of Key Transition Modeling and Control Approaches

Project	Alexis et. al [104]	JAXA Group [11, 78]	ITU Turac Group [75]	Suzuki et. al [87]	SUAVI Group [105]
Control Strategy	Direct switching from hover to translation	PI scheduling	PID Controllers	P control for yaw, LQI for roll-pitch	PID Controllers
Remark	Multi models are used	1) Seven models distributed in the α range from 0 to 90 deg are selected for transition. 2) Stability augmentation is added on PI based on linear model.	1)Slipstream effect of the rotors over the wings are taken into account and modeled mathematically by using a sigmoid function. 2) Depending on the transition scenario, it switches between hover, transition and forward flight controllers.	1) Slipstream effect of the rotors over the wing and flaperons are taken into account. 2) Yaw model and pitch-roll model are designed seperately and in a linear manner. 3) Thrust fluctuations are also taken into account.	1) A look-up table for motor signals, wing angle of attacks and current drawn by two motors on the half model for nominal flight is generated. 2)The model includes the effects of the propulsion system, the aerodynamic forces and the disturbances. 3) Position controllers for all three modes (vertical, transition, forward flight) are separate from each other while attitude controllers are common.
Assumptions	Linear models	1) Linear model components satisfy controllability and observability conditions. 2) Stability augmentation system is assumed to cover the whole flight regime.	1) Nonlinear models are used. 2) Particular transition scenarios are generated, where the tilting motion is step-by-step defined. 3) The transition effect is assumed to be affecting the longitudinal motion only so the transition effect is only in 3-DOF.	1) The transfer function between yaw moment and yaw rate ras wall as the pitch and roll moments and their corresponding angular rates are assumed to be of the first order transfer functions. 2) A first order delay is assumed between the change of flaperon angle and the direction of the slipstream.	1) Vertical position controllers are employed during the transition between the vertical 90 deg and the horizontal 30 deg wing angles. 2) Aerodynamic downwash effect of front wings on the rear wings are neglected. 3) The dynamics of the vehicle in quadrotor mode is expressed as a a quadrotor model.
What is missing ?	Transition dynamics, fixed wing dynamics	There is little information about the effect of high α during transition flight.	1) Full-flight envelope flight experiments. 2) Complete coverage of the α from 0 to 90 deg. 3) Justification of the sigmoid function approach developed for the slipstream effect on the wing.	The control results are only in the helicopter mode. The response for the tilt angle range of [0, 20 deg] from the vertical shows the heli model is valid until 10 deg.	The purpose of transition mode position controllers is mentioned as ”to keep the altitude of the aerial vehicle at some desired value” but the desired yaw angle is set arbitrarily in transition mode.
Drawbacks	Not applicable to transition dynamics	1) Selected points cannot cover the whole range of transition. 2) Stability augmentation system fails to cover the whole flight regime.	1) The effect of transition on lateral-directional motion (yaw becomes roll, roll becomes yaw) is not taken into account. 2) The nonlinear aerodynamics effect is included only up to a limited α range.	There is neither a stand-alone transition controller nor a mix of the control inputs between the VTOL and cruise flight modes.	Aerodynamic analysis is only run for the nominal condition and there is little information about the effect of high α on the control.

2.6 Summary

Due to the weight constraints of aerial vehicles, plastic printing is favored to metal printing. Among plastic printing methods, FDM technique is a strong candidate for lightweight applications and is considered to be suitable for the application in this thesis. The material strength for FDM is higher when compared to those of SLA and Polyjet materials, and the printed surface roughness is less compared to that of SLS. However, the layer separation and the stair-stepping problems are not solved, yet. Also, FDM component quality is affected by the printing parameters significantly.

To evaluate the suitability of FDM and the effects of printing and building orientations for this application, conventional and unconventional wing structures should be prepared. Two uniform lattice structures consisting of diamond type honeycomb and the 3D Kagome structures are considered and compared in this thesis.

The effects of rapid transitions between hover and level flight phases should be investigated. To do this, dynamic models with quasi-steady and unsteady aerodynamics are generated and compared in control simulations. Linear and nonlinear models are obtained to test the effect of nonlinear aerodynamics.

For control of transition flight, both model-based and model-free control approaches can be tested. Considering the uncertain environments of UAV applications, conventional PID controllers and T2FNN-based learning controllers can be implemented so that the control performance under disturbances during transition flight can be evaluated. By this manner, a conclusion of whether this type of an advanced controller is necessary can be achieved.

Chapter 3

Design and Manufacturing

3.1 Introduction

The build and print orientations are essential printing parameters while fabricating functional end-use parts using FDM. In this chapter, the capability of FDM as a manufacturing technology to fabricate UAV components is investigated. To reduce the lead time of UAV, parts are often arranged or stacked in different directions to maximise the usage of print volume. In such cases, the build and print orientations of various parts are different, and the designer needs to include their effects in the computational environment to analyze the performance of the component accurately. In this thesis, the effects of both print and build orientations on forming an appropriate material model for simulating FDM printed parts are presented. The elastic mechanical properties are obtained through the uniaxial tensile tests. Based on the results of the uniaxial tensile tests, certain assumptions are drawn and validated by conducting simulation on the representative parts. Finally, a strength-based design analysis on the flying wing UAV is presented to analyze the criticality of build and print orientations in the fabrication of the structure through the FDM process.

In the second part of this chapter, diamond honeycomb and 3D-Kagome periodic

cellular structures are investigated for their bending stiffness to further exploit the design freedom provided by AM as these structures are costly to obtain with conventional manufacturing methods.

3.2 Material Characterization and Investigation of 3D-Printing Effects

3.2.1 Uniaxial Tensile Test: Experimentation and Result

Mechanical characterization of the FDM parts is accomplished by manufacturing them in different build (edge-up (EU), face-up (FU) and straight-up (SU)) and print orientations (0-90°) as shown in Fig. 3.1. The Young's modulus and the ultimate tensile strength of FDM parts in different build and print orientations are presented and a suitable material model is predicted accounting for the changes in build and print orientations.

The tensile test samples are prepared according to the ASTM D638-10 Type-1 standard [106]. Five sample are printed for each build and print orientation, amounting to a total of 75 samples. The Shimadzu AGX-*plus* desktop testing machine with a load cell capacity of 10 kN is used for performing the tensile tests. The tests are performed at a constant displacement rate of 5mm/min. Figure 3.2 presents the stress-strain trends for FDM printed uniaxial tensile test samples. The solid lines, dashed lines and dash-dot lines represent the stress strain of the EU, SU and FU samples, respectively. The plot shows that the EU samples have the highest stiffness and tensile strength compared to FU and SU oriented samples. While a variation in stiffness and strength is evident for different build orientations, these parameters are not found to vary across different print orientations. Furthermore, Fig. 3.2 also showcases the non-linear behavior of tensile samples at different print and build orientations. EU and FU samples showed a prominent plastic region, where the material progressively fails through yielding before

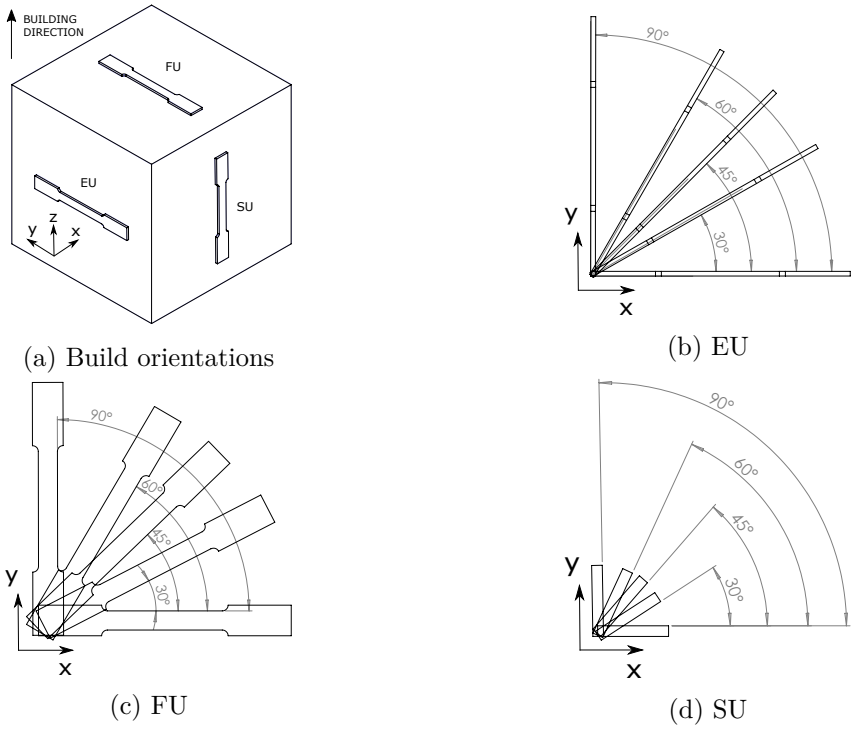

(a) Build orientations

(b) EU

(c) FU

(d) SU

Figure 3.1: Tensile specimen oriented in various build and print orientations.

complete failure while the SU sample fails in a brittle manner. Although the failure mechanism varies across different build orientations, it is found to remain the same for different print orientations.

3.2.2 Meso-Structures

The rasters inside the FDM part are arranged to reduce the air gap since the print interior style chosen is solid. The rasters are thermoplastic polymers which are in a semi-molten state due to the extrusion process and hence, they result in a phenomenon called as inter-road bonding. The phenomenon is explained in [107], where an individual raster comes in contact with its neighbours and undergoes necking and consequently, the rasters coalesce at the phase boundary to form a single entity as illustrated in Fig 3.3a.

Inter-road or inter-raster bonding is critical to understand the mechanics of FDM

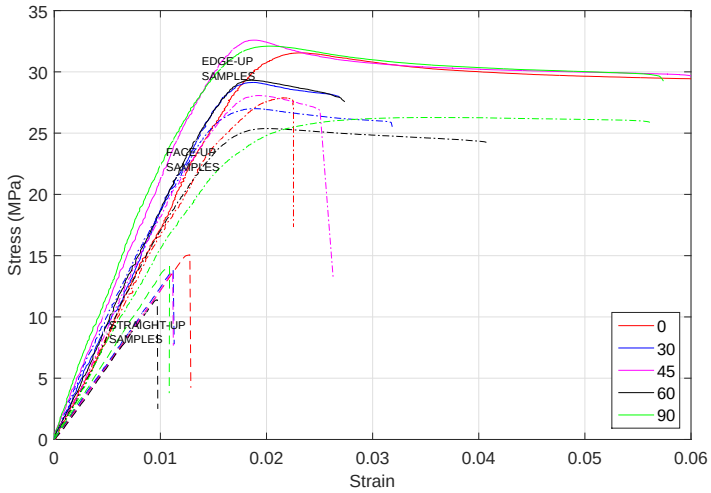

Figure 3.2: Representative stress-strain plot for flat samples at various print and build orientations.

parts when the raster or print angle within the print bed changes. The bonded area is an essential factor to consider while analyzing the effect of print orientation on the stiffness and strength of an FDM part. Unlike composite materials, where the stress inside the material is induced by the interacting forces between the polymeric matrix and carbon/glass fibre, an FDM printed part comprises of voids instead of the matrix constituent. The load is predominantly carried by the individual rasters and the area

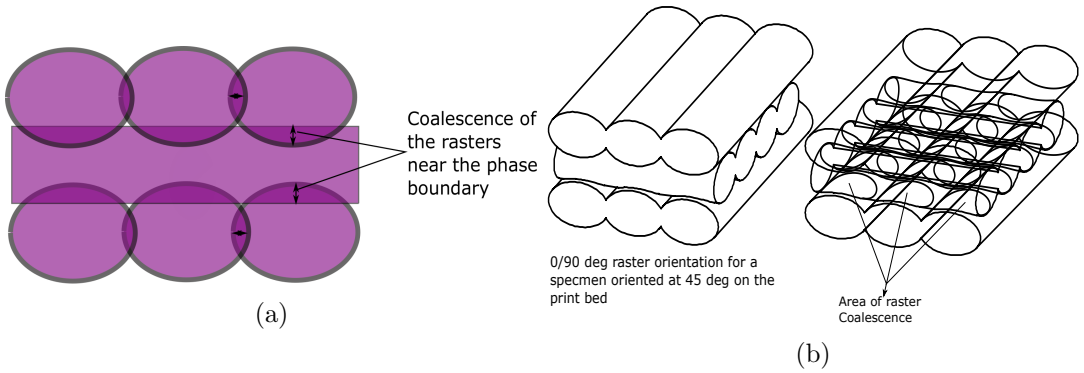

Figure 3.3: Coalescence in the rasters (a); the coalescence area between the rasters which are vital for the performance of the part (b).

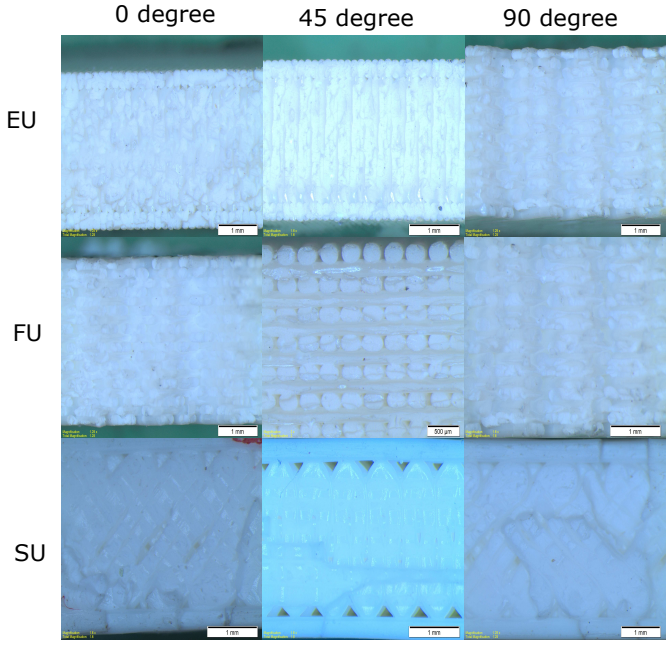

Figure 3.4: Meso-structure of the fractured surface of EU, FU and SU samples at various print orientations.

of coalescence as shown in Fig. 3.3b. The effect of the area of coalescence can be further explained by studying the meso-structure of a FU specimen oriented at 45°. The fractured surface is examined under a scanning electron microscope (SEM) to observe the morphology of the surface and the SEM image is given in Fig. 3.5a. From Fig. 3.5a, it can be concluded that the damage initiation happens at the inter-facial region between the layers and then advances to the individual rasters. Raster pull out is observed at various regions in the morphology of the fractured surface which shows that the adhesion between the layer fails and the raster is pulled out due to the tensile load. Once the maximum strength of the raster is achieved, they undergo failure in a brittle fashion.

Figure 3.4 presents the meso-structural arrangements of an EU, FU and SU sample oriented at 0°, 45° and 90° degrees respectively. The density of the meso-structural arrangement is the critical parameter here. The density increases the area of coa-

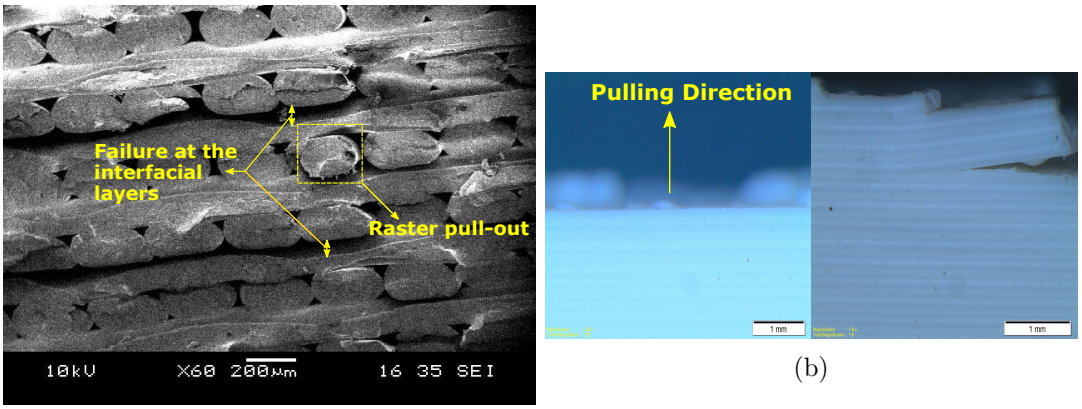

(a) (b)

Figure 3.5: Meso-structure of the fractured surface of an FU oriented FDM part under SEM. (a); microscopic image of the fractured edge showing failure between the stacked layers (b).

lescence, which is imperative to the mechanical performance of the FDM part. For EU samples, the meso-structure is more dense compared the other two, resulting in the highest stiffness and strength among all arrangements. Furthermore, FU and SU samples are perceived to have a similar density. However, the pulling direction or the loading direction is different for an SU sample, as seen in Fig. 3.5b.

In the case of the SU sample, the load is applied perpendicular to the direction in which the layers are stacked and hence, owing to the poor adhesion between the layers, the SU sample fails in a fragile manner as shown in Fig. 3.5b [108]. When the raster orientation changes between the layers, the area of coalescence does not change significantly in the case of an EU and FU sample. Therefore, the contribution to the stress developed in the meso-structure due to varying raster angles is minimal. Since the predominant load bearing element in an SU sample is the adhesive strength between the layers, the surface area change in the layers due to the different alignment of the rasters is very unlikely. However, the mechanical properties are predominantly influenced by the alignment of the individual raster to the direction of the load (evident in FU specimens). This influence, although provides a change in the stiffness and

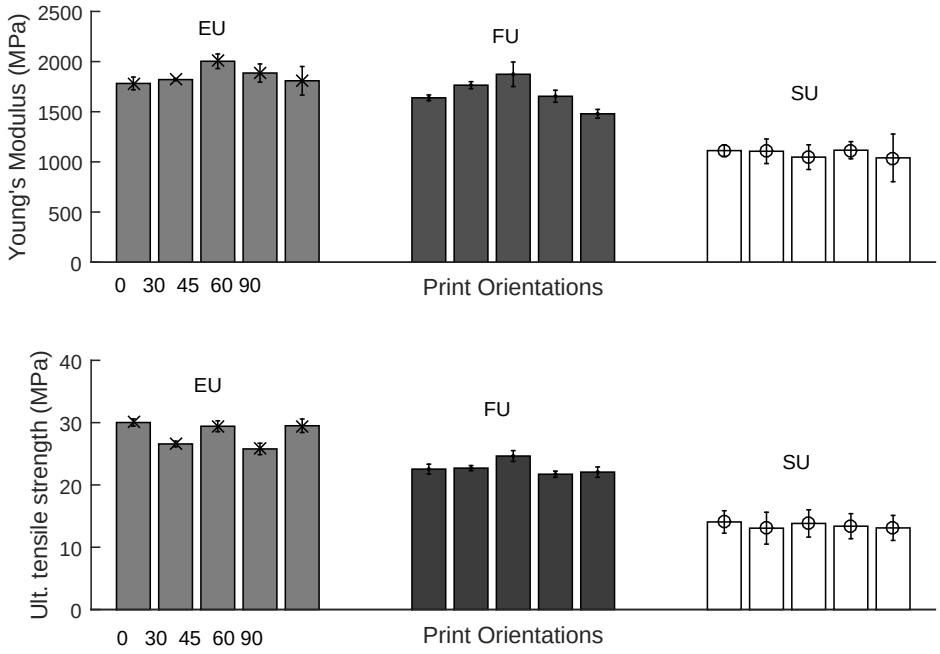

Figure 3.6: Comparison of the Young's modulus and ultimate tensile strength for various print and build orientations.

strength values, is not alarmingly different from the specimens oriented at other angles as seen in Fig. 3.6. The standard deviations (SD), marked by the error bars in each print orientation for a build orientation overlap each other and hence, the variation of the stiffness and strength properties along the print orientation is found to be minimal. Therefore, for simulating FDM parts fabricated in different print orientations, the mean of the elastic modulus and the strength value is taken in to consideration at each build orientation as shown in Table 3.1.

3.2.3 Testing and Simulation of Representative Curved Samples: Flexural Response of Flat and CLFDM Samples

Since the slicing software used for the printer has different travel/toolpath algorithms for flat and curved samples, an additional analysis should be conducted for the

Table 3.1: Comparison of the Young's modulus, Poisson's ratio and ultimate tensile strength for various build orientations.

Build Orientation	Young's modulus (MPa)			Ultimate tensile strength		Poisson's ratio
	E	SD (± MPa)	% diff (w.r.t SU)	σ_{ult}	SD (± MPa)	
EU	1808.60	88.64	73%	29.50	1.93	0.35
FU	1479.40	147.69	42%	22.06	0.55	0.36
SU	1040.20	48.15	-	11.60	0.97	0.34

curved layer FDM (CLFDM) parts [109–111]. Geometrical aberrations arising due to the build orientation of a CLFDM sample is analyzed to ensure their influence on the physical response is not severe. Finite Element (FE) analysis of the flat and CLFDM samples are conducted using ABAQUS, and the material model is validated.

The samples used for the three-point bend test for flat samples is prepared according to ASTM D790 standard. Procedure A (small deflection) and Type 1 methods are employed in the experiments. The printed sample has the dimensions 150 × 12.7 × 3.2 mm and a gauge length of 50 mm. Three specimens are printed and tested for each build (EU, FU and SU) and print (0°, 45° and 90°). The cross-head displacement rate (1.3021 mm/min) and the displacement at which the maximum strain in the outer surface reaches a maximum are calculated as per mentioned in the standard. The CLFDM samples are printed in similar print and build orientations as the flat samples. The dimensions of the CLFDM samples are shown in Fig. 3.7. Experiments are conducted using the Instron 5569 testing machine fitted with a load cell capacity of 100 kN.

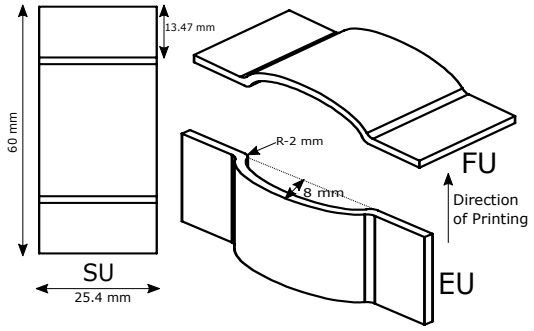

Figure 3.7: Orientation and dimensions of the curved samples in the build volume.

Linear elastic material properties for different build orientation mentioned in Table 3.1 is given as the input in the FE solver. The indentors are modelled as rigid bodies using a rigid body constraint option. A linear static analysis is conducted on the samples. A vertical downward displacement of 1.2 is given to the samples where the structure is still elastically deforming. The curved sample is meshed with 26,877 and the flat samples comprises of 96,768 linear hexahedral elements of type C3D8R. The indentors are meshed with quadrilateral elements of type S4R. The FE model of the CLFDM sample in ABAQUS is shown in Fig. 3.8. FE model of the flat sample is created using a similar approach adopted for modelling CLFDM samples.

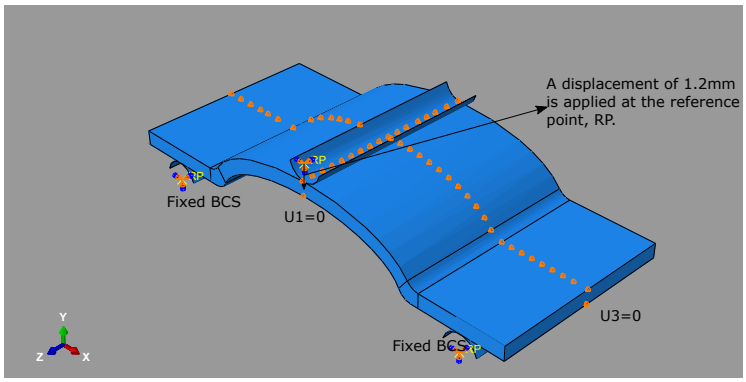

Figure 3.8: FE model of the CLFDM sample in Abaqus.

Table 3.2: Comparison of experimental and FE result for the CLFDM samples.

Build Orientation	F/d-Expt (kN/mm)			F/d expt. mean (kN/mm)	F/d-FE (kN/mm)	% diff. of the FE result from the expt.
	0	45	90			
EU	0.018	0.019	0.018	0.0183	0.01875	4%
FU	0.013	0.015	0.013	0.014	0.015	6.7%
SU	0.013	0.013	0.014	0.012	0.013	7.7%

The elastic mechanical responses of flat and CLFDM samples at different build and print orientations is compared by calculating the bending stiffness coefficient (F/d) and is listed in Table 3.2 and 3.3. The tables list the results of the experimental and numerical analysis on flat and CLFDM samples. It is observed that the influence of print orientation on the mechanical performance of these parts is minimal since the

Table 3.3: Comparison of experimental and FE result for flat samples.

Build Orientation	F/d-Expt (kN/mm)			F/d expt. mean (kN/mm)	F/d-FE (kN/mm)	% diff. of the FE result from the expt.
	0	45	90			
EU	0.029	0.032	0.031	0.031	0.029	6.4%
FU	0.026	0.028	0.024	0.026	0.025	3.8%
SU	0.023	0.021	0.022	0.022	0.0195	11.3%

variation of F/d is found to be less than 10% which is acceptable since the mechanical responses are influenced by other factors such as raster gap, width and diffusion between rasters. Therefore, an averaged isotropic model is sufficient to simulate the parts with varying raster angles. Moreover, the build orientation has a significant influence on the mechanical performance of these parts. As seen in Table 3.2 and 3.3, it is evident that the variation of flexural stiffness coefficient for both the samples is more than 10% for different build orientations. Also, it is observed that a part oriented at 45° provides better stiffness for EU and FU samples as observed in [112] but in SU orientation, the stiffness is minimal, as can be seen in Fig. 3.9 and 3.10. Unlike FU and SU samples where the arrangement of the rasters and layers contribute to the stiffness, the SU sample's stiffness is dependent on the adhesion between the layers and hence, comparison of the experimental result with FE analysis showed a larger deviation of 7.7% and 11.3% in the case of CLFDM and flat samples. Therefore, it is more favourable to build components oriented in FU and EU direction since they are easier to simulate and there is less probability for obtaining parts with less discontinuities. Although there are disadvantages, SU orientation provides a critical advantage of building long parts in most of the FDM printers. Therefore, a numerical design analysis shall be done prior to the building of these parts to reveal their stress state.

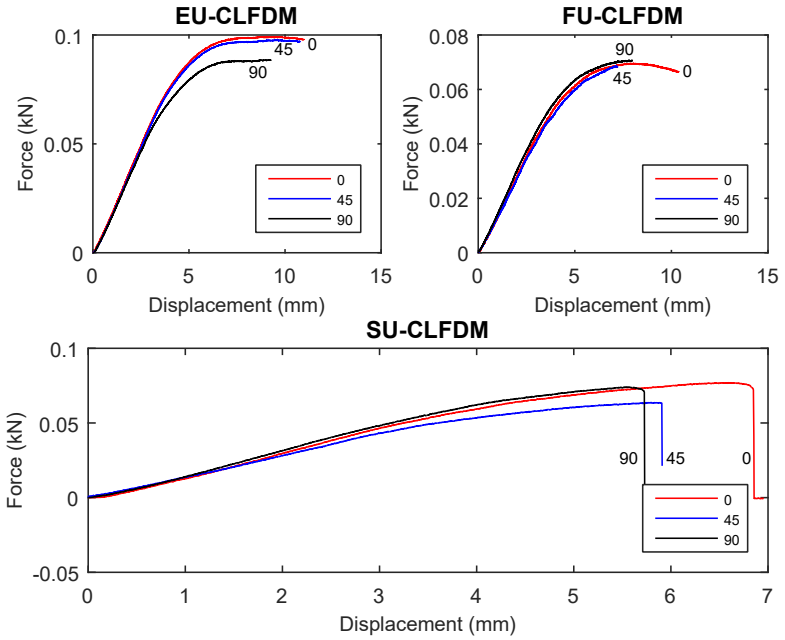

Figure 3.9: Force versus displacement experimental plot for CLFDM sample in different print and build orientations.

3.3 Application to UAV

Strength-based structural design based on the FE method is conducted for the flying wing model to determine appropriate build and print orientation of parts. The study combines the FE and Taguchi [113] and analysis of variance (ANOVA) statistical methods to determine the contribution of building orientation selection to the mechanical quality of the UAV structure. Taguchi method is used to drastically reduce the number of simulations, thereby reducing the lead time in part manufacturing. The ANOVA analysis is performed to study the contribution of build orientation to the UAV's structural integrity. The approach is beneficial since it reduces the prototyping cost in the preliminary structural design phase of the UAV and the computational cost [113, 114].

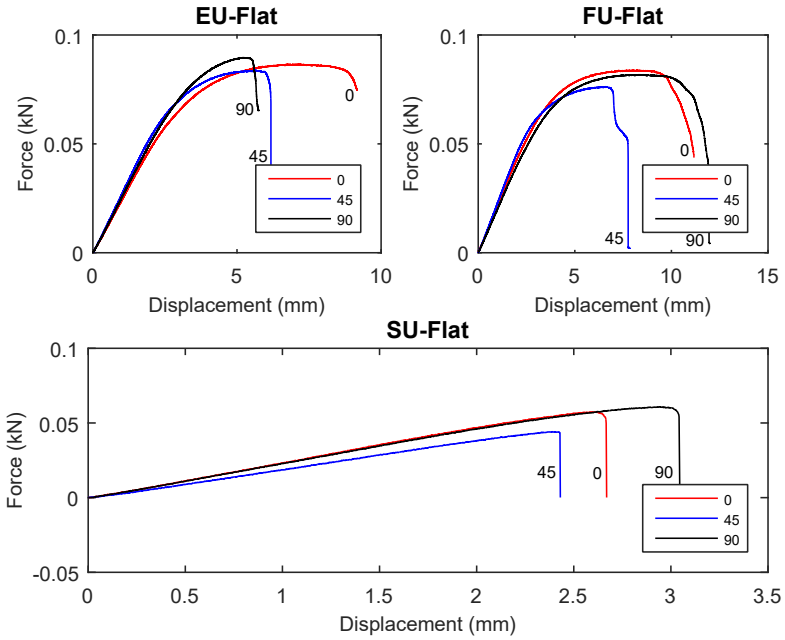

Figure 3.10: Force versus displacement experimental plot for flat samples at different orientations.

3.3.1 Taguchi Method: Factorial Selection and Orthogonal Array Design

The controllable factors chosen for this analysis are the thickness of the skin, number of ribs and the build orientation of the part. The skin thickness is crucial for resisting the buckling loads due to the bending moment. Rib spacing is an essential factor in carrying the aerodynamic loads as well as the shear from the skin panels. The factor values are chosen considering the minimum printable thickness by the printer and the maximum structural weight approximated during the initial design phases. The controllable factors and the levels selected for each of them are listed in Table 3.4. This section is a comprehensive analysis on the designed UAV structure, focusing on determining the contribution of build orientation selection to the strength of the structure and design calculations such as the thickness of the skin, rib spacing and spar positions are neglected.

Table 3.4: Controllable parameters and levels chosen.

Controllable parameters	Level 1	Level 2	Level 3
Skin thickness	0.5	0.75	1
No. of ribs	9	11	13
Build orientation	EU	FU	SU

Maximum von-Mises stress and the mass of the structure are considered as the responses from the FE simulation of the UAV structure. The goal of the study is to minimize the von-Mises stress and the weight and hence, the smaller-the-better characteristic is chosen to compute the signal-to-noise ratio (S/N) analysis as shown in (3.1),

$$S/N = -10.log_{10}[\frac{1}{n}\sum_{i=1}^{n} y_i^2] \tag{3.1}$$

where n is the number of simulations of a particular experiment and y is the value of the performance parameter examined.

3.3.2 FE Model of the UAV

The dynamic responses of the UAV are neglected and a quasi-equilibrium condition is assumed. The loads on the UAV structure is computed for a single maximum load case of 3 which is a safe value to consider as seen in [115]. A factor of safety of 1.5 is included in the calculation of the loads. The aerodynamic loads are computed using XFLR5. The aerodynamic loads are given in the FE model as cut-loads which comprises of three orthogonal pairs of shear force, bending moment and torsional moments acting on the elastic axis along the span of the UAV, as seen in Fig. 3.11 [116].

The shear force, bending moment and the torsional moment are applied using the structural distributing elements [117]. Inertial relief loads, such as the mass of the motors, motor booms, battery etc., are applied as a point mass in the FE model. A fixed boundary condition is employed at the plane of the symmetry of the model as the wing is approximated as cantilever beam fixed to the mid-rib. The mechanical

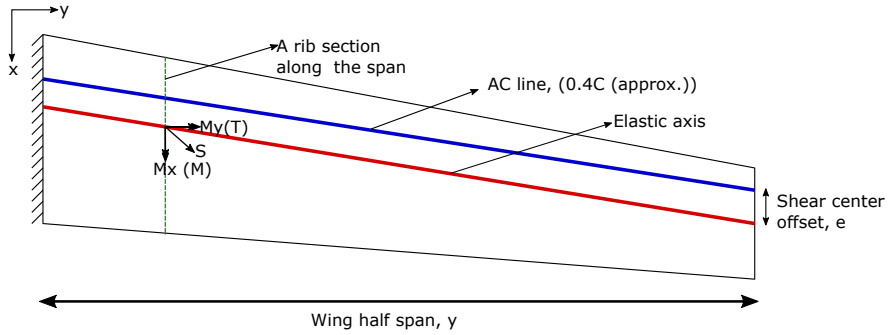

Figure 3.11: A representative location of elastic axis and cut loads applied along wing span.

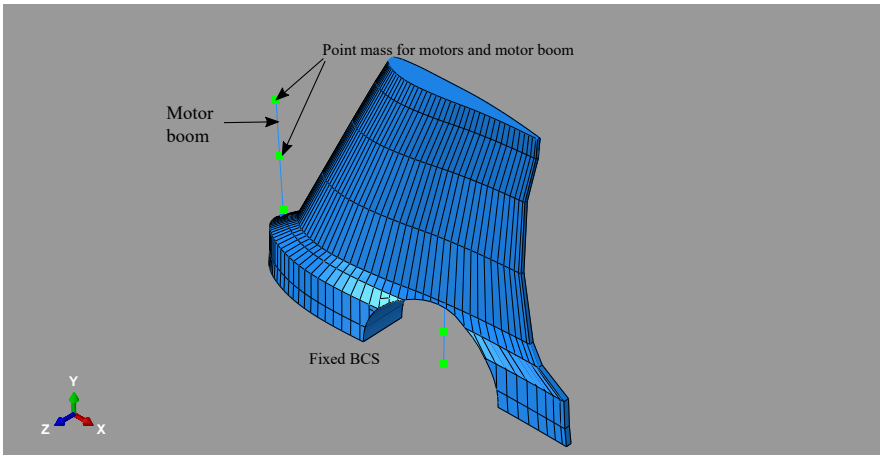

Figure 3.12: Point mass and boundary conditions in FE model.

properties from Table 3.1 are used as an input to the software. The FE model created in ABAQUS is shown in Fig. 3.12. The skin and the ribs are meshed with a 4-node shell element, S4R, and the motor booms are meshed using the two node linear beam element, B31. Three FE models are created with varying number of ribs depending upon the combinations mentioned in the L9 orthogonal array. The number of elements created for each FE model afer the mesh sensitivity analysis is shown in Table 3.5.

The combination of the controllable factors in each simulation, the maximum von-Mises stress and the structural weight of each configuration is recorded in Table 3.6. The Taguchi method based on the L9 orthogonal array is conducted to provide a simple,

Table 3.5: Number of elements in the final FE model after the mesh convergence test.

Number of ribs	Element type	
	S4R	B31 (158-front, 125-rear)
9	83189	283
11	85071	283
13	85488	283

computationally cost-effective and a systematic method for determining the optimum level of the controllable factors. The S/N ratio for both the responses is recorded in Table 3.7 and 3.8.

Table 3.6: The L9 orthogonal array, response values from FE simulations and the S/N values for the responses recorded.

Analysis no.	**Sheet thickness**	**No. of ribs**	**Build Orientation**	**von Mises (MPa)**	**Mass (kg)**	**S/N von Mises**	**S/N Mass**
1	**0.5**	**9**	**EU**	**8.342**	**0.889**	**-18.425**	**1.022**
2	0.5	11	FU	9.742	1.010	-19.773	-0.086
3	0.5	13	SU	10.760	1.160	-20.636	-1.289
4	**0.75**	**9**	**FU**	**5.239**	**0.999**	**-14.385**	**0.009**
5	0.75	11	SU	6.100	1.120	-15.707	-0.984
6	0.75	13	EU	6.592	1.270	-16.380	-2.076
7	**1**	**9**	**SU**	**3.310**	**1.110**	**-10.397**	**-0.906**
8	1	11	EU	3.820	1.230	-11.641	-1.789
9	1	13	FU	3.944	1.380	-11.919	-2.798

Table 3.7: S/N response table for von Mises stress (MPa).

Levels	Skin thickness	No. of Ribs	Build Orientation
1	-19.61	**-14.40**	-15.48
2	-15.49	-15.71	**-15.36**
3	**-11.32**	-16.31	-15.58
Delta	8.29	1.91	0.22
Rank	1	2	3

The highlighted values in the tables show the optimum values that could be chosen for the least weight and best mechanical performance of the UAV. A low stressed structure is possible if the skin thickness, the number of ribs and the build orientation are to be 1 mm, 9 and FU respectively. For the least structural mass, these factors must take the values of 0.5 mm, nine ribs and EU orientation. Without exception, both

Table 3.8: S/N response table for structural mass (kg).

Levels	Skin thickness	No. of Ribs	Build Orientation
1	**-0.11787**	**0.04140**	**-0.95074**
2	-1.01725	-0.95630	-0.95844
3	-1.83405	-2.05427	-1.05999
Delta	1.71617	2.09567	0.10926
Rank	2	1	3

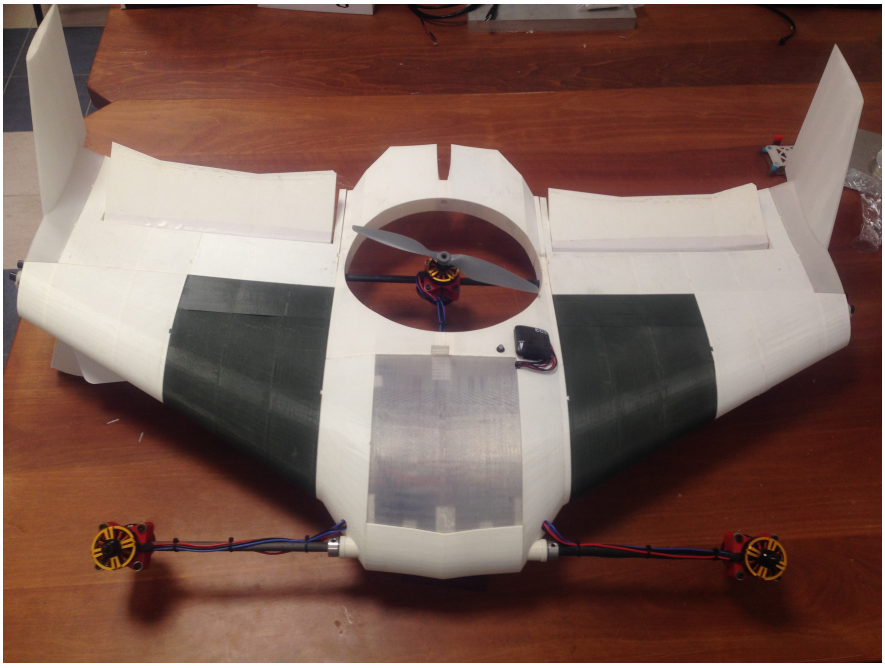

Figure 3.13: Resulting model with approximately 2 kg (0.999 kg × 2) structural weight.

the responses demand a maximum rib quantity of 9. Therefore in Table 3.6, between analyses 1 and 4, the configuration for analysis 4 is the least stressed among the two and the structural mass (0.999 kg) is close to the mass value given as the input during the stability and aerodynamic analyses. Therefore, the factors defined in analysis 4 can be chosen as the most optimum combination for the fabrication of the initial prototype (see Fig. 3.13).

3.3.3 ANOVA Analysis

An ANOVA analysis is conducted to examine the influence of build orientation on the mechanical behavior of the UAV configuration. It is used to study the effect of the skin thickness, the number of ribs and the build orientation on the maximum von Mises stress and the mass (conducted to obtain a direction for further structural optimisation) of the structure. This analysis is carried out at a 5% significance level and a 95% confidence level. The results of ANOVA on the von Mises stress and the mass of the structure is shown in Table 3.9.

The results of the ANOVA analysis is critical in understanding the contribution of each control factor to the maximum von Mises stress of the UAV structure. The significance of these factors is determined by comparing the F-values of each control factor. From Table. 3.9, the skin thickness of the structure is the factor affecting the stresses developed in the structure (93%). For this particular configuration, the build orientation of the structure did not influence its mechanical performance. Also, the mass of the structure is found to be primarily affected by the number of ribs (60.2%) rather than the thickness of skin (39.8%) whose surface is larger than that of the rib sections. Nevertheless, these results provide insight into the most critical factors, the maximum von Mises stress and structural mass, affecting the two essential responses that are considered in the preliminary design phase.

3.4 Cellular Structures for UAV Wings

The initial prototype designed with the ribs and spars are based on the conventional aerial vehicle design methods. However, this method does not fully exploit the design freedom provided by AM. The designed system still suffered from the excessive structural weight when compared to conventional prototypes manufactured with balsa wood. The main reason for this difference is the low specific stiffness of the AM ther-

Table 3.9: Results of ANOVA on the von Mises stress and structural mass of the UAV configuration.

Source	DF	SS	Mean square (MS)	% contribution
von Mises stress				
Skin	2	**53.5428**	**26.7714**	**93%**
No of ribs	2	3.3058	1.6529	6%
Build orientation	2	0.3983	0.1991	0.7%
Error	2	0.4074	0.2037	
Total	8	57.6543		
Structural mass				
Skin	2	0.07282	0.03641	39.8%
No of ribs	2	**0.110321**	**0.05516**	**60.2%**
Total	8	0.183142		

moplastics [4]. To better exploit the advantages of AM, complex cellular structures are investigated.

In this section, the diamond honeycomb and 3D-Kagome structures are investigated for their bending stiffnesses and weights as the slot-in method used in the earlier design reduces the bending stiffness considerably. To determine the bending stiffnesses, a set of cantilever beam bending experiments are carried out with various sandwich structures containing different honeycomb and 3D-Kagome cores. Finally, their feasibility for the incorporation in the UAV design is evaluated.

3.5 Cantilever Beam Bending Experiment Results

Referring to the ISO 1209-1 standard [118] for 3-point bending test of cellular plastics, all cantilever beams with dimensions 250 × 60 × 22 mm are designed using Solidworks with two 1mm-thick face sheets sandwiching the different cores. Each cantilever beam has a 48mm solid portion, which is firmly clamped during the experiment. This ensures that one end of the cantilever beam is fixed while the other end is free to move.

All the cantilever beams are printed vertically upwards using the ABS material on Stratasys Fortus 450mc. The T12 nozzle which extrudes a layer thickness of 0.178mm is used for all the printing jobs. The bending tests are carried out using the Shimadzu

Autographer Universal testing machine. The experimental setup is included in Appendix A. The experiments are carried out at a testing speed of 1.3mm/min with a stroke limit of 50mm. Normally, the testing is completed when a brittle fracture occurs at the cantilever beam root. This shows that the core structure distributes the load from the edge to the root of the cantilever beam as planned. In some rare cases, the core material fails due to the compression instead of bending, which indicates that there are some printing defects and the sample needs to be discarded. Each experiment is repeated at least 3 times to obtain a reliable result, excluding the discarded samples.

3.5.1 Diamond Honeycomb Core Results

The diamond core shape is selected in this work as it is the most consistent core type for both elastic and shear behaviors (see Section 2.3.2). Several modes of failure are detected during experimentation. Most of the diamond honeycombs failed due to brittle fracture at the cantilever beam root. This indicates that the diamond core structure is effective in transferring the bending load from the loading end to the cantilever beam root. In one rare case, the sandwich structure failed due core-to-facesheets debonding which leads to the failure of the diamond core.

Figure 3.14 shows the printed cantilever beams with different infill ratios. The core of the diamond honeycomb sandwich structure has a constant wall thickness of 0.4mm. The relative density of the cantilever beam section in bending is calculated by the ratio of the cellular solid density to the material density. Table 3.10 shows the infill values and the relative densities of the cross-section area of the diamond honeycomb cantilever beams. The relative density of the section of the cantilever beam in bending is calculated by the ratio of cellular solid density to the material density [69].

The bending stiffness of the cantilever beam is tabulated in Table 3.11 using the maximum force divided by the displacement. Generally, the bending stiffness increases as the infill percentage rises. The bending stiffness coefficient, which is the ratio of

Figure 3.14: Honeycomb structures with different infill ratios: 3%, 5% and 8%.

Table 3.10: Different honeycomb structures and their properties [72].

Specimen Number / Material	**Infill Ratio (%)**	**Distance Between Vertex (mm)**	**Average Mass (g)**	**Beam Mass w/o Solid Portion (g)**	**Density of Cellular Material (g/cm3)**	**Relative Density (g/cm3)**
I /ABS	3	37.5	92.1	26.21	0.0983	0.0945
II /ABS	5	22.5	102.5	36.61	0.137	0.132
III/ABS	8	14	107	41.11	0.154	0.148

the average bending stiffness over the relative density, is used to determine the optimal infill for the cantilever beam. Figure 3.15 shows the force (N) vs displacement (mm) plot for the diamond honeycomb cantilever beams of the selected infill values. The force vs displacement curves generally have a constant gradient except for the 3% infill where there is a slight curvature. This is due to the insufficient walls in the core region of the sandwich structure compared to other infills.

Table 3.11: Diamond honeycomb bending stiffness and coefficient values [72].

Specimen Number/ Material	**Infill Ratio %**	**Average Bending Stiffness (N/m)**	**Bending Stiffness Coefficient**
I /ABS	3	4544.72	48092.28
II /ABS	5	7343.46	55632.27
III /ABS	8	8957.17	60521.42

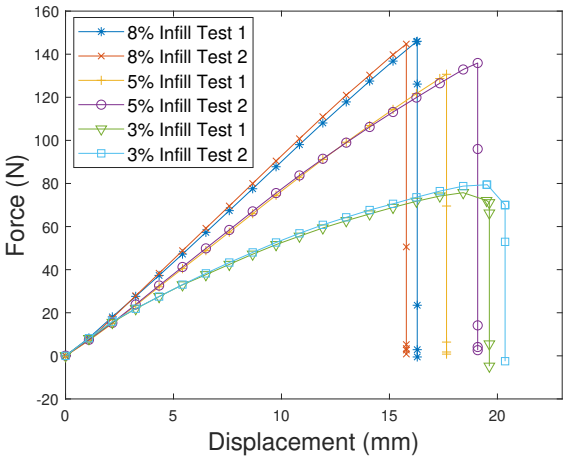

Figure 3.15: Force vs Displacement plots for 2 samples of each diamond honeycomb infill [72].

3.5.2 3D-Kagome Core Results

3D-Kagome structure is one of the most promising 3D cellular structures with superior bending, compression stiffness and impact strength compared to other alternatives. However, manufacturing of 3D-Kagome is challenging and generally, number of large-scale applications are costly. AM of 3D-Kagome may significantly lower its manufacturing cost and duration as the number of steps in line can be reduced.

The design of Kagome structures is possible in two ways: Either the diameter of the trusses is adjusted or the elevation angle between the diagonal truss and the base plane is changed. The optimal angle of elevation is 45° – 55° and the truss diameter should be around 1.7mm to 2.2mm [67]. This provides a guideline for the design of the 3D-Kagome structures. All Kagome trusses fabricated have a standardized length of 12.58 mm and the elevated trusses have an elevation angle of 54°. The bottom and top planes are formed with the equilateral triangles and hexagonal semi-circular trusses. The only variation between the three different struts is the diameter of the trusses whereby they are slowly increased from 1.5 mm to 3mm. Simultaneously, the mass of the beams and the relative density increase as well.

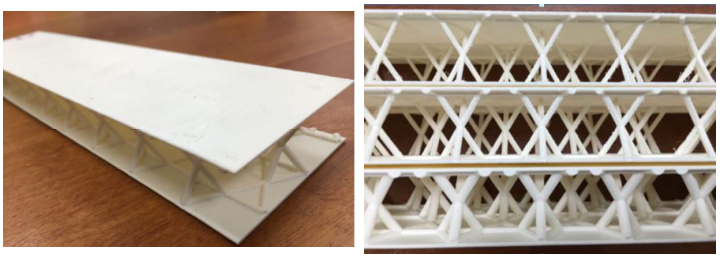

(a) (b)

Figure 3.16: 3D-Kagome cantilever beam (Left). 1.5mm, 2mm, 3mm truss diameter 3D-Kagome structures. (Right Top to Bottom) [119].

Table 3.12: Three different Kagome structures with truss diameters of 1.5 mm to 3mm [119].

Specimen Number / Material	**Truss Diameter (mm)**	**Average Mass (g)**	**Beam Mass w/o Solid Portion (g)**	**Density of Cellular Material (g/cm3)**	**Relative Density (g/cm3)**
IV/ABS	1.5	91.5	25.6	0.096	0.0923
V /ABS	2	98.5	32.6	0.122	0.118
VI/ABS	3	110	44.1	0.165	0.159

It is seen that the 3D-Kagome sandwich structures are much weaker to resist bending load and have lower bending stiffness as compared to the diamond honeycomb. The reason for this is the diamond honeycomb has interconnected plates throughout the entire core of the sandwich structure while the 3D-Kagome has only interconnected trusses throughout the core. It seems that trusses do not provide sufficient stiffness to the beam as compared to the thin wall plates. Table 3.12 shows that there is no significant change in the bending stiffness coefficient when the diameter of the trusses is increased from 1.5mm to 2mm. However, there is a slight increase in the bending stiffness coefficient with the truss diameter increasing to 3mm.

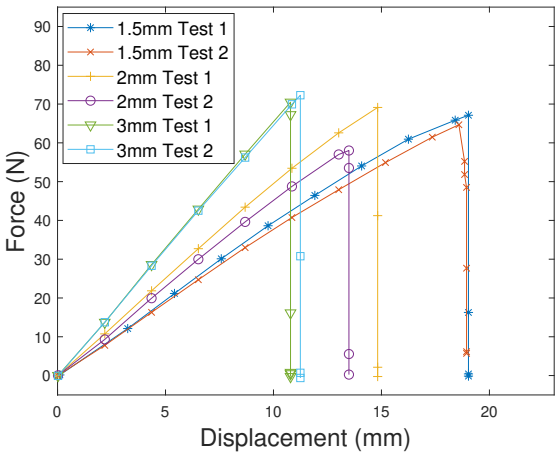

Figure 3.17: Force vs. displacement plots for 2 samples of each Kagome truss diameter [119].

Table 3.13: 3D-Kagome bending stiffness and coefficient values [119].

Specimen Number/ Material	**Struts Diameter (mm)**	**Average Bending Stiffness (N/m)**	**Bending Stiffness Coefficient**
IV/ ABS	1.5	3512.9	38059.58
V/ ABS	2	4482.79	37989.7
VI/ ABS	3	6369.37	40058.93

3.6 Application of Cellular Structures to UAV

The results obtained from the experiments highlight the fact that the diamond honeycomb structure has a superior bending stiffness compared to the 3D-Kagome trusses. Hence, the diamond honeycomb is selected as the wing interior structure of the 1 meter fixed-wing VTOL UAV. The result of the cantilever beam bending experiment provides a guideline for the accurate infill values for the UAV. The UAV is split into 26 different components for printing. The 3D printed components near the fuselage and the mid-rotors are printed with 8% infill as they experience higher loads compared to the components found in the wings and flaps. Table 3.14 shows the rough estimation of the mass with its respective infill. This distribution is applied in the XFLR5 model.

When compared to the first model with the conventional ribs and spars, the diamond honeycomb wings provided a 31.8% weight reduction, shown in Fig. 3.19. Manual VTOL flights are conducted to prove the validity of the model.

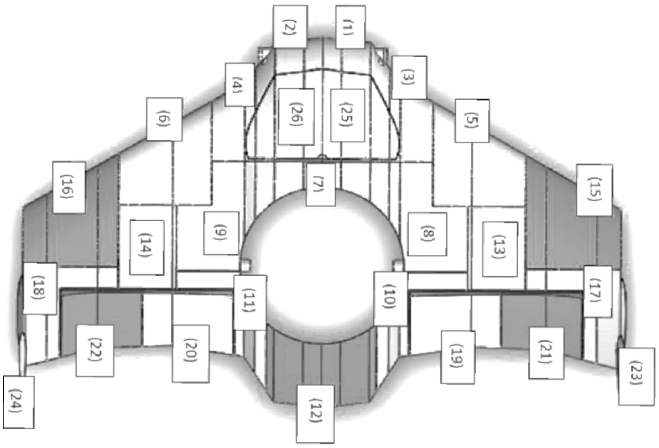

Figure 3.18: UAV printing architecture [119].

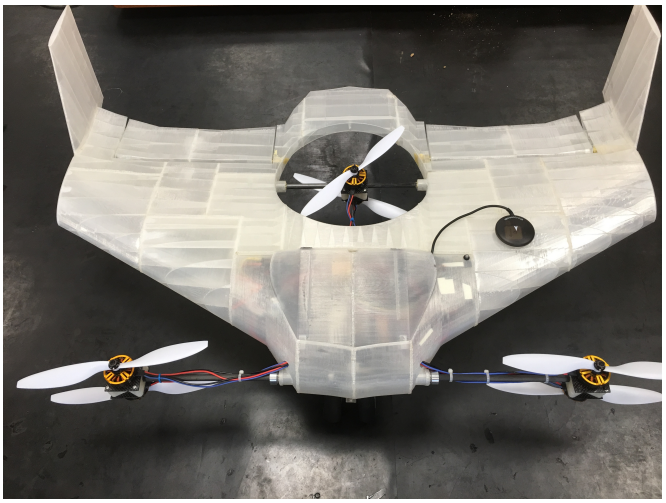

Figure 3.19: Diamond honeycomb model with approximately 1.3 kg structural weight [119].

Table 3.14: Diamond Honeycomb Part Weights [119].

Component	**Infill** (%)	**Thickness** (mm)	**Mass Estimation** (g)	**Actual Mass** (g)
Fuselage–1	8	0.8	74.94	68
Fuselage–2	8	0.8	75.44	69
Fuselage – 3/4	8	0.8	60.61 × 2	65 × 2
Wing Part – 5/6	3	0.4	78.89 × 2	64 × 2
Fuselage support – 7	5	0.4	115.10	NA
Mid-Rotor Support – 8/9	5	0.8	128.5 × 2	118 × 2
Tail Support – 10/11	3	0.4	24.32 × 2	21 ×2
Tail– 12	3	0.4	38.75	33
Servo Support – 13/14	3	0.4	51.28 × 2	46 ×2
Wing Part – 15/16	3	0.4	75 ×2	63 ×2
Winglet Support – 17/18	3	0.4	36.19 × 2	26.2 ×2
Flap Part – 19/20	3	0.4	25.36 ×2	20 ×2
Flap Part – 21/22	3	0.4	23.45 × 2	23 ×2
Winglet – 23/24	2	0.4	42.17 ×2	40 ×2
Cover – 25/26	3	0.4	25.53 × 2	25 ×2
Total			1331.73g	1192.4g
Error				10.4%

3.7 Summary of Design Procedure

The design procedure in this study is summarized with the help of Figs. 3.20 and 3.21. As in traditional aircraft design, the process is initiated with a conceptual design. The design choices are queried and a statistical survey for major dimensions, weight, wing loading concludes the stage with a preliminary design. The choice of wing sections and assessment of static and dynamic stability for the preliminary design is performed. All the components (electrical, propulsive) are selected as they affect the center of gravity location. The application of AM for different parts, selecting different printing orientations and materials to optimize and reduce weight follow. A verification for weight and stability margin is then needed before manufacturing proceeds. If necessary, some of the steps are repeated to achieve an optimized model.

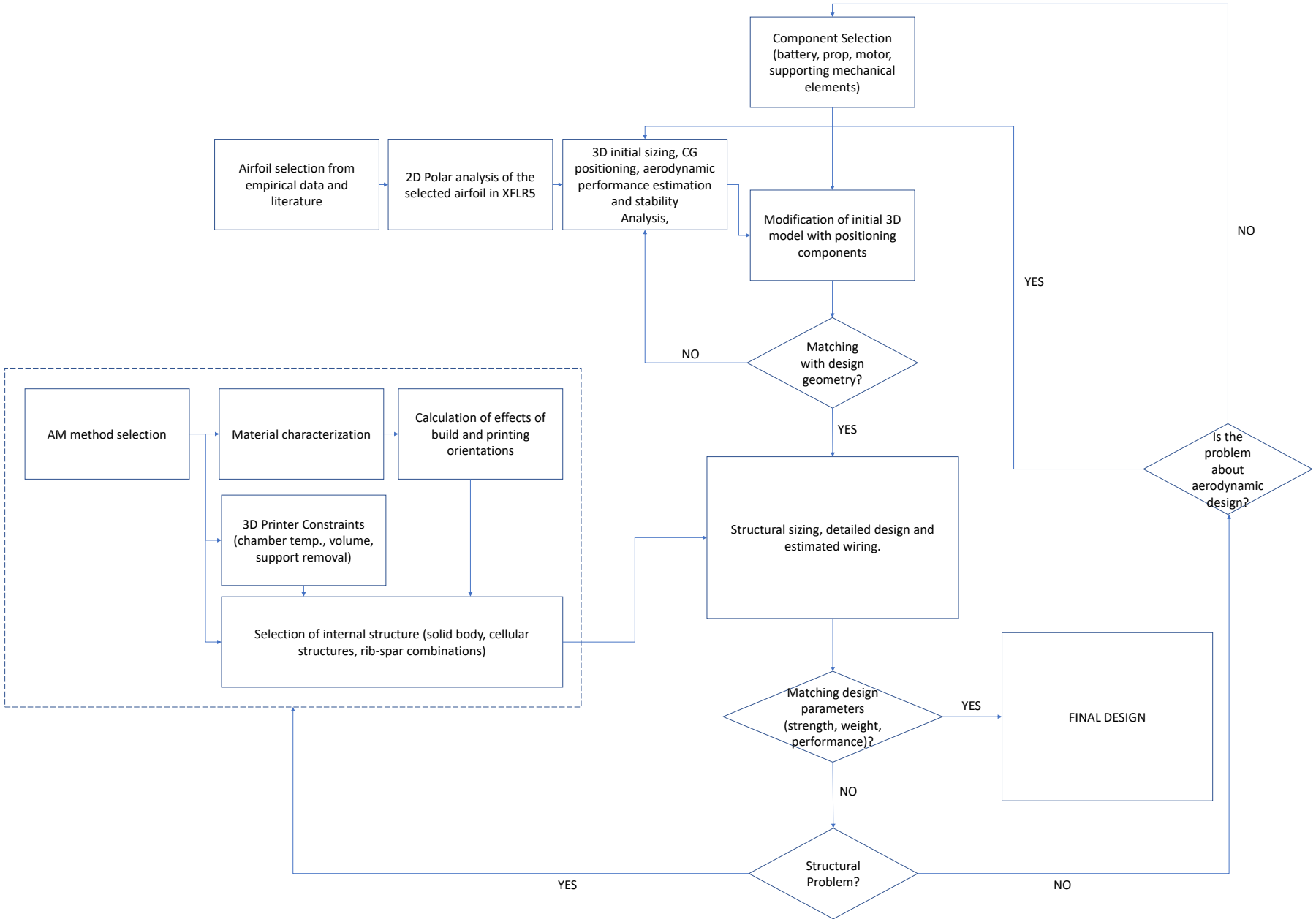

Figure 3.20: Overview of the design procedure.

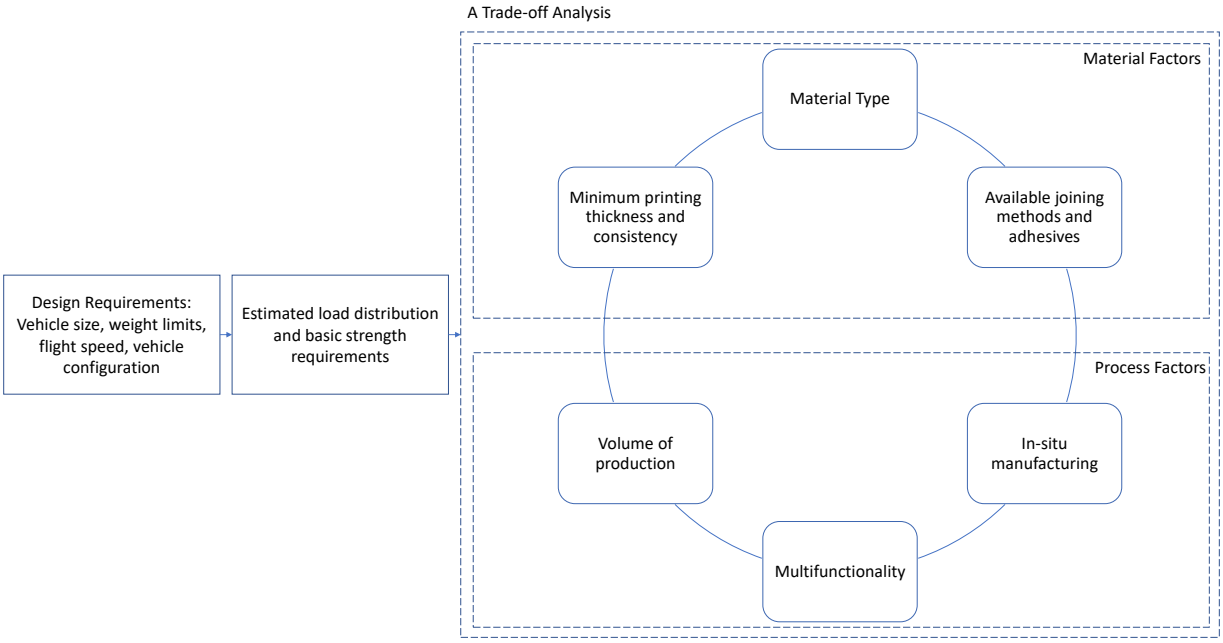

Figure 3.21: AM method selection.

3.8 Summary

- The experiments in this section revealed that build orientation (SU, EU, FU) has a larger impact than print orientation (0-90°) on the elastic deformation of an FDM part. Layer arrangement perpendicular to the direction of the applied tensile load are extremely weak.
- An averaged isotropic model can be used for different print orientations but not for different build orientations as the difference in the flexural stiffness coefficient is more than 10%.
- To build the rib-spar model, a simple FE simulation is performed using the mechanical properties obtained in the three build orientations to determine the maximum stress in a component.

- An ANOVA analysis is carried out to examine the effects of skin thickness, number of ribs, and build orientation on maximum stress of the whole structure. An optimal combination of these parameters is selected for manufacturing of the first model.

- Diamond honeycomb and 3D-Kagome structures are compared for their bending performance. Due to the superior bending performance of diamond honeycomb, it is selected as the interior structure of the wing of the second model. By this manner, the overall structural weight of the system is reduced by approximately 700 g, 35%.

Chapter 4

Mathematical Modeling

4.1 General Equations of Motion

This section presents the general equations of motion of the UAV. It is assumed that the XZ plane of the UAV body axis system is the symmetry plane, the mass of the UAV remains constant, the UAV is a rigid body, and the Earth-Centric-Earth-Fixed (ECEF) frame is assumed to be the inertial reference. Two coordinate systems are used to describe the states of the UAV. The fixed inertial frame points to North-East-Down (NED) of the Earth. The body frame $(O_B; X_B; Y_B; Z_B)$ is located at the center of gravity (CG) of the UAV with the X_B-axis pointing to the front and the Y_B-axis to the right side of the system as seen in Fig. 4.1. The equations of motion are driven based on Newton-Euler methods [120] as

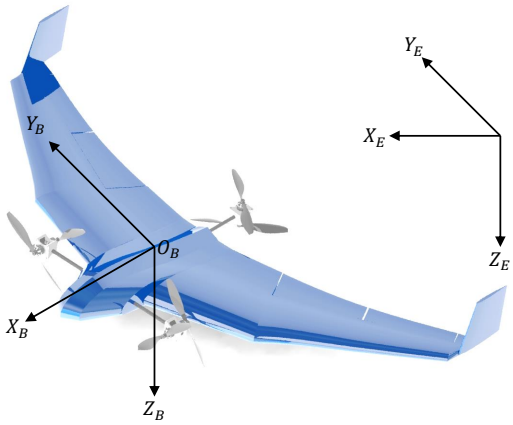

Figure 4.1: Body and Earth Frames.

$$
\begin{aligned}
m(\dot{u} + qw - rv) &= F_{G_X} + F_{A_X} + F_{T_X}, \\
m(\dot{v} + ru - pw) &= F_{G_Y} + F_{A_Y} + F_{T_Y}, \\
m(\dot{w} + pv - qu) &= F_{G_Z} + F_{A_Z} + F_{T_Z}, \\
\dot{p}I_{xx} + qr(I_{zz} - I_{yy}) - (\dot{r} + pq)I_{xz} &= L_A + L_T, \\
\dot{q}I_{yy} - pr(I_{zz} - I_{xx}) + (p^2 - r^2)I_{xz} &= M_A + M_T, \\
\dot{r}I_{zz} + pq(I_{yy} - I_{xx}) + (qr - \dot{p})I_{xz} &= N_A + N_T,
\end{aligned}
\tag{4.1}
$$

where F_* denote forces, and L_*, M_*, N_* denote moments where $* \in \{X, Y, Z\}$ directions of the appropriate coordinate frames. The subscripts A and T stand for aerodynamic and thrust components, respectively, while gravitational forces are shown with F_{G_*} [120]. The mass is as m, while I_* denote the moments of inertia. The translational speed and rotational rate along X_B, Y_B and Z_B are u, v, w and p, q, r, respectively. Finally, the gravitational force components, body angular velocities and the translational equations

can be represented as follows

$$\begin{bmatrix} F_{G_X} \\ F_{G_Y} \\ F_{G_Z} \end{bmatrix} = R \begin{bmatrix} 0 \\ 0 \\ mg \end{bmatrix}, \quad \begin{bmatrix} p \\ q \\ r \end{bmatrix} = R \begin{bmatrix} \dot{\phi} \\ \dot{\theta} \\ \dot{\psi} \end{bmatrix}, \begin{bmatrix} \dot{x} \\ \dot{y} \\ \dot{z} \end{bmatrix} = R_E \begin{bmatrix} u \\ v \\ w \end{bmatrix}, \tag{4.2}$$

where R is Euler rotation matrix from ECEF to the body frame; R_E is the transformation matrix from linear velocities along ECEF frame to the linear velocities along the body frame. Here, ϕ, θ, ψ are roll, pitch and yaw angles, respectively, while x,y, and z are displacements in the fixed inertial frame [120]. In following, two aerodynamic models are presented: (i) a quasi-steady model for flying wing and (ii) an unsteady model for quadplanes.

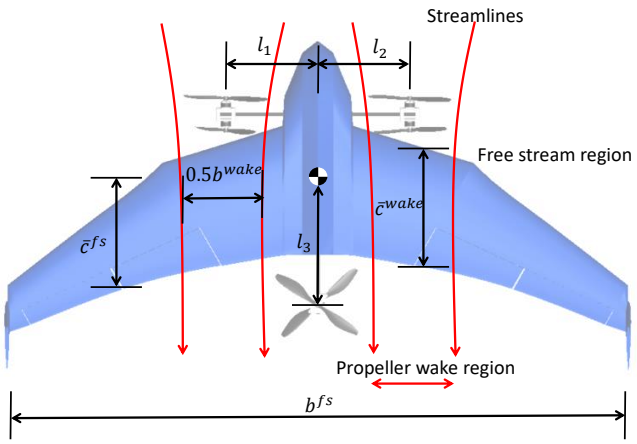

Figure 4.2: Free stream and propeller wake regions on the wing.

4.2 Quasi-steady and Unsteady Models

For aerodynamic modeling of transition motion, quasi-steady and unsteady aerodynamic models are considered and applied to two different configurations, namely a flying wing and a quadplane. Later, the tilting effect on a transiton motion is further investigated on the quadplane configuration (see Chapter 6). At this point, it is necessary to highlight the main differences between these aerodynamic models and the general assumptions made for each model:

Table 4.1: Comparison of specifications of quasi-steady and unsteady models used in this thesis.

Quasi-Steady Flying Wing	**Unsteady Quadplanes**
Developed for whole transition regime in 3DOF.	Developed for whole transition regime in 3DOF.
Lateral-directional effects are calculated only for level flight. To generate the guidance laws for 6DOF, a carrot-chasing algorithm is implemented. For the calculation of spanwise effects during forward flight, DATCOM and ANSYS Fluent are used.	Lateral-directional are not accounted for in this work.
For the modelling of transition regime, multiple linearizations at 10 degree intervals are carried out.	For the transition flight model, directly the nonlinear dynamics is included.
Steady conditions are assumed. In other words, aerodynamic coefficients at a particular angle of incidence is assumed to be constant over time.	Unsteady conditions are assumed, i.e., the changes at aerodynamic loads at the beginning of a sudden change in the flow are taken into account.
For the modelling of flow behind the propellers, a thrust model using propeller disk theory is embedded.	A propeller disk for thrust generation is not included in this model. However, it is assumed that the front and back wings are separated sufficiently far such that the downwash and upwash effects from each other are negligible.
For each linearization, small perturbations and low angle of attack are assumed to be valid as the aircraft body generally remains horizontal.	The unsteady lumped vortex model is considered for the complete flight regime. The model assumes a flat plate which implies that the unsteady moment about the mean aerodynamic center is zero. This assumption does not affect the overall moment calculation significantly since it is much smaller when compared to the moment around the CG generated by the lift forces.

4.3 Aerodynamic Model: Flying Wing Test Case

4.3.1 Tilt-Rotor Flying Wing Configuration

In our approach, we focus on an in-depth aerodynamic model of the flow over the wings. Unlike other applications, in this study, the thrust generation and the propeller downstream are modeled separately for a more accurate aerodynamic representation (see Fig. 4.2). Specifically, the aerodynamic effects of free airstream and propeller-induced airstream are modeled using the aerodynamic data obtained from CFD in ANSYS Fluent and DATCOM analyses. These datasets are used to generate aerodynamic lookup-tables for lift, drag, and moment coefficients. Furthermore, the thrust generation is modeled using the propeller disk theory and embedded into the aerodynamic model. The assumptions made for the derivations are highlighted in each respective section.

4.3.2 Aerodynamic Forces and Moments

Multiple aerodynamic models are generated and integrated over the wing to obtain the total aerodynamic forces and moments. The main components of these models are the free-stream forces/moments and the ones generated on the propeller wake regions. This approach is very similar to the one in [75].

Aerodynamic forces and moments in the free-stream region. The first component of the total aerodynamic model is the free-stream model. This model is generated using the analysis results from DATCOM. Using the aerodynamic data, the force and

moment coefficients can be expressed as:

$$
\begin{aligned}
C_L^{\text{fs}} &= C_{L_0}^{\text{fs}} + C_{L_{\delta_e}}^{\text{fs}}(\delta_e) + \frac{\bar{c}^{\text{fs}}}{2V_\infty}\left[C_{L_{\dot{\alpha}}}^{\text{fs}}\dot{\alpha} + C_{L_q}^{\text{fs}} q\right], \\
C_D^{\text{fs}} &= C_{D_\alpha}^{\text{fs}}(\alpha) + C_{D_{\delta_e}}^{\text{fs}}(\delta_e), \\
C_M^{\text{fs}} &= C_{m_\alpha}^{\text{fs}}\alpha + C_{m_{\delta_e}}^{\text{fs}}\delta_e + \frac{\bar{c}^{\text{fs}}}{2V_\infty}\left[C_{m_{\dot{\alpha}}}^{\text{fs}}\dot{\alpha} + C_{m_q}^{\text{fs}} q\right], \\
C_l^{\text{fs}} &= C_{l_\beta}^{\text{fs}}\beta + C_{l_{\delta_a}}^{\text{fs}}\delta_a + C_{l_{\delta_r}}^{\text{fs}}\delta_r + \frac{b^{\text{fs}}}{2V_\infty}\left[C_{l_p}^{\text{fs}} p + C_{l_r}^{\text{fs}} r\right], \\
C_Y^{\text{fs}} &= C_{Y_\beta}^{\text{fs}}\beta + C_{Y_{\delta_a}}^{\text{fs}}\delta_a + C_{Y_{\delta_r}}^{\text{fs}}\delta_r + \frac{b^{\text{fs}}}{2V_\infty}\left[C_{Y_p}^{\text{fs}} p + C_{Y_r}^{\text{fs}} r\right], \\
C_n^{\text{fs}} &= C_{n_\beta}^{\text{fs}}\beta + C_{n_{\delta_a}}^{\text{fs}}\delta_a + C_{n_{\delta_r}}^{\text{fs}}\delta_r + \frac{b^{\text{fs}}}{2V_\infty}\left[C_{n_p}^{\text{fs}} p + C_{n_r}^{\text{fs}} r\right],
\end{aligned}
\tag{4.3}
$$

where the superscript 'fs' stands for free stream. The force coefficients along the body axes can be obtained as:

$$
\begin{aligned}
C_X^{\text{fs}} &= -C_D^{\text{fs}}\cos(\alpha) + C_L^{\text{fs}}\sin(\alpha), \\
C_Z^{\text{fs}} &= -C_D^{\text{fs}}\sin(\alpha) - C_L^{\text{fs}}\cos(\alpha).
\end{aligned}
\tag{4.4}
$$

Here, it should be noted that, during tilting motion, yaw and roll effects on the angle of attack are not accounted for while they are included for horizontal flight and maneuvers after tilting is completed. Finally, the forces and moments generated on the entire wing by the free-stream airflow can be calculated as

$$
\begin{aligned}
F_{X_B}^{\text{fs}} &= C_X^{\text{fs}}\bar{q}^{\text{fs}}S^{\text{fs}}, \qquad F_{Y_B}^{\text{fs}} = C_Y^{\text{fs}}\bar{q}^{\text{fs}}S^{\text{fs}}, \qquad F_{Z_B}^{\text{fs}} = C_Z^{\text{fs}}\bar{q}^{\text{fs}}S^{\text{fs}}, \\
L_B^{\text{fs}} &= C_l^{\text{fs}}\bar{q}^{\text{fs}}S^{\text{fs}}b^{\text{fs}}, \quad M_B^{\text{fs}} = C_M^{\text{fs}}\bar{q}^{\text{fs}}S^{\text{fs}}\bar{c}^{\text{fs}}, \quad N_B^{\text{fs}} = C_n^{\text{fs}}\bar{q}^{\text{fs}}S^{\text{fs}}b^{\text{fs}},
\end{aligned}
\tag{4.5}
$$

where

$$
\bar{q}^{\text{fs}} = \frac{1}{2}\rho V_\infty^2. \tag{4.6}
$$

Aerodynamic forces and moments in the propeller wake region. The aerodynamic forces, $F_{X_B}^{\text{wake}}$, $F_{Y_B}^{\text{wake}}$, $F_{Z_B}^{\text{wake}}$ and moments, L_B^{wake}, M_B^{wake}, N_B^{wake}, in the propeller wake region can be calculated similarly to previous models. However, in this case, the

velocity of the flow after propellers V_T and the effective angle of attack α_{eff} should be considered (see Fig. 4.4). Moreover, since α_{eff} can be large due to the tilting motions of rotors, the aerodynamic coefficient data collected from DATCOM, which is only valid in the low angle of attack region, cannot be used in this case for longitudinal motion. Instead, a number of computational fluid dynamics (CFD) analyses have been carried out using ANSYS Fluent software to estimate the aerodynamic coefficients of the wing part in the propeller wake region. Using the realizable k-epsilon method, the results in Fig. 4.3 are collected and used for the estimation of aerodynamic properties in this region. For the lateral-directional motion, DATCOM results are used as in the free stream region. Hence, the wake region forces and moment can be written as follows

$$\begin{aligned} F_{X_B}^{\text{wake}} &= C_X^{\text{wake}} \bar{q}^{\text{wake}} S^{\text{wake}}, \\ F_{Y_B}^{\text{wake}} &= C_Y^{\text{wake}} \bar{q}^{\text{wake}} S^{\text{wake}}, \\ F_{z_B}^{\text{wake}} &= C_Z^{\text{wake}} \bar{q}^{\text{wake}} S^{\text{wake}}, \\ L_B^{\text{wake}} &= C_l^{\text{wake}} \bar{q}^{\text{wake}} S^{\text{wake}} b^{\text{wake}}, \\ M_B^{\text{wake}} &= C_M^{\text{wake}} \bar{q}^{\text{wake}} S^{\text{wake}} \bar{c}^{\text{wake}}, \\ N_B^{\text{wake}} &= C_n^{\text{wake}} \bar{q}^{\text{wake}} S^{\text{wake}} b^{\text{wake}}, \end{aligned} \tag{4.7}$$

where

$$\bar{q}^{\text{wake}} = \frac{1}{2} \rho V_T^2. \tag{4.8}$$

Here, b^{wake}, $\bar{c}^{\text{wake}}$ denote the span and mean chord length of the wake region, respectively. Finally, the total aerodynamic forces including all possible propeller induction

and downstream effects can be summarized as

$$
\begin{aligned}
F_{A_X} &= F_{X_B}^{\text{fs}} + F_{X_B}^{\text{wake}}, \\
F_{A_Y} &= F_{Y_B}^{\text{fs}} + F_{Y_B}^{\text{wake}}, \\
F_{A_Z} &= F_{Z_B}^{\text{fs}} + F_{Z_B}^{\text{wake}}, \\
L_A &= L_B^{\text{fs}} + L_B^{\text{wake}}, \\
M_A &= M_B^{\text{fs}} + M_B^{\text{wake}}, \\
N_A &= N_B^{\text{fs}} + N_B^{\text{wake}}.
\end{aligned}
\tag{4.9}
$$

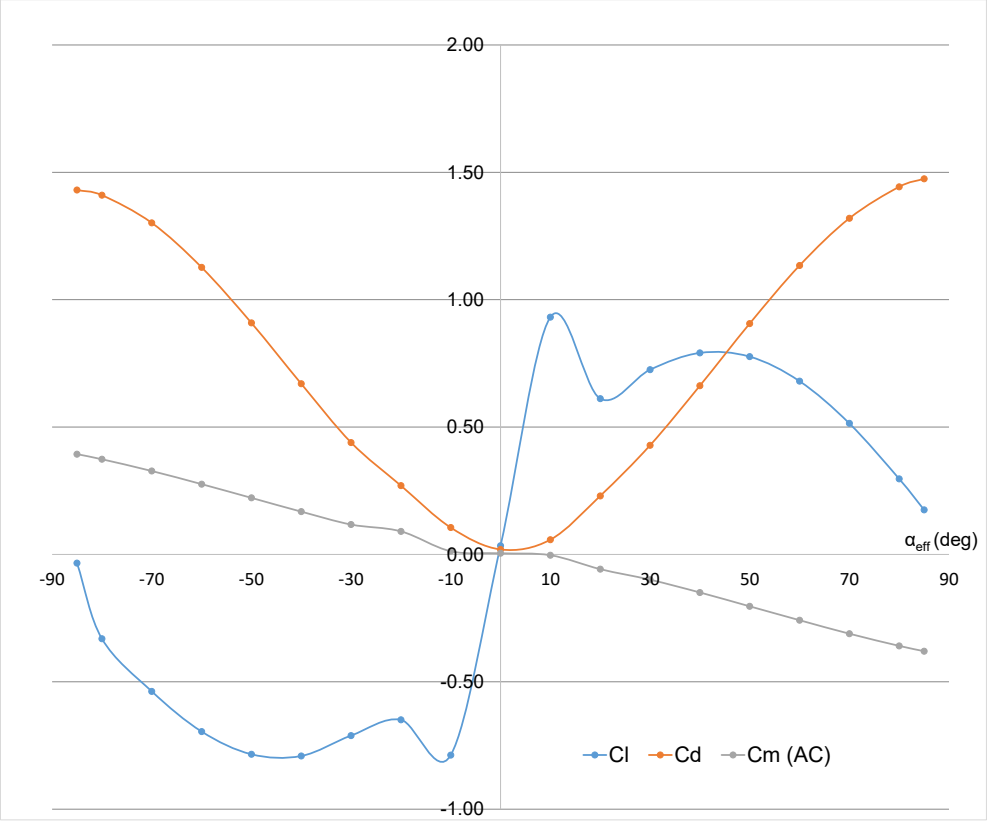

Figure 4.3: Change of the aerodynamic lift, drag, and moment coefficients with respect to angle of attack obtained via CFD behind the propeller stream.

(a)

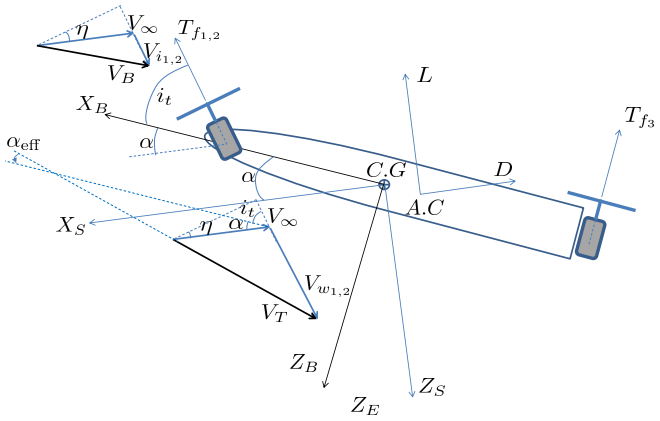

Figure 4.4: Propeller stream, speed vectors and thrust forces.

4.3.3 Propulsive Forces and Moments

As highlighted in Fig. 4.4, the propeller upstream velocity V_B along the body axis is a resultant vector of the free-stream velocity V_∞ and the propeller induction effect V_i. In a similar fashion, the total downstream velocity V_T is obtained using the propeller downstream V_w and V_∞. Thus, the effective angle of attack α_{eff} is the angle between the total flight velocity vector and the body axis of the system. Here, i_t is the tilting angle of the front rotors and α is the aerodynamic angle of attack. Considering the upstream and downstream flow speeds of the propellers, we can write the conservation of momentum and energy equations in the direction normal to the propeller disk [121, 122], and then the thrust T_f generated by the front propellers can be determined as

$$T_f = 2\rho A V_i \sqrt{(V_\infty \sin(i_t + \alpha))^2 + (V_\infty \cos(i_t + \alpha) + V_i)^2}, \tag{4.10}$$

where the induced velocity V_i can appropriately be calculated as in [121, 122]. Accordingly, the velocity of the flow behind the propeller, V_T, and its angle of attack to a

proportion of the wing, α_{eff}, can be obtained as

$$V_T = \sqrt{\left[V_w \xi \sin\left[i_t + \alpha\right]\right]^2 + \left[V_w \xi \cos\left[i_t + \alpha\right] + V_\infty \cos\beta\right]^2}, \tag{4.11}$$

where

$$\begin{aligned} \alpha_{\text{eff}} &= \arctan \frac{V_\infty \sin\alpha - V_w \sin i_t}{V_\infty \cos\alpha + V_w \cos i_t}, \\ V_w &= 2V_i, \\ \xi &= \frac{\pi}{2} - i_t - \alpha. \end{aligned} \tag{4.12}$$

After the completion of the derivation of forces and moments caused by the wake region, forces and moments generated by the rotating propellers along body axes can be acquired as below

$$\begin{aligned} F_{T_X} &= \frac{(T_{\text{f}_1} + T_{\text{f}_2})\cos(i_t)}{m}, \\ L_T &= (T_{\text{f}_1} - T_{\text{f}_2})\sin(i_t) l_1, \\ F_{T_Y} &= 0, \\ M_T &= (T_{\text{f}_1} + T_{\text{f}_2})\sin(i_t) l_2 - T_{\text{f}_3} l_3, \\ F_{T_Z} &= \frac{-(T_{\text{f}_1} + T_{\text{f}_2})\sin(i_t) - T_{\text{f}_3}}{m}, \\ N_T &= (T_{\text{f}_1} - T_{\text{f}_2})\cos(i_t) l_1. \end{aligned} \tag{4.13}$$

Please see Appendix B for the calculation of V_i and V_w.

4.3.3.1 Thrust and Induced Velocity Model

The propeller upstream velocity V_B along the body axis is a resultant vector of the free-stream velocity V_∞ and the propeller induction effect V_i. In a similar fashion, the total downstream velocity is obtained using the output velocity V_{w_*} and V_∞. This, in turn, determines the amount of thrust generated by the front propellers T_{f_*}. Assuming

the total incidence angle ξ to defined as

$$\xi = 90 - i_t - \alpha \tag{4.14}$$

where the i_t is the geometric incidence shown with great exaggeration and α is the aerodynamic angle of attack. Hence, V_B can be calculated as in (4.15)

$$\begin{aligned} V_B &= \sqrt{(V_\infty \cos\xi)^2 + (V_\infty \sin\xi + V_i)^2} \\ &= \sqrt{(V_\infty \sin(i_t+\alpha))^2 + (V_\infty \cos(i_t+\alpha) + V_i)^2} \end{aligned} \tag{4.15}$$

Next, we can write the conservation of momentum and the conservation of energy equations in the direction normal to the propeller disk as below [122]:

$$\begin{aligned} T_f &= \dot{m}(V_\infty \cos(i_t+\alpha) + V_w) - \dot{m}V_\infty \cos(i_t+\alpha) \\ &= \dot{m}V_w \end{aligned} \tag{4.16}$$

$$\begin{aligned} P &= T_f(V_\infty \cos(i_t+\alpha) + V_i) \\ &= \frac{1}{2}\dot{m}\left[V_\infty \cos(i_t+\alpha) + V_w\right]^2 - \frac{1}{2}\dot{m}\left[V_\infty \cos(i_t+\alpha)\right]^2 \\ &= \frac{1}{2}\dot{m}\left[2V_\infty \cos(i_t+\alpha)V_w + V_w^2\right] \end{aligned} \tag{4.17}$$

where P stands for the change of power. From (4.16), (4.17), we conclude a very significant remark:

$$V_w = 2V_i \tag{4.18}$$

Mass flow at the propeller disk is $\rho A V_B$. Then, propeller thrust is

$$\begin{aligned} T &= \dot{m} V_w \\ &= 2\rho A V_i \sqrt{(V_\infty \sin(i_t + \alpha))^2 + (V_\infty \cos(i_t + \alpha) + V_i)^2} \end{aligned} \tag{4.19}$$

Since T depends on V_i, it is necessary to find a way to calculate V_i. For the hover case which is $V_\infty = 0$,

$$V_h^2 = \frac{T}{2\rho A} \tag{4.20}$$

Then,

$$V_i = \frac{V_h^2}{\sqrt{(V_\infty \sin(i_t + \alpha))^2 + (V_\infty \cos(i_t + \alpha) + V_i)^2}} \tag{4.21}$$

The non-dimensional form using the tip speed ΩR of the propeller

$$\begin{cases} \mu = \frac{V_\infty \sin(i_t+\alpha)}{\Omega R} \\ \lambda = \frac{V_\infty \cos(i_t+\alpha)+V_i}{\Omega R} = \frac{V_\infty \cos(i_t+\alpha)}{\Omega R} + \frac{V_i}{\Omega R} = \frac{\mu}{\tan(i_t+\alpha)} + \lambda_i \end{cases} \tag{4.22}$$

So that the non-dimensional induced velocity becomes

$$\lambda_i = \frac{\lambda_h^2}{\sqrt{\mu^2 + \lambda^2}} \tag{4.23}$$

Since it is known that

$$\lambda_h = \sqrt{\frac{C_T}{2}} \tag{4.24}$$

where $C_T = \frac{T}{\rho\pi\Omega^2 R^4}$. Then, (4.23) can be written as

$$\begin{aligned} \lambda_i &= \frac{C_T}{2\sqrt{\mu^2+\lambda^2}} \\ \Rightarrow \lambda &= \frac{\mu}{\tan(i_t+\alpha)} + \frac{C_T}{2\sqrt{\mu^2+\lambda^2}} \end{aligned} \tag{4.25}$$

To solve (4.25), Newton-Raphson method is used. The iteration calculation is

$$\lambda_{n+1} = \lambda_n - \frac{f(\lambda)}{f'(\lambda)} \tag{4.26}$$

where

$$f(\lambda) = \lambda - \frac{\mu}{\tan(i_t+\alpha)} - \frac{C_T}{2\sqrt{\mu^2+\lambda^2}} \tag{4.27}$$

$$f'(\lambda) = 1 + \frac{C_T}{2}\left[\mu^2+\lambda^2\right]^{-3/2} \tag{4.28}$$

Convergence condition is

$$\left|\left|\frac{\lambda_{n+1}-\lambda_n}{\lambda_{n+1}}\right|\right| < 0.1\% \tag{4.29}$$

Finally, we can calculate V_i from C_T and ΩR , which will be detrimental in the aerodynamic performance of the aircraft.

4.4 Unsteady Aerodynamic Modeling: Quadplane Test Case

4.4.1 Pusher and Tilt-Rotor Quadplane Configurations

The pusher and tilt-rotor quadplanes used in this work are inspired by Quadcruiser, a tandem-wing surveillance system developed by Airbus [15]. In the first configuration,

the quadplane has four lifting rotors at the wingtips and a pusher rotor at the rear of the vehicle while in the second configuration, four lifting rotors are provided at the wingtips where the front rotors are capable of tilting from 0° to 90°. The vehicle first operates as a quadrotor to provide necessary thrust to lift up during take-off. Once the vehicle is airborne and in hover mode, the pusher rotor engages in the first configuration. In the second configuration, the front rotors tilt forward to accelerate the vehicle to a sufficient speed, which, in turn, helps in producing lift from the wing surfaces. Simultaneously, thrust from all vertically-oriented rotors in the first configuration and thrust from the back rotors in the second configuration are reduced to zero for an energy efficient forward flight. Longitudinal control is achieved by differential thrust from the rotors as well as the pusher rotor thrust or the tilt-rotor thrust. The selected technical specifications for the vehicle is summarized in Table 4.2. As a final remark, please note that the tilt configuration suggested in this work is not optimal as more complex designs including simultaneous tilting of front and back can be considered as well. In future work, such configurations will also be assessed.

For longitudinal motion considered in this work, all the components of the forces and moments along the body axes are highlighted in Fig. 4.5, which represent a composite side view of both of the configurations. The aerodynamic components can be calculated by

Table 4.2: Common system specifications and design parameters for both configurations.

Specification		Specification	
Airfoil type	NACA0012	Mean aerodynamic chord $\bar{c}$	0.083 m
Take-off weight	1 kg	Front rotor incidence angles	4°
Front and back wingspans b	0.5 m	Back rotor incidence angles	5°
Back rotor moment arms x_b	0.08 m	Inertia along pitching axis I_{yy}	0.006 kgm^2
Front rotor moment arms x_f	0.08 m	Level flight trim speed u	20 m/s
Back rotor vertical offset z_b	0.1 m	Level flight trim pitch angle θ	0°
Front rotor vertical offset z_f	0.0 m		

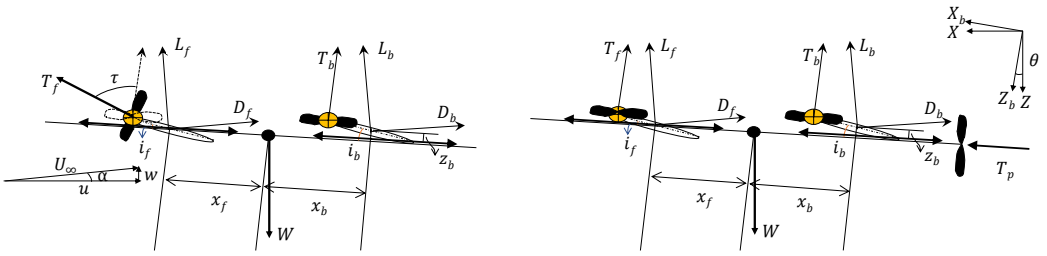

(a) Tilt-rotor configuration. (b) Pusher configuration.

Figure 4.5: Forces and moments acting during longitudinal motion. The dashed lines indicate the tilted position of the front rotors.

$$\begin{aligned} F_{A_X} &= L_f \sin\alpha + L_b \sin\alpha - D_f \cos\alpha - D_b \cos\alpha \\ F_{A_Z} &= -L_f \cos\alpha - L_b \cos\alpha - D_f \sin\alpha - D_b \sin\alpha \\ M_A &= L_f(x_f \cos\alpha - z_f \sin\alpha) + L_b(-x_b \cos\alpha + z_b \sin\alpha) \\ &\quad + D_f(-x_f \sin\alpha - z_f \cos\alpha) + D_b(-x_b \sin\alpha + z_b \cos\alpha) \end{aligned} \quad , \tag{4.30}$$

Furthermore, the propulsive thrust and moment for each configuration will be different. For the pusher, it can be described as

$$\begin{aligned} F_{T_X} &= T_p \\ F_{T_Z} &= -T_f - T_b \\ M_T &= T_f x_f - T_b x_b \end{aligned} \quad , \tag{4.31}$$

whereas for the tilt-rotor configuration, the propulsive thrust and moments are determined as

$$\begin{aligned} F_{T_X} &= T_f \sin\tau \\ F_{T_Z} &= -T_f \cos\tau - T_b \\ M_T &= T_f(x_f \cos\tau - z_f \sin\tau) - T_b x_b \end{aligned} \quad . \tag{4.32}$$

Here, L_f, L_b, D_f, D_b represent the lift and drag at the front and back wings, respectively. x_f and x_b are the moment arms; T_p is the pusher rotor thrust whereas the rotor tilt

angle is denoted by τ. Since the longitudinal control is only considered in this thesis, it is sufficient to model the two front and back rotors by single forces of T_f and T_b, respectively. Also, it should be noted that the lift is perpendicular and drag is parallel to the resultant velocity vector U_∞, where the angle $\alpha = \arctan(w/u)$ is the angle of attack.

4.4.2 Unsteady Aerodynamic Model

One of the novel points in this thesis is the inclusion of unsteady aerodynamic forces and moments in the equations of motion during transition flight of the quadplane without resorting to linearization. For hover flight condition, the vehicle is airborne due to the vertical propellers with no lift generated from the wings. During forward flight, the vehicle relies on the forward flight speed to generated aerodynamic lift and remain airborne. In this context, the equilibrium conditions are significantly different, one hovering at a particular altitude and the other as continuously flying forward to balance the system weight. During transition, the aerodynamic forces increase from zero to the quasi-steady state values. Therefore, linearization for the transition flight regime may lead to instability since the steady state conditions of hover and forward flight are different. For simplicity, the unsteady lumped vortex model is considered in this thesis, which accounts for the complete flight regime. The model assumes a flat plate which implies that the unsteady moment about the mean aerodynamic center is zero. This assumption does not affect the overall moment calculation significantly since it is much smaller when compared to the moment around the center of gravity generated by the lift forces. The second assumption is that the forces are calculated for a two dimensional model. The third and final assumption is that the front and back wings are separated sufficiently far such that the downwash and upwash effects from each other are negligible.

To model unsteady aerodynamics, the lift is computed from the bound vortex

strength around the airfoil. While the airfoil is at the transition phase, the lift changes, which necessitates the formation of an unsteady vortex wake. This vortex wake causes upwash and downwash effects on the airfoil leading to the generation of the unsteady forces. In the unsteady lumped vortex model [9], the bound vortex at the quarter chord $\Gamma(t)$ is sought. To determine the strength of the bound vortex and wake, two conditions must be satisfied. First, the impermeability condition at a collocation point (at three-quarter of the chord length) must be zero [9]. As shown in Fig. 4.6, this condition implies that the normal velocity from the bound vortex $\Gamma(t)$, the normal velocity from the wake vortices and the normal contribution from the free stream is zero. The strength of the bound vortex can be calculated by solving the system of equations in [9] as

$$-\frac{\Gamma(t_N)}{2\pi x_c}+\frac{\Gamma_w(t_N)}{2\pi(x_t+0.5U_N\Delta t)}+U_N\alpha=-\sum_{i=1}^{N-1}\left(\frac{\Gamma_w(t_i)}{2\pi[x_t+(N-i+0.5)U_i\Delta t)]}\right), \tag{4.33}$$

where U_N is a variable velocity at the N^{th} time step, α is the angle of attack and $\Gamma_w(i)$ stands for the circulation of wake. x_c and x_t are the distances of the airfoil circulation and the final wake circulation from the collocation point, respectively. The second condition to determine the bound vortex strength and the wake vortex is the

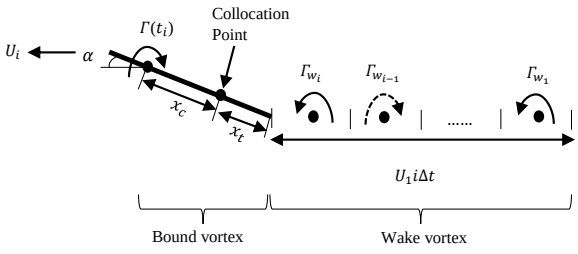

Figure 4.6: Generation of bound and wake vortices at unsteady plunging or acceleration/deceleration adapted from [9].

Helmholtz condition, which implies $\frac{d\Gamma}{dt} = 0$ resulting in

$$\Gamma(t_N) + \Gamma_w(t_N) = -\sum_{i=1}^{N-1} \Gamma_w(t_i). \tag{4.34}$$

Solving (4.33) and (4.34), the unknown wake strength and bound vortex at time t_N can be determined. Eventually, the unsteady lift and drag are calculated by

$$L(t) = \rho \left[U(t)\Gamma(t) + \frac{\partial}{\partial t}\Gamma(t)c \right], \tag{4.35}$$

$$D(t) = \rho \left[w(x,t)\Gamma(t) + \frac{\partial}{\partial t}\Gamma(t)c\alpha \right] + \frac{1}{2}\rho U^2(t) S C_{D_f}, \tag{4.36}$$

where ρ is the air density; c and S are the chord length and wing area, respectively. U is the total speed whereas $w(x,t)$ is the wake-induced downwash and $\Gamma(t)$ is the bound circulation around the airfoil shown in Fig. 4.6. In (4.36), an additional drag term is added to account for the skin friction drag. The flow is assumed to be fully turbulent and $C_{D_f} = 0.027/Re^{\frac{1}{7}}$ where C_{D_f} and Re are the drag coefficient of skin friction and Reynolds number, respectively. Initially, the circulation strength at rest is zero. As the airfoil accelerates from rest, unsteady lift is generated and a wake vortex is formed. At steady state, the wake vortex effect diminishes and no longer contributes to the lift and drag. During backward transition from forward flight to hover, the Kelvin-Helmholtz condition is modified and (4.34) becomes

$$\Gamma(t_N) + \Gamma_w(t_N) = -\sum_{i=1}^{N-1} \Gamma_w(t_i) - \Gamma_{trim}, \tag{4.37}$$

where Γ_{trim} is the circulation at infinity. This term must be added to account for the starting vortex that is present at infinity for a steady forward flight condition.

Figure 4.7 illustrates the differences between an unsteady and a quasi-steady aerodynamic model for a suddenly accelerating flat plate at an incidence angle of 4.5°. As

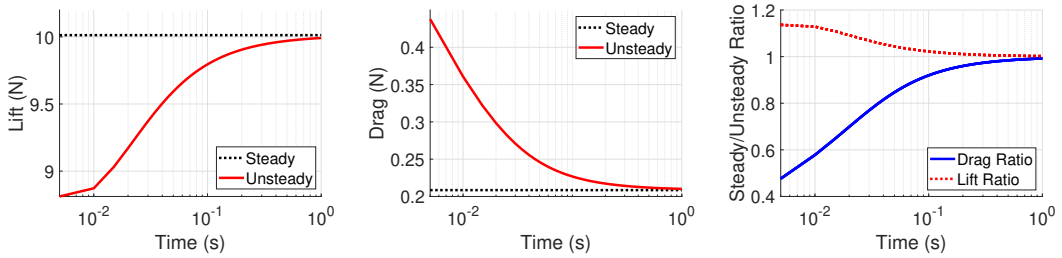

(a) Unsteady, L, and steady, L_{st}, lift.

(b) Unsteady, D, and steady, D_{st}, drag.

(c) Unsteady, D, and steady, D_{st}, force ratios.

Figure 4.7: Comparison of unsteady and steady aerodynamic lift and drag generation on a logarithmic scale at 20 m/s and 4.5°. The difference between the models is more visible at the initial stage of the sudden acceleration motion.

shown, the unsteady forces are significantly different at early stages of motion. As time increases, the forces become similar and quasi-steady results can be assumed to be accurate. This result highlights the importance of including the unsteady effects not only for sudden acceleration but also for inclusion of turbulence and disturbances, which are abrupt sudden motions, as they also affect the forces and controller actions.

4.5 Summary

In this chapter, the basis for the following chapters is established by introducing the general equations of motion along with the quasi-steady and unsteady aerodynamic models. Next, these are implemented to the dynamic models of two distinctive vehicle types, one being a tilt-rotor flying wing and the other being a quadplane in a tilt-rotor and a pusher configuration. For the former, the effect of tilt-rotor propeller stream on the wing is accounted for while it is not calculated in the latter. At the end of the chapter, the significance of the unsteady effects are highlighted, especially at the beginning of the motion. These effects are not accounted for in the quasi-steady model.

Chapter 5

Quasi-Steady Flying Wing

5.1 Introduction

This section describes the methodology for the control of a tilt-rotor VTOL UAV. It is a modified flying wing with tilting rotors to enable vertical flight as seen in Fig. 5.1a. With increasing rotor angles, it has a tendency to act more like a multi-rotor system whereas the steady level flight is obtained when the rotors are positioned horizontally. The view of an approximate full flight trajectory is shown in Fig. 5.1b. Due to the complex aerodynamic characteristics of the proposed configuration, the controller structure consists of a level of stability augmentation systems (SASs), control augmentation systems (CASs), and guidance laws as shown in Fig. 5.2. Control inputs are elevator, aileron deflections and the differential thrust generated by the rotors. To control the pitch motion, elevators and the differential thrust between the front and back rotors are used. In the same fashion, lateral and directional control is carried out using the aileron input and the thrust difference between the right-hand side and left-hand side rotors. There is no separate rudder unit on this system so the rolling and yawing motion are controlled together. The significant aircraft design parameters are listed in Table 5.1. The tilt rate of the rotors are initally kept constant. Then, a fuzzy logic

based switching algorithm is designed for a smoother transition flight.

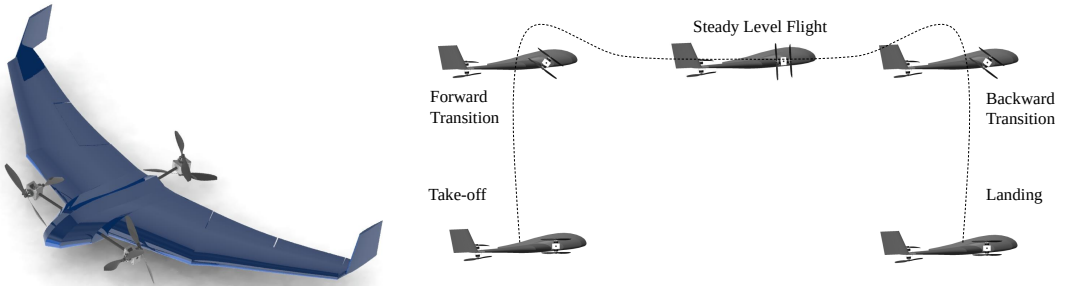

(a) Model of the UAV. (b) Flight regime.

Figure 5.1: (a) tilt-rotor blended wing-body VTOL UAV model and (b) the flight regime. The UAV takes off vertically, transits to the steady level flight, then transits back to the hover mode, and lands.

5.2 Controller Design

5.2.1 Trim Analysis

Before designing any controllers, trim conditions of the vehicle should be determined. A trim can be achieved at a steady-state flight condition in multiple manners with different combinations of throttle input and control surface deflections. For example, the trim at 70° rotor tilting can be obtained by 55% rotor thrust and 5° elevator deflection or 75% rotor thrust and 0° elevator deflection. To select one of the possible

Table 5.1: System configuration and design parameters.

Specification	
Airfoil type	MH61
Take-off weight m	3.8 kg
Wingspan b	1.61 m
Mean aerodynamic chord $\overline{c}$	0.272 m
Distance between front propellers	0.6 m
Distance between front and rear propellers	0.6 m
Moment of inertia I_{xx}	0.3794 kgm^2
Moment of inertia I_{yy}	0.1002 kgm^2
Moment of inertia I_{zz}	0.4755 kgm^2
Moment of inertia I_{xz}	–0.0064 kgm^2

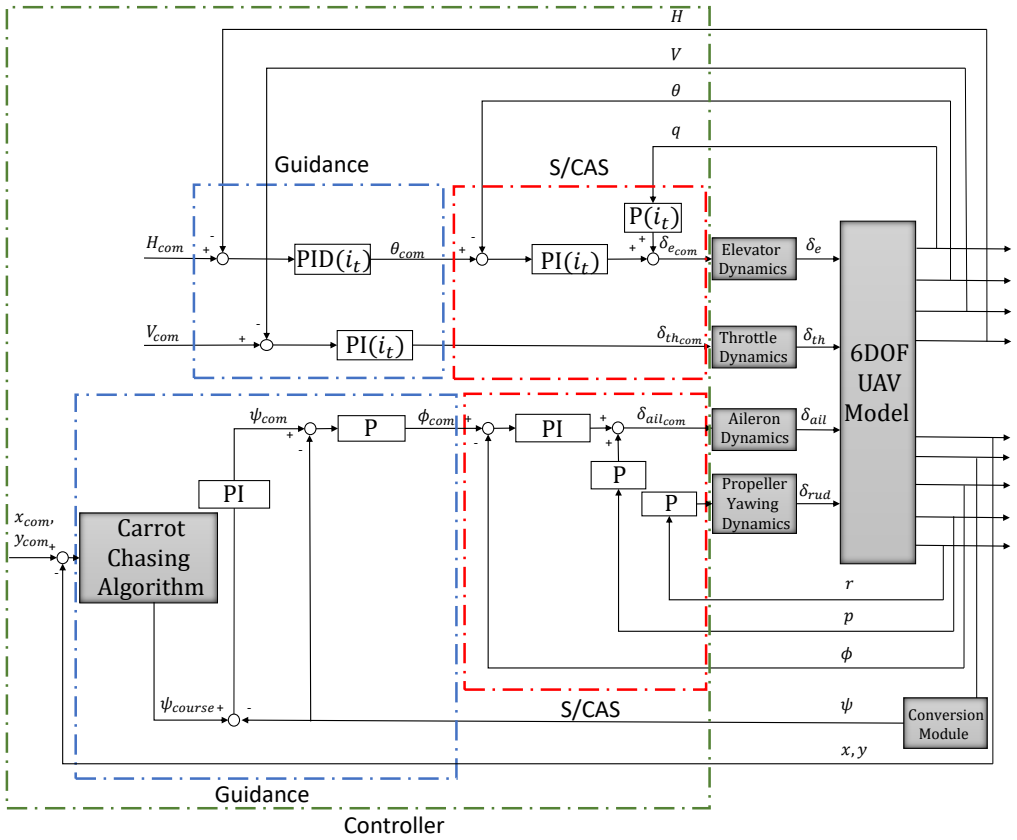

Figure 5.2: Cascaded controller structure of the tilt-rotor UAV: (i) outer loops for the guidance control, (ii) SAS and CAS loops for attitude control.

trim conditions, a weighing matrix is used to determine relative importance of control inputs and desired states. In this analysis, the changes in the particularly throttle-controlled states are penalized with higher weights since control surface deflections are more energy efficient than changing the throttle inputs [7]. Then, the trim condition is determined using a performance index in the form of a cost function dependent on these weights. The condition minimizing the cost is considered to be the trim condition. Keeping in mind that the rear propellers are not utilized for fixed-wing level flight and that the control surfaces are not efficient during vertical take-off and landing, the trim conditions during tilting motion are determined as follows.

The vector input for the trim search is:

$$x_{full} = [x_E\ y_E\ z_E\ \phi\ \theta\ \psi\ V_T\ \alpha\ \beta\ p\ q\ r\ T_T\ T_e\ T_a\ T_r\ T_{rear}\ \delta_e\ \delta_a\ \delta_r]^T. \tag{5.1}$$

The first 12 parameters in this vector are the states and the remaining 9 parameters are the trim and control inputs. Here, x_E, y_E, z_E denote the position of the vehicle in Earth frame; ϕ, θ, ψ are the attitude angles whereas p, q, r are the angular rates; V_T is the total speed and α, β are the angle of attack and sideslip angle, respectively. The control inputs total throttle, pitching, rolling and yawing differential thrust, elevator, aileron and rudder deflections are denoted by T_T, T_e, T_r, T_a, δ_e, δ_a, δ_r, respectively. This vector is input as initial conditions to the nonlinear 6-DOF mathematical model. The initial values of these parameters are zero except for V_T, T_T, T_{rear}. When finding the trim condition, the first 12 states are selected as the criteria. Hence, we define a vector as

$$x_{cost} = [x_E\ y_E\ z_E\ \phi\ \theta\ \psi\ V_T\ \alpha\ \beta\ p\ q\ r]^T \tag{5.2}$$

The corresponding trimming weights for these 12 terms are:

$$R_{Trim} = [0\ 0\ 5\ 5\ 10\ 10\ 100\ 10\ 10\ 10\ 100\ 10]^T, \tag{5.3}$$

where the gains are selected based on experience. This matrix will be further investigated in future work for better efficiency. Hence, the cost function to be minimized is found by [78]:

$$J_{Trim} = R_{Trim} x_{cost} \odot x_{cost}^T \tag{5.4}$$

where $\odot$ indicates Hadamard product and $\min_{\forall x_{cost}} J_{Trim}$.

For the trim analysis, trim conditions of the 10 linearized models are obtained. The arrays of trim speed, percentages of total and rear rotor throttle are selected as follows:

$$
\begin{aligned}
V_{T_i} &= [20, 17, 16, 14, 12, 11, 08, 05, 03, 01], \\
T_{T_i} &= [60, 60, 70, 70, 70, 20, 70, 70, 70, 70], \\
T_{rear_i} &= [00, 00, 70, 70, 70, 90, 70, 60, 70, 70].
\end{aligned} \tag{5.5}
$$

These parameters are selected based on trial-and-error and estimations. In future studies, the selection of these arrays could also be optimized.

To determine a trim condition, we examine whether the cost is sufficiently small. The cost function indicates the changes between the initial conditions and the time next step after the initial conditions. To search for a local minimum of the cost, we utilize the *fminsearch* function in MATLAB. If the difference between two time steps is too high, then the cost will be too high, from which it can be concluded that the trim condition is achieved but at a very high cost. Then, we re-initialize *fminsearch* for the model with a slightly modified initial condition for another trim search, which would require less effort to obtain. By this manner, the nonlinear plant with all its parameters are evaluated for the trim condition.

A sample trim condition calculated for the given cost vector and the weight matrix for level flight condition is shown in Table 5.2. In this table, it is seen that the total throttle is at approx. 57% of the total available thrust, and the back rotor is silent. Besides, the elevator deflection is almost at 1° and the angle of attack is almost zero whereas the trim speed is 20 m/s. The same technique is applied throughout the transition flight with all linear models. The linear controllers in the following sections are designed with respect to these trim conditions.

5.2.2 Linear Controller Development: SAS and CAS

For the controller development for the vehicle, two strategies are followed. In the first method, a set of P/PI/PID controllers with the linearized longitudinal and lateral-directional models are implemented. In this technique, the approach to tune the con-

Table 5.2: A sample trim condition for level flight with the given weight matrix. The same method is applied at all 10 models.

Term	Value
Cost term	$J_{Trim} = 1.2371 \times 10^{-28}$
Total thrust	$T_{f_3} + T_{f_2} + T_{f_1} = T_{total} = 56.9771\%$
Rear thrust	$T_{f_3} = 0\%$
Elevator deflection	$\delta_e = 0.91229°$
Angle of attack	$\alpha = 0.051917°$
Total speed	$V_T = 20$m/s

trollers is based on the minimization of the tracking error functions, which will be defined in the following section. The idea is first to stabilize the aircraft using a stability augmentation system (SAS), then to obtain the attitude control with a control augmentation system (CAS). Finally, after controlling the so-called "inner loop", the vehicle position and velocity control are achieved in the guidance loop. Later, in the second method, we use a T2-FNN controller to enhance both the S/CAS and guidance loop performances. The motivation for this application is to overcome the effect of linearization at the tilting angles in-between the models. In both cases, actuator dynamics are included in the designs of the controllers.

One should note that the linear models are written by accounting for the deviations from the desired states. This leads to the fact that the references are fed as changes/deviations from the current states as well. However, in the nonlinear model, the states are defined as the total values of each state. Therefore, the linear models deal with the changes from the desired values whereas the nonlinear model directly represent the states. Accordingly, the linear model of the system would comprise the state vector below

$$x = [x_E \ y_E \ z_E \ \phi \ \theta \ \psi \ V_T \ \alpha \ \beta \ p \ q \ r]^T, \tag{5.6}$$

which can be decomposed to the following longitudinal and lateral-directional states near a steady-flight condition with the assumptions of small angle of attack and negli-

gibly small perturbations:

$$\begin{aligned} x_{lon} &= [V_T \quad \alpha \quad q \quad \theta]^T, \\ x_{lat} &= [\beta \quad \phi \quad p \quad r]^T. \end{aligned} \tag{5.7}$$

To model the dynamics of control surfaces and motors, first-order lag systems with time constants of $T_{cs} = 0.15s$ and $T_{th} = 0.05s$ are designed, respectively. The cascaded system of SAS, CAS and actuator dynamics are formulated as

$$\dot{x}_i = A_i x_i + B_i x_{a_i}, (i = \text{lon}, \text{lat}) \tag{5.8}$$

where x_{a_i} is the control input to the above augmented system. All control input are listed as follows

$$\begin{aligned} x_{a_{lon}} &= \begin{bmatrix} \delta_e & \delta_{e_{pw}} & \delta_T \end{bmatrix}^T \\ x_{a_{lat}} &= \begin{bmatrix} \delta_{\text{a}} & \delta_{\text{a}_{\text{pw}}} & \delta_{\text{r}} & \delta_{\text{r}_{\text{pw}}} \end{bmatrix}^T \end{aligned} \tag{5.9}$$

Unlike in the longitudinal motion where the elevator and the pitching effect caused by differential thrust between the front and back rotors, roll and yaw rate control inputs are selected to affect on each individual channel separately. Since this setup does not have any separate rudder unit, roll rate is controlled by the aileron input whereas the yaw rate is controlled by the differential thrust between right- and left-hand side rotors. Hence, the lateral-directional control inputs are reduced to

$$x_{a_{lat}} = \begin{bmatrix} \delta_{\text{a}} & \delta_{\text{r}_{\text{pw}}} \end{bmatrix}^T \tag{5.10}$$

5.2.2.1 SAS for Longitudinal Motion

For longitudinal motion, q, θ, and H control will be achieved in a cascaded scheme as in Fig. 5.2. As described in the previous section, the actuator model will be analyzed

together with the longitudinal motion model. For SAS design, we have

$$\begin{aligned} \dot{x}_{lon} &= A_{lon}x_{lon} + B_{lon}x_{a_{lon}}, \\ \dot{x}_{a_{lon}} &= A_a x_{a_{lon}} + B_a u_{lon}. \end{aligned} \tag{5.11}$$

Here,

$$A_a = \begin{bmatrix} -1/T_{cs} & 0 \\ 0 & -1/T_{th} \end{bmatrix}, B_a = \begin{bmatrix} K_{cs}/T_{cs} & 0 \\ 0 & K_{th}/T_{th} \end{bmatrix}. \tag{5.12}$$

Please note that K_{cs} and K_{th} are the efficiency factors of elevator deflection and differential thrust for pitching, respectively. These parameters vary from 0 to 1 from level flight condition to VTOL. At SAS level,

$$\begin{aligned} x_{a_{lon}} = x_{a_{SAS}} &= \begin{bmatrix} \delta_e & \delta_{e_{pw}} \end{bmatrix}^T, \\ u_{lon} = u_{SAS} &= \begin{bmatrix} \delta_{e_{com}} & \delta_{e_{pw_{com}}} \end{bmatrix}^T. \end{aligned} \tag{5.13}$$

The subscript *com* indicates the commanded actuator changes. However, due to the actuator dynamics, the actuator output will not be the same with u_{SAS} and will be $x_{a_{SAS}}$. Then, the control input can be rewritten in the form of longitudinal states such that

$$u_{SAS} = \begin{bmatrix} K_{q_e} q \\ K_{q_{pwe}} q \end{bmatrix} = \begin{bmatrix} K_{q_e} C_q x_{lon} \\ K_{q_{pwe}} C_q x_{lon} \end{bmatrix}, \tag{5.14}$$

where

$$C_q = \begin{bmatrix} 0 & 0 & 1 & 0 \end{bmatrix}. \tag{5.15}$$

Finally, the state matrix of the augmented system can be written by adding the actuator dynamics as follows:

$$\begin{aligned}\begin{bmatrix}\dot{x}_{lon}\\ \dot{x}_a\end{bmatrix} &= \begin{bmatrix}A_{lon} & B_{lon}\\ 0 & A_a\end{bmatrix}\begin{bmatrix}x_{lon}\\ x_a\end{bmatrix} + \begin{bmatrix}0\\ B_a\end{bmatrix}\begin{bmatrix}K_{q_e}C_q x_{lon}\\ K_{q_{pwe}}C_q x_{lon}\end{bmatrix}\\ &= \begin{bmatrix}A_{lon} & B_{lon}\\ B_a\begin{bmatrix}K_{q_e}C_q\\ K_{q_{pwe}}C_q\end{bmatrix} & A_a\end{bmatrix}\begin{bmatrix}x_{lon}\\ x_a\end{bmatrix} = A_{SAS}\begin{bmatrix}x_{lon}\\ x_a\end{bmatrix}.\end{aligned} \tag{5.16}$$

At the SAS stage, we try to stabilize the system. For this purpose, in defined ranges for K_{q_e} and $K_{q_{pwe}}$, we search for $\max|Re(\lambda_n)|$ when $Re(\lambda_n) \leq 0$, where λ_n is the eigenvalue of A_{SAS} of any n_{th} model. By this manner, the controller gain K_q is selected. At some tilting angles, $Re(\lambda_n) \geq 0$. Therefore, SAS cannot stabilize all the models and the remaining unstable models should be stabilized in the CAS level.

5.2.2.2 CAS for Longitudinal Motion

For CAS design, we use a PI controller as in Fig. 5.2, unlike in SAS design. It should have drawn the attention of the reader that, in SAS design, the pitch rate signal q is directly amplified by two gains, K_{q_e}, and $K_{q_{pwe}}$, respectively. In CAS, θ is controlled as below:

$$u_{CAS} = K_\theta(\theta_{com} - \theta) + K_{i\theta}z. \tag{5.17}$$

Here, we define the error dynamics with z_θ such that

$$\dot{z}_\theta = e_\theta = (\theta_{com} - \theta) = \theta_{com} - C_\theta x_{lon}. \tag{5.18}$$

Similarly to SAS,

$$\begin{aligned} C_q &= \begin{bmatrix} 0 & 0 & 1 & 0 \end{bmatrix}, \\ C_\theta &= \begin{bmatrix} 0 & 0 & 0 & 1 \end{bmatrix}. \end{aligned} \tag{5.19}$$

Thus, the total longitudinal control input can be written as:

$$u_{lon} = u_{SAS} + u_{CAS} = \begin{bmatrix} \delta_{e_{com}} \\ \delta_{e_{pwcom}} \end{bmatrix} = \begin{bmatrix} K_{q_e} C_q x_{lon} + K_\theta(\theta_{com} - C_\theta x_{lon}) + K_{i\theta} z \\ K_{q_{pwe}} C_q x_{lon} + K_\theta(\theta_{com} - C_\theta x_{lon}) + K_{i\theta} z \end{bmatrix}. \tag{5.20}$$

Then, the augmented state matrix is expanded by adding error dynamics such that

$$\begin{aligned} \begin{bmatrix} \dot{x}_{lon} \\ \dot{x}_a \\ \dot{z}_\theta \end{bmatrix} &= \begin{bmatrix} A_{lon} & B_{lon} & 0 \\ B_a \begin{bmatrix} K_{q_e} C_q - K_\theta C_\theta \\ K_{q_{pwe}} C_q - K_\theta C_\theta \end{bmatrix} & A_a & B_a \begin{bmatrix} K_{i\theta} \\ K_{i\theta} \end{bmatrix} \\ -C_\theta & 0 & 0 \end{bmatrix} \begin{bmatrix} x_{lon} \\ x_a \\ z_\theta \end{bmatrix} \\ &+ \begin{bmatrix} 0 \\ B_a \begin{bmatrix} K_\theta \\ K_\theta \end{bmatrix} \\ 1 \end{bmatrix} \theta_{com} = A_{CAS} \begin{bmatrix} x_{lon} \\ x_a \\ z_\theta \end{bmatrix} + B_{CAS} \theta_{com}. \end{aligned} \tag{5.21}$$

After obtaining 5.21, for the cases of $Re(\lambda_n) \leq 0$, the condition of $\max|Re(\lambda_n)|$ of A_{CAS} is determined for the stability of any n_{th} model. In following, the pair of K_θ and $K_{i\theta}$ is selected by minimizing a basic performance index $J = \int e_\theta^2 dt$, where the index indicates a cost calculated with respect to the total amount of attitude error of the vehicle, e_θ. This strategy is further applied to the altitude controller and the speed controller. However, it is noteworthy that altitude and speed controllers are affected by the total throttle, too. Hence, the control inputs can be summarized as following

functions:

$$\begin{cases} u_{SAS} = f\left(K_{q_e}, K_{q_{pw_e}}, q\right) \\ u_{CAS} = u_{SAS} + g\left(\theta_{com}, \theta\right) \\ u_V = i\left(u_{SAS} + u_{CAS}, j\left(V_{com}, V_T\right)\right) \\ u_H = k\left(k\left(H_{com}, u_V\right)\right) \end{cases} \tag{5.22}$$

5.2.2.3 Speed Controller (PI)

Speed control is achieved directly by manipulating the total throttle, which is the total rotation speed of the rotors. Therefore, the actuator matrix is expanded by one dimension as:

$$x_{a_V} = \begin{bmatrix} \delta_e \\ \delta_{e_{pw}} \\ \delta_T \end{bmatrix}. \tag{5.23}$$

The controller to be used is a PI controller. Therefore, the error dynamics should also differ from the previous cases in that

$$\dot{z}_V = e_V = (V_{com} - V) = V_{com} - C_V x_{lon}, \tag{5.24}$$

where

$$C_V = \begin{bmatrix} 1 & 0 & 0 & 0 \end{bmatrix}. \tag{5.25}$$

Thus, the augmented model will be in the form of

$$\begin{aligned} \dot{x}_{lon} &= A_{lon} x + B_{lon} x_a, \\ \dot{x}_{a_V} &= A_{a_V} x_{a_V} + B_{a_V} u_V. \end{aligned} \tag{5.26}$$

Here,

$$A_{a_V} = \begin{bmatrix} -1/T_{cs} & 0 & 0 \\ 0 & -1/T_{th} & 0 \\ 0 & 0 & -1/T_{th} \end{bmatrix}, B_{a_V} = \begin{bmatrix} K_{cs}/T_{cs} & 0 & 0 \\ 0 & K_{th}/T_{th} & 0 \\ 0 & 0 & K_{th}/T_{th} \end{bmatrix}. \quad (5.27)$$

The controller input will be

$$u_V = K_V e_V + K_{iV} \int_0^t e_V dt = \begin{bmatrix} \delta_{e_{com}} \\ \delta_{e_{pw_{com}}} \\ \delta_{T_{com}} \end{bmatrix}. \quad (5.28)$$

The next steps will be combining the longitudinal state matrix with the actuator matrix as well as the speed error dynamics. The augmented model is first written in the form

of θ_{com} and V_{com} as follows:

$$\begin{bmatrix} \dot{x}_{lon} \\ \dot{x}_a \\ \dot{z}_\theta \\ \dot{z}_V \end{bmatrix} = \begin{bmatrix} A_{lon} & B_{lon} & 0 & 0 \\ B_a \begin{bmatrix} K_{q_e} C_q - K_\theta C_\theta \\ K_{q_{pw_e}} C_q - K_\theta C_\theta \\ -K_V C_V \end{bmatrix} & A_a & B_a \begin{bmatrix} K_{i\theta} \\ K_{i\theta} \\ 0 \end{bmatrix} & B_a \begin{bmatrix} 0 \\ 0 \\ K_{iV} \end{bmatrix} \\ -C_\theta & 0 & 0 & 0 \\ -C_V & 0 & 0 & 0 \end{bmatrix} \begin{bmatrix} x_{lon} \\ x_a \\ z_\theta \\ z_V \end{bmatrix} + \begin{bmatrix} 0 \\ B_a \begin{bmatrix} K_\theta \\ K_\theta \\ 0 \end{bmatrix} \\ 1 \\ 0 \end{bmatrix} \theta_{com} + \begin{bmatrix} 0 \\ B_a \begin{bmatrix} 0 \\ 0 \\ K_V \end{bmatrix} \\ 0 \\ 1 \end{bmatrix} V_{com}, \tag{5.29}$$

which can be reorganized as

$$\begin{bmatrix} \dot{x}_{lon} \\ \dot{x}_a \\ \dot{z}_\theta \\ \dot{z}_V \end{bmatrix} = \begin{bmatrix} A_{lon} & B_{lon} & 0 \\ B_a \begin{bmatrix} K_{q_e}C_q - K_\theta C_\theta \\ K_{q_{pwe}}C_q - K_\theta C_\theta \\ -K_V C_V \end{bmatrix} & A_a & B_a \begin{bmatrix} K_{i\theta} & 0 \\ K_{i\theta} & 0 \\ 0 & K_{iV} \end{bmatrix} \\ -C_\theta & 0 & 0 \\ -C_V & 0 & 0 \end{bmatrix} \begin{bmatrix} x_{lon} \\ x_a \\ z_\theta \\ z_V \end{bmatrix} + \begin{bmatrix} 0_{4\times 2} \\ B_{a_{3\times 3}} \begin{bmatrix} K_\theta & 0 \\ K_\theta & 0 \\ 0 & K_V \end{bmatrix} \\ 1 \quad 0 \\ 0 \quad 1 \end{bmatrix}_{9\times 2} \begin{bmatrix} \theta_{com} \\ V_{com} \end{bmatrix} = A_V x_V + B_V \begin{bmatrix} \theta_{com} \\ V_{com} \end{bmatrix}. \tag{5.30}$$

Then, in a similar fashion to CAS, the controller gains K_V and K_{iV} are determined.

5.2.2.4 Altitude Controller (PID)

The most outer loop of this cascaded controller is the altitude controller. It is designed slightly different than CAS and speed controllers. The altitude reference H_{com} is given by the pilot. The PID controller generates the reference θ_{com} for the pitch controller. The error dynamics of altitude can be found by

$$\dot{z}_H = e_H = H_{com} - H, \tag{5.31}$$

whereas the control input can be calculated by

$$u_H = \theta_{com} = K_H e_H + K_{iH} e_{iH} + K_{dH} \dot{e}_H. \tag{5.32}$$

Since we also define a D gain, we need to define a pseudo-derivative of the error, which will be used in the augmented states matrix:

$$\dot{e}_H \approx \dot{\eta}_H = (-1/T_{del})\eta + (1/T_{del})e_H, \tag{5.33}$$

where T_{del} is a time constant for delay, which can be selected in the interval of $T_{del} = [0.1, 0.15]$. Instead of writing the matrix in an open form, we prefer directly using the control system obtained in the speed controller design stage and write it in the closed form of the equations as follows:

$$\begin{bmatrix} \dot{x}_V \\ \dot{H} \\ \dot{z}_H \\ \dot{\eta}_H \end{bmatrix} = \begin{bmatrix} A_V x_V + B_V \begin{bmatrix} u_H & V_{com} \end{bmatrix}^T \\ (V_{Trim} + V_T)\sin(\theta - \alpha) \\ e_H \\ (-1/T_{del})\eta + (1/T_{del})e_H \end{bmatrix}. \tag{5.34}$$

Here, it should be noted that the trim altitude change is defined as $\dot{H} = (V_{Trim} + V_T)\sin(\theta - \alpha)$, where V_{Trim} is the trim speed of any n_{th} model. With given altitude reference, this system of differential equations can be solved with *ode*45 function in MATLAB.

5.2.2.5 SAS for Lateral - Directional Control

For lateral-directional motion control, the controller structure differs considerably from the longitudinal motion control, especially in the guidance level as shown in Fig. 5.2. Besides, it should also be noted that, the lateral-directional controller is developed

only for the level flight condition as it is impractical to maneuver to other directions during tilting motion. In the most inner loop, p, and r are input to SAS. The actuator model is again analyzed together with the linearized motion model:

$$\begin{aligned} \dot{x}_{lat} &= A_{lat}x_{lat} + B_{lat}x_{a,lat}, \\ \dot{x}_{a,lat} &= A_{a,lat}x_{a,lat} + B_{a,lat}u_{lat}. \end{aligned} \tag{5.35}$$

Since there is no rudder on this vehicle, yaw control is carried out via the differential thrust between the front rotors and the back rotors while the roll control is achived with aileron deflection. Therefore, the actuator vector along with its system and control matrices are

$$x_{a,lat} = \begin{bmatrix} \delta_{r_{pw}} \\ \delta_a \end{bmatrix}, A_{a,lat} = \begin{bmatrix} -1/T_{th} & 0 \\ 0 & -1/T_{cs} \end{bmatrix}, B_{a,lat} = \begin{bmatrix} K_{th}/T_{th} & 0 \\ 0 & K_{cs}/T_{cs} \end{bmatrix}. \tag{5.36}$$

For SAS design, we have

$$u_{SAS,lat} = \begin{bmatrix} \delta_{r_{pw_{com}}} \\ \delta_{a_{com}} \end{bmatrix} = \begin{bmatrix} K_{p_r}C_r x_{lat} \\ K_{p_p}C_p x_{lat} \end{bmatrix}, \tag{5.37}$$

where

$$C_p = \begin{bmatrix} 0 & 0 & 1 & 0 \end{bmatrix}, C_r = \begin{bmatrix} 0 & 0 & 0 & 1 \end{bmatrix}. \tag{5.38}$$

Then, the augmented system matrix becomes

$$\begin{aligned}\begin{bmatrix}\dot{x}_{lat}\\ \dot{x}_{a,lat}\end{bmatrix} &= \begin{bmatrix}A_{lat} & B_{lat}\\ 0_{2\times4} & A_{a,lat}\end{bmatrix}\begin{bmatrix}x_{lat}\\ x_{a,lat}\end{bmatrix} + \begin{bmatrix}0_{4\times2}\\ B_{a,lat}\end{bmatrix}\begin{bmatrix}K_{p_r}C_r x_{lat}\\ K_{p_p}C_p x_{lat}\end{bmatrix}\\ &= \begin{bmatrix}A_{lat} & B_{lat}\\ B_a\begin{bmatrix}K_{p_r}C_r\\ K_{p_p}C_p\end{bmatrix} & A_{a,lat}\end{bmatrix}\begin{bmatrix}x_{lat}\\ x_{a,lat}\end{bmatrix} = A_{SAS,lat}\begin{bmatrix}x_{lat}\\ x_{a,lat}\end{bmatrix}.\end{aligned} \tag{5.39}$$

Similarly to the longitudinal SAS, we try to stabilize the system at the lateral-directional SAS level. In defined ranges for K_{p_p} and K_{p_r}, we search for $\max|Re(\lambda_{lat})|$ when $Re(\lambda_{lat}) \leq 0$, where λ_{lat} is the eigenvalue of $A_{SAS,lat}$ of the level flight model. By this manner, these controller gains are selected.

5.2.2.6 CAS for Lateral - Directional Control

In the CAS level, a PI controller is used for the ϕ control. Thus, the control input is

$$u_{CAS,lat} = K_\phi(\phi_{com} - \phi) + K_{i\phi} z_\phi. \tag{5.40}$$

The error can be defined as

$$\dot{z}_\phi = e_\phi = \phi_{com} - \phi. \tag{5.41}$$

By summing up the both SAS and CAS signals, the total lateral-directional control input becomes

$$u = u_{SAS,lat} + u_{CAS,lat} = \begin{bmatrix}\delta_{r_{pw_{com}}}\\ \delta_{a_{com}}\end{bmatrix} = \begin{bmatrix}K_{p_r}C_r x_{lat}\\ K_{p_p}C_p x_{lat} + K_\phi(\phi_{com} - C_\phi x_{lat}) + K_{i\phi} z\end{bmatrix}, \tag{5.42}$$

where

$$C_\phi = \begin{bmatrix}0 & 1 & 0 & 0\end{bmatrix}. \tag{5.43}$$

Please note that u_{CAS} changes only the $\delta_{a_{com}}$ as per its definition in Fig. 5.2. Then, the state matrix is expanded by adding the change in the error to the system of equations such that

$$\begin{bmatrix} \dot{x}_{lat} \\ \dot{x}_{a,lat} \\ \dot{z}_{\phi} \end{bmatrix} = \begin{bmatrix} A_{lat} & B_{lat} & 0 \\ B_{a,lat}\begin{bmatrix} K_{p_r}C_r \\ K_{p_p}C_p - K_{p_\phi}C_\phi \\ -C_\phi \end{bmatrix} & A_{a,lat} & B_{a,lat}\begin{bmatrix} 0 \\ K_{i\phi} \\ 0 \end{bmatrix} \end{bmatrix} \begin{bmatrix} x_{lat} \\ x_{a,lat} \\ z_{\phi} \end{bmatrix} + \begin{bmatrix} 0 \\ B_{a,lat}\begin{bmatrix} 0 \\ K_{\phi} \end{bmatrix} \\ 1 \end{bmatrix} \phi_{com} = A_{CAS,lat}\begin{bmatrix} x_{lat} \\ x_{a,lat} \\ z_{\phi} \end{bmatrix} + B_{CAS,lat}\phi_{com}. \tag{5.44}$$

After obtaining 5.44, for $Re(\lambda_l at) \leq 0$, the condition of $\max|Re(\lambda_l at)|$ of $A_{CAS,lat}$ is determined for the stability of the level flight model. In following, the K_ϕ) and $K_{i\phi}$ are selected by minimizing $J = \int e_\phi^2 dt$ in a similar fashion to longitudinal motion.

Heading Definition for Lateral - Directional Control. Due to the coupled dynamics of the system, the roll and yaw attitude angles are affected by any sideways maneuver simultaneously. Therefore, we need to define these maneuvers in a meaningful manner so that the vehicle can perform them. Otherwise, it may be physically impossible for the vehicle to follow the commanded lateral-directional trajectory. Therefore, we utilize a 2D trajectory generation strategy called "carrot-chasing" algorithm, which necessitates the definition of a heading angle to account for the coupling effect between the two motions. Hence, the heading control is defined as

$$\phi_{com} = K_\psi e_\psi = K_\psi(\psi_{com} - \psi), \tag{5.45}$$

where ψ_{com} is the reference for heading and generated by the carrot-chasing algorithm. Also, per definition,

$$\dot{\psi} = \frac{r}{\cos(\theta_{Trim})} = \frac{C_r x_{lat}}{\cos(\theta_{Trim})} \tag{5.46}$$

where θ_{Trim} is the trim pitching angle. Then, the augmented state matrix can be re-written as

$$\begin{bmatrix} \dot{x}_{lat} \\ \dot{x}_{a,lat} \\ \dot{z}_{\phi} \\ \dot{\psi} \end{bmatrix} = \begin{bmatrix} A_{lat} & B_{lat} & 0_{4\times 2} \\ B_{a,lat} \begin{bmatrix} K_{p_r} C_r \\ K_{p_p} C_p - K_{p_\phi} C_\phi \end{bmatrix} & A_{a,lat} & B_{a,lat_{4\times 2}} \begin{bmatrix} 0 & 0 \\ K_{i\phi} & K_\psi K_\phi \end{bmatrix}_{2\times 1} \\ -C_\phi & 0_{1\times 2} & K_\psi \end{bmatrix} \begin{bmatrix} x_{lat} \\ x_{a,lat} \\ z_{\phi} \\ \psi \end{bmatrix}$$
$$+ \begin{bmatrix} 0_{4\times 1} \\ B_{a,lat} \begin{bmatrix} 0 \\ K_\psi K_\phi \end{bmatrix} \\ K_\psi \\ 0 \end{bmatrix} \psi_{com} = A_\psi \begin{bmatrix} x_{lat} \\ x_{a,lat} \\ z_{\phi} \\ \psi \end{bmatrix} + B_\psi \psi_{com}. \tag{5.47}$$

5.2.3 Carrot-Chasing Algorithm for Lateral-Directional Guidance

Straight-Line Following. For a straight-line following problem, we first need to define the start and end point of that line W_i and W_{i+1}. After that, depending on the vertical minimum distance/the cross-track error (d) of UAV's current position p from the defined path,the algorithm generates a desired course angle ψ_d.The distance of the carrot point from the vertical projection q of UAV's current position p is δ. q, on the other hand, is away from W_i by R whereas p is at a distance of R_u. The current carrot position is $s = (x_t, y_t)$). In the next time-step, the UAV gets closer to the path as the PI controller pushes it to a heading angle closer to ψ_d and thus, the $s = (x_t, y_t)$) is

updated to the next position by $s = (x_t + \delta, y_t + \delta)$). This process continues until the UAV reaches the desired path. The lower δ is, the more carrot points are generated and the faster the UAV reaches to the path. Nevertheless, very frequent occurrence of δ causes oscillatory motions along the path, due to overshoots. Therefore, its value should be "sufficiently high" for a better trajectory tracking, which relies on a little trial-and-error. Fig. 5.3a is a representation of this algorithm.

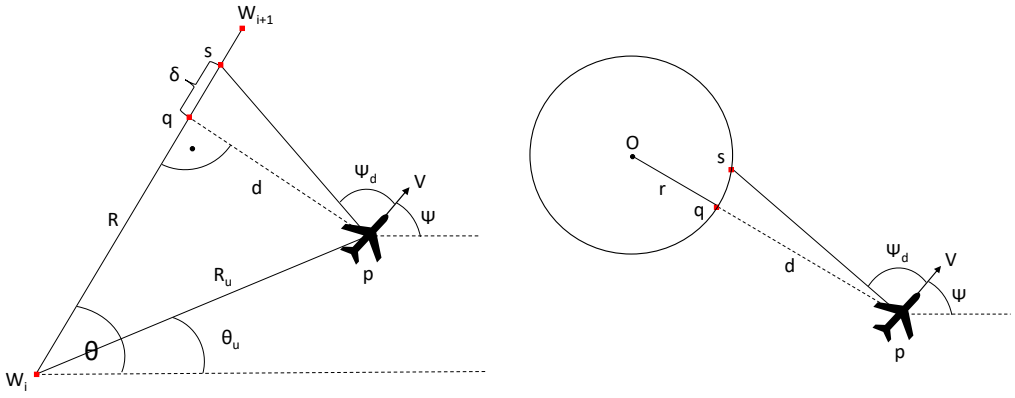

(a) Straight flight.

(b) Loiter flight.

Figure 5.3: Iterative logic of the carrot-chasing algorithm for (a) straigt level flight and (b) a circular loiter flight adapted from [123].

Loiter. The logic for a loiter maneuver is similar to the straight line tracking. However, in the loiter flight, a reference trajectory is generated with the center (O) and the radius of that path r, as shown in Fig. 5.3b.

Similar to straight line following, the carrot is again generated on the desired path but with another performance parameter λ. The cross-track error is calculated as $d = \|O - p\| - r$ so the heading angle ψ_d is obtained over an arc depending on the values of λ. The frequency of λ determines how fast the UAV will settle on the circle. When compared to δ in straight-line following, λ is a more relaxed parameter and it is more convenient to follow a circular trajectory for the UAV. The current carrot position

is again $s = (x_t, y_t)$). In the next time-step, the UAV gets closer to the path as the PI controller pushes it to a heading angle closer to ψ_d and thus, the $s = (x_t, y_t))$ is updated to the next position by $s = (rcos(\theta + \lambda), rsin(\theta + \lambda))$. This process continues until the UAV reaches the desired path.Nevertheless, very frequent occurrence of λ causes oscillatory motions along the circle, due to overshoots whereas a very high λ may not result in a converging result.

5.2.4 Learning Controller Design

The learning controller used in this work is a type-2 fuzzy neural network (T2FNN) based on [124], which is proven to be robust under time-varying conditions, unmodeled dynamics and disturbances. T2FNN is utilized to adjust the controller input provided by PD gains. To avoid any unstable conditions, PD gains are tuned roughly to bring the system to an –at least– marginally stable condition and the rest of the control action is taken by T2FNN. Figure 5.4 shows the functioning principle of T2FNN with PD controllers as implemented in this work. The error is fed both to PD and T2FNN. Depending on the update rules, T2FNN adjusts its output over time depending on the PD output so that both the error and the effects of disturbances are reduced. Accordingly, the final controller output of the learning controller is determined as

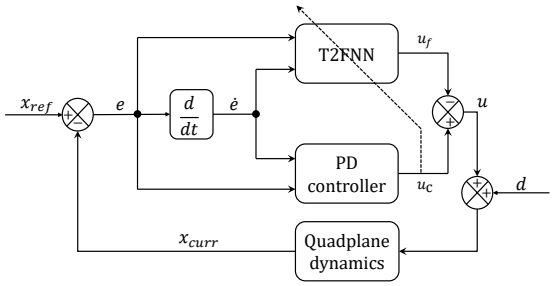

Figure 5.4: Proposed learning control block diagram along with disturbance d acting on the quadplane dynamics.

$$u = u_c - u_f, \tag{5.48}$$

where u_c and u_f stand for the inputs produced by the PD and T2FNN, respectively. In order to adjust the control output over time, T2FNN uses a rule base, of which ij$^{\text{th}}$ rule can be represented as [101]

$$IF\ x_1\ is\ \tilde{A}_{1i}\ and\ x_2\ is\ \tilde{A}_{2i},\ THEN\ u_f = f_{ij} i = 1, \ldots, I, j = 1, \ldots, J \tag{5.49}$$

where x_1 and x_2 are the input variables, I and J are the number of membership functions (MFs) for x_1 and x_2, respectively. f_{ij} are consequent parameters of the fuzzy system, and $\tilde{A}_{1i}$, $\tilde{A}_{2i}$ are the type-2 fuzzy sets for the inputs with their corresponding fuzzy MFs represented as $\tilde{\mu}_{1i}$, $\tilde{\mu}_{2j}$, respectively. Here, the inputs to T2FNN are error e and its derivative $\dot{e}$. The lower and upper MFs of $\tilde{\mu}_{1i}$ are $\underline{\mu}_{1i}$ and $\overline{\mu}_{1i}$. Similarly, the lower and upper MFs of $\tilde{\mu}_{2j}$ are $\underline{\mu}_{2j}$ and $\overline{\mu}_{2j}$, respectively. Thus, the firing levels can be computed as

$$\begin{aligned} \underline{W_{ij}} &= \underline{\mu}_{1i}(x_1)\underline{\mu}_{2j}(x_2) \\ \overline{W_{ij}} &= \overline{\mu}_{1i}(x_1)\overline{\mu}_{2j}(x_2) \end{aligned}. \tag{5.50}$$

Hence, the T2FNN control input becomes

$$u_f = \frac{1}{2}\frac{\sum_{j=1}^{J}\sum_{i=1}^{I}\underline{W_{ij}}f_{ij}}{\sum_{j=1}^{J}\sum_{i=1}^{I}\underline{W_{ij}}} + \frac{1}{2}\frac{\sum_{j=1}^{J}\sum_{i=1}^{I}\overline{W_{ij}}f_{ij}}{\sum_{j=1}^{J}\sum_{i=1}^{I}\overline{W_{ij}}}. \tag{5.51}$$

The selected T2 MFs are in the form of Gaussian distributions. As shown in [125], the Gaussian MFs can be represented as in (5.52)

$$\begin{aligned}
\underline{\mu}_{1i}(x_1) &= exp\left(-\left(\frac{x_1-\underline{c_{1i}}}{\underline{\sigma_{1i}}}\right)^2\right)\\
\overline{\mu}_{1i}(x_1) &= exp\left(-\left(\frac{x_1-\overline{c_{1i}}}{\overline{\sigma_{1i}}}\right)^2\right)\\
\underline{\mu}_{2j}(x_2) &= exp\left(-\left(\frac{x_2-\underline{c_{2j}}}{\underline{\sigma_{2j}}}\right)^2\right)\\
\overline{\mu}_{2j}(x_2) &= exp\left(-\left(\frac{x_2-\overline{c_{2j}}}{\overline{\sigma_{2j}}}\right)^2\right)
\end{aligned}, \tag{5.52}$$

where c and σ are the centers and standard deviations from the centers of MFs, respectively. Then, the firing rules in (5.50) can be rewritten as

$$\begin{aligned}
\underline{W_{ij}} &= exp\left(-\left(\frac{x_1-\underline{c_{1i}}}{\underline{\sigma_{1i}}}\right)^2-\left(\frac{x_2-\underline{c_{2j}}}{\underline{\sigma_{2j}}}\right)^2\right)\\
\overline{W_{ij}} &= exp\left(-\left(\frac{x_1-\overline{c_{1i}}}{\overline{\sigma_{1i}}}\right)^2-\left(\frac{x_2-\overline{c_{2j}}}{\overline{\sigma_{2j}}}\right)^2\right)
\end{aligned}. \tag{5.53}$$

The PD controller which shows the global asymptotic stability in the closed loop, helps to obtain [101]

$$\begin{aligned}
|e(t)| &\leq B_e\\
|\dot{e}(t)| &\leq B_{\dot{e}} \quad \forall t,\\
|\ddot{e}(t)| &\leq B_{\ddot{e}}
\end{aligned} \tag{5.54}$$

where $B_e > 0, B_{\dot{e}} > 0$ and $B_{\ddot{e}} > 0$ are assumed to be some constant values. The adaptation laws for the parameters of the MFs, σ and c values, are also kept constant.

In other words, they are also bounded as

$$\begin{aligned} \underline{B_\sigma} \leq ||\underline{\sigma_1}|| \leq \overline{B_\sigma}, \quad \underline{B_\sigma} \leq ||\underline{\sigma_2}|| \leq \overline{B_\sigma}, \\ \underline{B_\sigma} \leq ||\overline{\sigma_1}|| \leq \overline{B_\sigma}, \quad \underline{B_\sigma} \leq ||\overline{\sigma_2}|| \leq \overline{B_\sigma}, \\ ||\overline{c_1}|| \leq B_c, \qquad ||\overline{c_2}|| \leq B_c, \\ ||\underline{c_1}|| \leq B_c, \qquad ||\underline{c_2}|| \leq B_c, \end{aligned} \tag{5.55}$$

In addition, it is also assumed that the time-varying parameters of the consequent part are also bounded; that is,

$$|f_{ij}| \leq B_{ij} \quad \forall t. \tag{5.56}$$

Following the constraints from (5.54) to (5.56), it is evident that

$$|u(t)| \leq B_u, \quad |\dot{u}(t)| \leq B_{\dot{u}} \quad \forall t, \tag{5.57}$$

where $B_u > 0$ and $B_{\dot{u}} > 0$ are some constant values.

In order for the learning controller to adjust the final control output, T2FNN parameters are updated using a sliding mode control (SMC) based technique. SMC, by its nature, produces a chattering output for the controller; however, T2FNN can manage to reduce this chattering behavior [126]. Mathematical derivation of this technique is presented in [101]. Accordingly, the consequent and learning rate parameters are updated as follows

$$\dot{f_{ij}} = -\alpha \frac{0.5\underline{\widetilde{W_{ij}}} + 0.5\overline{\widetilde{W_{ij}}}}{(0.5\underline{\widetilde{W}} + 0.5\overline{\widetilde{W}})^T (0.5\underline{\widetilde{W}} + 0.5\overline{\widetilde{W}})} sgn(u_c), \tag{5.58}$$

$$\dot{\alpha} = \gamma_1 \mid u_c \mid -\nu\gamma_1\alpha, \tag{5.59}$$

where α is the learning rate. $\underline{\widetilde{W_{ij}}}$ and $\overline{\widetilde{W_{ij}}}$ are the normalized lower and upper outputs of the ij$^{\text{th}}$ rule of the fuzzy system while $\underline{\widetilde{W}}$ and $\overline{\widetilde{W}}$ stand for the vectors of the normalized outputs.

5.3 Results

5.3.1 Forward Flight Simulations and Discussions

In the earlier sections, the methodologies for both the linear controller and T2FNN development are presented. In this section, several longitudinal and lateral-directional routes are defined for the system and its tracking responses are recorded. The main purpose of this simulation study is to discuss the efficiency of the T2FNN in uncertain or varying conditions.

Case study I. In the first scenario, we discuss a trajectory tracking problem with the linear conventional controllers and T2FNN+PD at a fixed altitude of 10m as seen in Fig. 5.5a to test the controllers under nominal conditions. The vehicle is able to follow the fixed references of 10 m easily. Slightly higher error with the learning controller is due to the progress of learning as seen in Fig. 5.5b, until the learning rate reaches to a meaningful value. In the same figure, it is also evident that the slope of the learning rate decays once the system settles to the given trajectory. However, in order to avoid the over-learning/over-fitting, an upper limit for the learning-rate could also be defined.

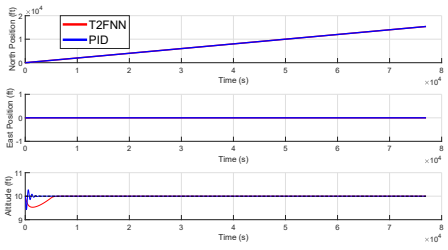

(a) Position control with conventional and T2FNN+PD controllers at 10 m altitude.

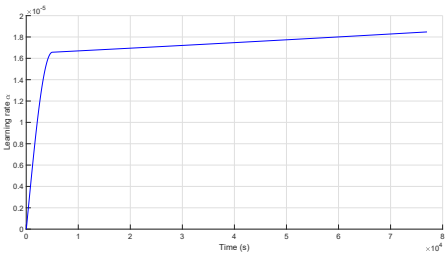

(b) Learning rate of the T2FNN.

Figure 5.5: Case I.

Case study II. In the second scenario, we use the same trajectory tracking problem at a fixed altitude of 10m but with a wind disturbance acting on the system (See Fig. 5.6). This scenario is created to test the learning ability of the intelligent controller when disturbances are present. In this condition, the vehicle with the linear controllers performs better at the beginning of simulation. However, throughout the simulation, T2FNN learns the effect of the wind on the system such that the altitude deviations are damped out slowly. When the system reaches to the end of simulation, it is evident that there is a difference between the linear and learning controllers. The learning rate asymptotically approaches to a higher value when compared to the earlier case study. It shows an oscillatory behavior, of which amplitude reduces over time.

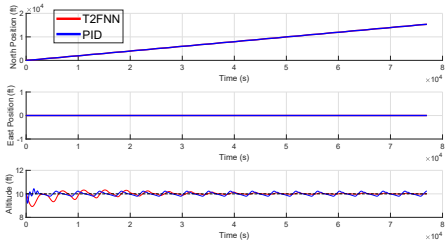

(a) Position control with conventional and T2FNN+PD controllers at 10 m altitude with sinusoidal wind of a maximum amplitude of 5 m/s.

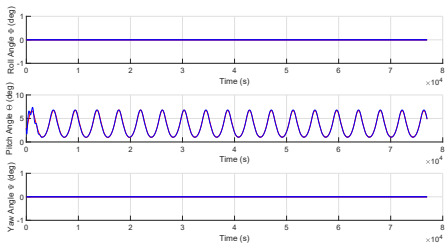

(b) Attitude changes with conventional and T2FNN+PD controllers with sinusoidal wind of a maximum amplitude of 5 m/s.

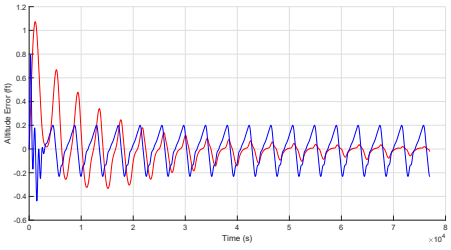

(c) Altitude error with conventional and T2FNN+PD controllers in the windy condition.

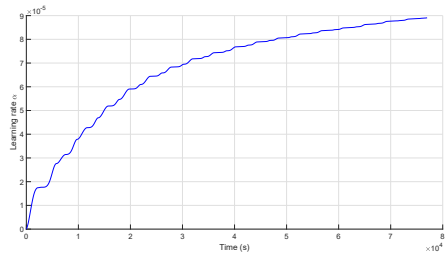

(d) Learning rate of the T2FNN in the windy condition.

Figure 5.6: Case II.

Case study III. The third scenario is actually a combination of a varying altitude reference under a windy condition. The target of this study is to observe the behavior of T2FNN+PD algorithm when the altitude reference also changes. Results are as expected and in conformity with the previous case. However, the effect of the varying reference is less significant when compared to the directly added disturbance (see Fig. 5.7). Once the system learns the flight condition, it is able to track it. The learning behavior is quite similar to study II as well.

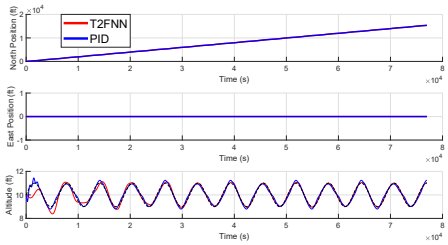

(a) Position control with conventional and T2FNN+PD controllers at 10 m altitude.

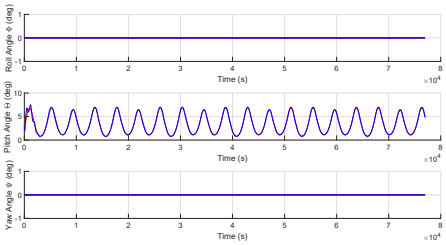

(b) Attitude changes with conventional and T2FNN+PD controllers at 10 m altitude.

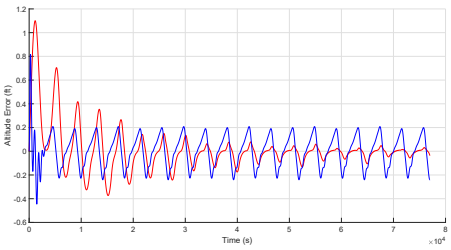

(c) Altitude error with conventional and T2FNN+PD controllers.

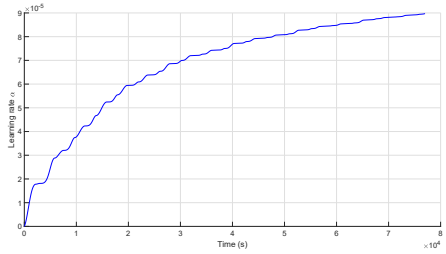

(d) Learning rate of the T2FNN.

Figure 5.7: Case III.

Case study IV. The final scenario presented here is a bit different than the previous three cases. The idea of this scenario is to test whether the designed linear controllers are able to capture the 3D dynamics of the UAV. In this context, two different trajectories, namely a square-like path and a circle path for loiter flight are generated as seen in Fig 5.8. The results indicate that the nature of carrot-chasing algorithm causes the so-called carrots to be generated in a oscillatory manner, forcing the system to

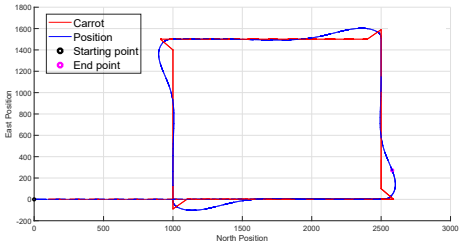

(a) Square trajectory tracking at 10 m fixed altitude reference using the carrot chasing algorithm.

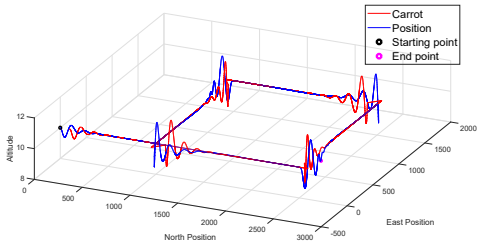

(b) Square trajectory tracking at 10 m fixed altitude reference using the carrot chasing algorithm.

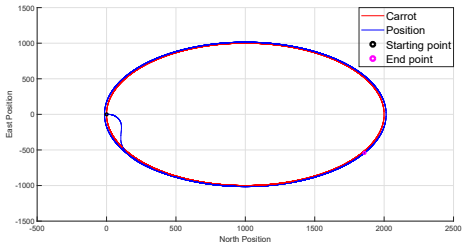

(c) Circular trajectory tracking at 10 m fixed altitude reference using the carrot chasing algorithm.

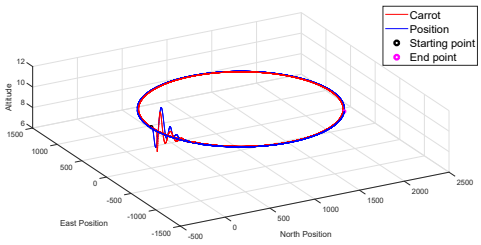

(d) Circular trajectory tracking at 10 m fixed altitude reference using the carrot chasing algorithm.

Figure 5.8: CaseIV.

oscillate at the beginnings of both trajectories and in the cases where rapid maneuvers are present, such as at the corners of square-like trajectory.

5.3.2 Fuzzy Switching Logic between Models

As explained in Chapter 4, a portion of the wing is under the effect of the propeller wake and thrust force, which causes a high angle of attack flow on it. Consequently, the aerodynamic characteristic of the UAV for the low tilting angles are significantly different from the high tilting angles. Therefore, the trim states obtained over the course of tilting show distinctive features. It is also worth noting that the controller gains are calculated via linear interpolations between each trim point. This results in the fact that the switches between two consecutive models take different durations until the UAV is stabilized. Therefore, a nonlinear tilting function accounting for this effect

is necessary. The idea in this thesis is to generate this nonlinear function using a fuzzy logic-based switching algorithm and to reduce the deviations from the calculated trim conditions.

The switching algorithm is designed as a function of the tilting angle. As reflected in Fig. 5.9c, each trim point has a corresponding trim speed. Therefore, three Gaussian membership functions (MFs) representing the partial membership of the tilting angle i_t to a set of low μ_1, average μ_2 and high μ_3 angles are defined as shown in Fig. 5.9a. Here, the centers and the width of the MFs are $[c_1, c_2, c_3] = [0, 45, 90]$ and $[\sigma_1, \sigma_2, \sigma_3] = [30, 20, 30]$, respectively. Using a Sugeno type fuzzification, the i$^{\text{th}}$ fuzzy rule can be written as [101]

$$IF\ i_t\ is\ \tilde{A}_i;\ THEN\ di_t/dt = k_i,\ i = 1; \ldots, I, \tag{5.60}$$

where I is the number of MFs. The tilting rate di_t/dt is the output variable, k_i is the consequent part of the fuzzy system, and $\tilde{A}_i$ is a type-1 fuzzy set. Then, the corresponding tilting rate is calculated by (5.61). The resulting distribution is given in Fig. 5.9b.

$$\frac{di_t}{dt} = \frac{\sum_{i=1}^{I} \mu_i k_i}{\sum_{i=1}^{I} \mu_i}. \tag{5.61}$$

5.3.3 Tilt-Rotor Simulations and Discussions

In this section, the simulation results of the fixed and fuzzy switching rates are presented. For the tilting motion, the switching duration between the models is very critical. The UAV is able to balance the loads at each model defined in 10° intervals. Each model is represented by a model number as in Fig. 5.10a. The highest model number, 9, represents the near hover condition whereas the model number 0 corresponds to the steady level flight condition. Furthermore, one should also note that it takes an average of 30s to balance the UAV at each model as shown in Fig. 5.10b. The reason

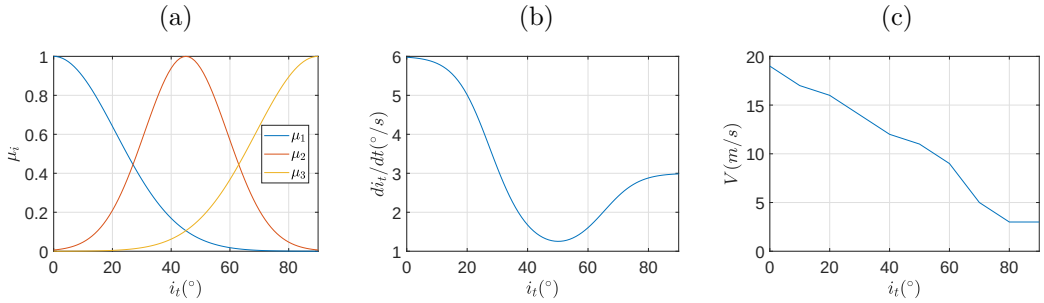

Figure 5.9: Selected membership functions for the tilt angle (a) and its corresponding tilting output (b). The MFs are used to generate the tilting rate di_t/dt with respect to the instantaneous tilting angle i_t. The MF selection is carried out considering the relationship between the tilt angle and speed interpolations (c).

of balancing the loads at each trim point is to show the stability of the UAV at each trim point. By this manner, it is proven that the UAV would be able to maneuver at each trim point and we would have control at every tilting angle. During the tilting period, the altitude reference of the UAV is kept the same at 10m as highlighted in Fig. 5.10d. The corresponding reference pitch angle θ_{ref} is also shown in Fig. 5.10e. From these graphs, it is noticed that the oscillations at the altitude and pitch angle depend strictly on the magnitude of tilting rate. When the tilting rate is kept low throughout the transition, then the magnitudes of the oscillations can be reduced significantly. However, this results in a much longer duration for tilting of the rotors. Therefore, in order to keep the tilting duration at a practical level, the fixed tilting rate di_t/dt is selected as 3°/s. Hence, by decreasing the tilting rate where the oscillations are adverse, we can obtain a better performance. For this purpose, the fuzzy algorithm described in the previous section is employed. All Fig. 5.10 results compare the performances of the fixed and fuzzy tilting rates. As shown in Figs. 5.10d, 5.10e and 5.10f, for the switches between 6^{th} and 4^{th} models, 3°/s tilting rate is too high and causes an oscillatory response. This is the region where the aerodynamic forces start getting more prominent and the UAV transients from the multi-rotor dominant dynamics to

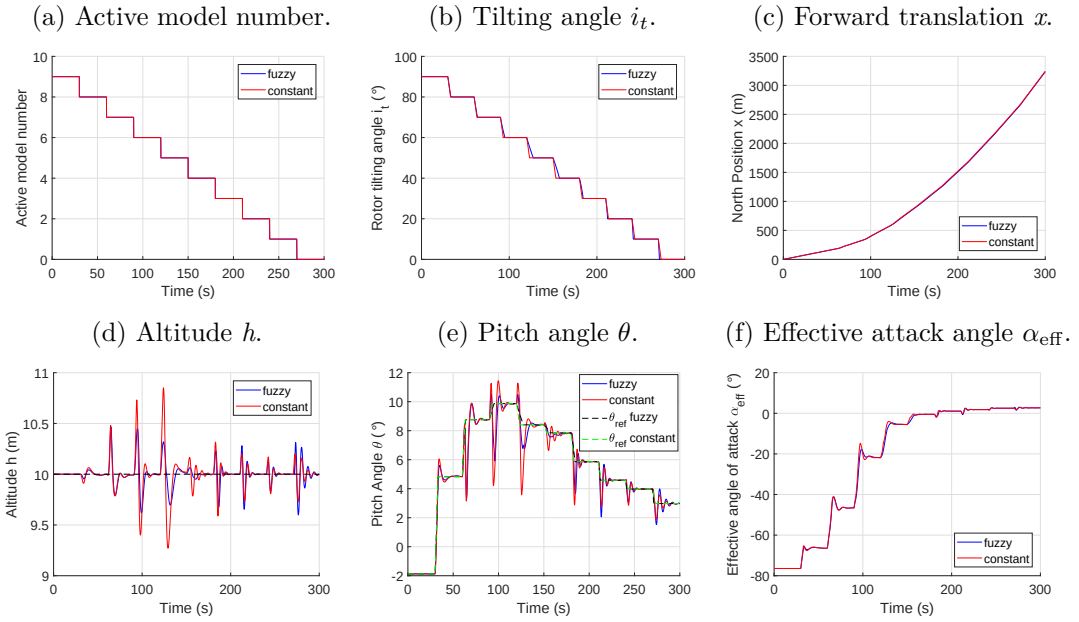

Figure 5.10: Comparison of the cases of the fixed tilt rate $di_t/dt = 3$ř and the fuzzy logic based tilting for an intermittent tilting case. (a) highlights the initial tilting position of the UAV whereas (b) shows the change in the tilt angle i_t. The forward translation (c), altitude (d), and the desired pitch angle tracking (e) are also compared for the fuzzy and constant tilting cases. The corresponding efficient angle of attack changes are reflected in (f).

a more fixed-wing dominant dynamics. Therefore, it is very sensitive to the tilting rate in this range, and a slower tilting is preferred as dictated by the fuzzy switching algorithm. The further tilting angles are not susceptible to the tilting rate as much as in this region. Thus, the tilting rate is increased even higher than 3°/s for further tilting angles of which results are presented in Table 5.3. It is evident that the maximum error in altitude and pitch angle tracking is decreased by 45.2% and 5.5%, respectively. Besides, the mean absolute error (MAE) and the root mean squared error (RMSE) are reduced by 24.4% and 31.3% for the altitude and 20.3% and 23.7% for the pitch angle, respectively.

Continuous tilting. After checking the behavior of the fuzzy switching algorithm in intermittent tilting, the continuous tilting case is investigated. As shown in Fig. 5.11a, in this case, the time spent between each model is varying for the fuzzy switching algorithm. The resulting rotor tilting behavior is shown in Fig. 5.11b, where both fuzzy and constant tilting strategies take the same total duration but in different regimes. The distance covered during the transition is shown in Fig. 5.11c, where fuzzy algorithm takes 41 m less than the constant tilting rate case. The differences of oscillations in the altitude can be seen in Fig. 5.11d and the pitch angle tracking is highlighted in Fig. 5.11e. Although the fuzzy switching algorithm outperforms the constant switching algorithm, the performance of the pitch angle tracking is significantly reduced in the continuous tilting when compared to the intermittent tilting. Finally, the change of α_{eff} is given in Fig. 5.11f. The control performance in the continuous tilting case is presented in Table 5.4.

3D trajectories. After the completion of the tilting motion, a complete circular trajectory tracking result is presented for the sake of completeness of the 6DOF maneuver. Figures 5.12a and 5.12b showcase the intermittent tilting and the continuous tilting cases, respectively. The initial oscillations are caused by tilting of the rotors. The last group of oscillations is due to the start of the loiter flight. Since the rolling and yawing motions are controlled only with the differential thrust and aileron inputs,

Table 5.3: Comparison of results for maximum error (MAX), mean absolute error (MAE), and root mean squared error (RMSE) of h and θ for the whole transition flight in intermittent tilting case.

Tilting type	MAX		MAE		RMSE	
	h (m)	θ (°)	h (m)	θ (°)	h (m)	θ (°)
Fixed rate switching	0.8511	5.6510	0.0726	0.3797	0.1590	0.9277
Fuzzy rate switching	0.4663	5.3970	0.0549	0.3027	0.1092	0.7080
Difference (%)	45.2	4.5	24.4	20.3	31.3	23.7

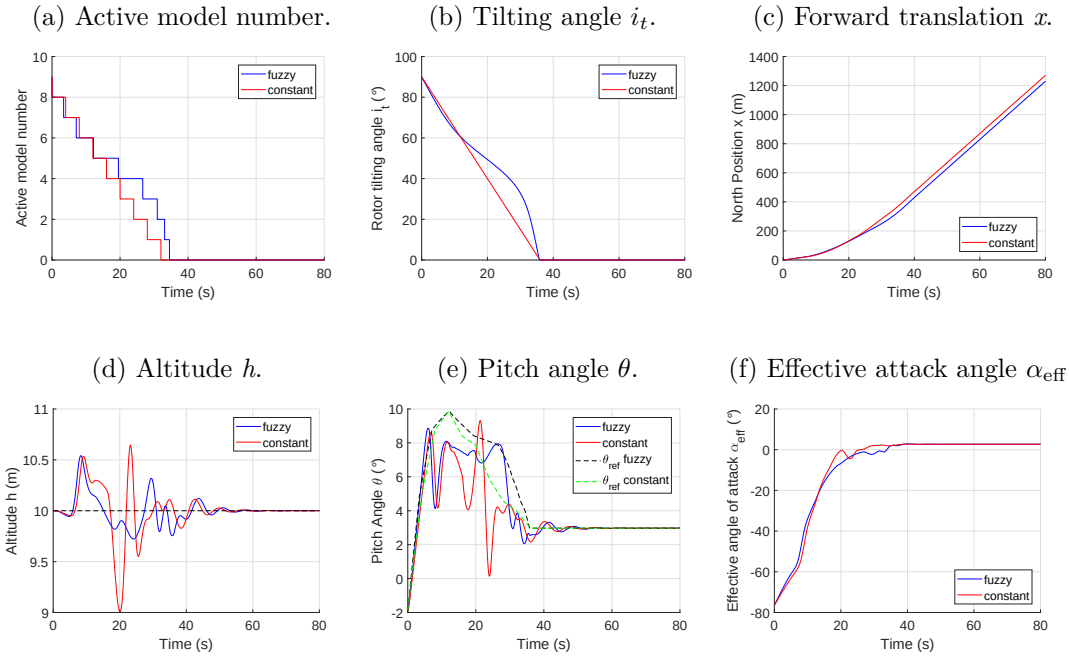

Figure 5.11: Comparison of the cases of the fixed tilt rate $di_t/dt = 2.5$ř and the fuzzy logic based tilting for a continuous tilting case. (a) highlights the initial tilting position of the UAV whereas (b) shows the change in the tilt angle i_t. The forward translation (c), altitude (d) and the desired pitch angle tracking (e) are also compared for the fuzzy and constant tilting cases. The corresponding efficient angle of attack changes are reflected in (f).

there are naturally some oscillations. As the carrot-chasing algorithm does not have any control on the altitude, the reference lines are also oscillating at the beginning of the circular motion. However, with oscillations in altitude dying out due to the longitudinal flight controller, the carrot-chasing algorithm starts generating horizontal references and UAV tracks down the reference successfully.

5.4 Summary

In this chapter, a multi-model flight control of a tilt-rotor blended wing-body UAV with a fuzzy switching algorithm is presented. First, the 6DOF nonlinear model of the UAV is linearized at ten different trim states which represent the flight conditions at ten different tilt angles of the rotors. Then, conventional PID controllers are designed

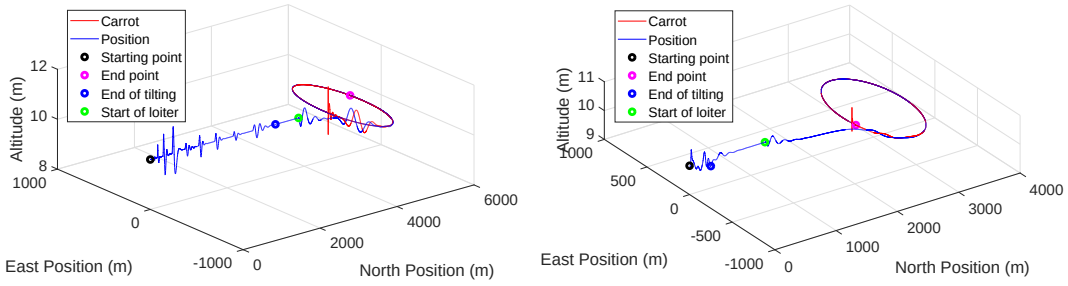

(a) Intermittent tilting and loiter.

(b) Continuous tilting and loiter.

Figure 5.12: Complete tilting followed by a loiter flight. The UAV starts its motion at the hover condition. In (a) the rotors are tilted 10° every 30s intermittently whereas in (b), they are tilted continuously in the first 36 s. The initial picks in the reference lines highlighted in red are caused by the coupled rolling-yawing motion when starting the loiter flight.

by minimizing a cost function based on the attitude or position tracking error. For the angles in-between the trim models, linear interpolations are carried out to calculate the controller gains. As the controller inputs, the differential thrust and control surface inputs are considered simultaneously. The rotors are first tilted at 3° fixed tilting rate and then with a varying tilting rate defined by the fuzzy algorithm. The results indicate that, for the intermittent tilting case, the fuzzy algorithm helps to reduce the RMSE of the oscillations by 31.3% and 41.4% for the altitude and 23.7% and 20.7% for the pitch angle tracking, respectively. The main benefit of the fuzzy algorithm is the fact that the tilting rate is reduced where the oscillations are significant. In the end, a case

Table 5.4: Comparison of results for maximum error (MAX), mean absolute error (MAE), and root mean squared error (RMSE) of h and θ for the whole transition flight in continuous tilting case.

Tilting type	MAX		MAE		RMSE	
	h (m)	θ (°)	h (m)	θ (°)	h (m)	θ (°)
Fixed rate switching	0.9940	5.7360	0.0955	0.6016	0.2069	1.2934
Fuzzy rate switching	0.5409	4.8832	0.0653	0.5271	0.1212	1.0256
Difference (%)	45.6	14.9	31.6	12.4	41.4	20.7

study of a full transition from hover to forward and then to a loiter flight is presented. It is evident from the results that the UAV is capable of maneuvering on the given trajectory successfully. As a future study, the linear interpolations between the models will also be fuzzified for a better trajectory tracking performance.

Chapter 6

Unsteady Quadplane

6.1 Introduction

A nonlinear unsteady aerodynamics model is coupled with a three degree of freedom quadplane to control the forward and backward transition between hover and steady level flight. The unsteady lift and drag forces are modeled using a lumped vortex model for flat plates. Two variants for the quadplane are considered: (i) a pusher and (ii) a tilt-rotor configuration in the absence of control surfaces to assess the controllability for altitude, attitude and forward speed.

One of the advantages of including the unsteady aerodynamic forces is the simplification of the controller design process. As the forces rapidly change from zero at hover state to steady trim values at forward flight, it is not possible to use a linearized aerodynamic model for the simulation of the vehicle dynamics. In previous work [7, 11, 78, 127], multiple mathematical models representing different aerodynamic characteristics during a transition flight are generated to resolve this issue. In this context, this work can be considered unique since a fully nonlinear aerodynamic model is used to predict the transition effects [14, 128]. The unsteady aerodynamic model is implemented into nonlinear equations of motion for two vehicle variants, a quadplane

with a pusher rotor and a tilt-rotor quadplane. Thus, the differences in controllability of the given quadplane variants are further illustrated.

A learning controller consisting of a type-2 fuzzy neural network and a proportional-derivative controller is tested on the hover-to-level transition flights of both configurations under varying wind disturbances, and its performance is compared with a conventional proportional-integral-derivative (PID) controller. After showing that the learning controller outperforms the PID controller during the transition flight, which is the most unstable regime of VTOL UAVs, it is implemented for the whole flight envelope. The learning controller successfully completes missions consisting of vertical take-off, forward transition, level flight, backward transition and landing for both configurations. Independent of the flight phase and configuration, the controller structure remains the same.

6.2 Full Flight Envelope Control

The design parameters of the tilt-rotor and pusher configurations are listed in Table 6.1. The geometrical information as well as forces and moments acting on each configuration are illustrated in Figs. 6.1a, 6.1b and 6.1c, respectively.

Table 6.1: Common system specifications and design parameters for both configurations adapted from [8].

Specification	Value	Specification	Value
Airfoil type	NACA0012	Mean aerodynamic chord $\bar{c}$	0.083 m
Take-off weight	1 kg	Front rotor incidence angles	4°
Front and back wingspans b	0.5 m	Back rotor incidence angles	5°
Back rotor moment arms x_b	0.08 m	Inertia along pitching axis I_{yy}	0.006 kgm^2
Front rotor moment arms x_f	0.08 m	Level flight trim speed u	20 m/s
Back rotor vertical offset z_b	0.1 m	Level flight trim pitch angle θ	0°
Front rotor vertical offset z_f	0.0 m		

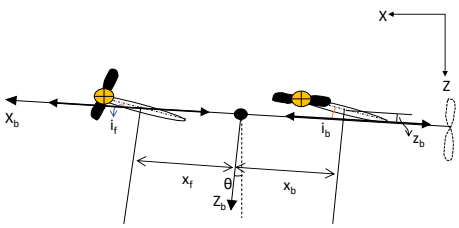

(a) Geometrical information.

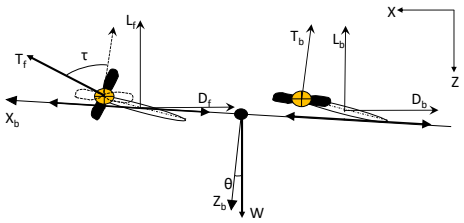

(b) Aerodynamic and thrust forces on the tilt-rotor quadplane.

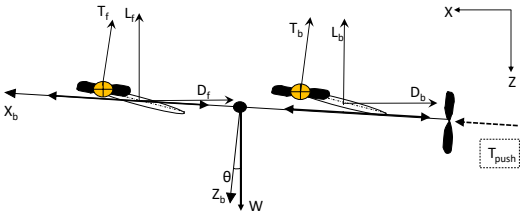

(c) Aerodynamic and thrust forces on the pusher quadplane.

Figure 6.1: Geometrical information (a), and free body diagrams of tilt-rotor (b) and pusher (c) configurations.

6.2.1 Ground-to-hover/hover-to-ground flight control

To complete a flight trajectory, three distinct flight modes are considered. The first mode is ground-to-hover (hover-to-ground), in which the vehicle operates in a similar fashion to a multi-rotor. In this mode of flight, aerodynamic forces acting on the vehicle can be considered to be negligible. Similar to a multi-rotor controller structure, it consists of two cascaded control loops, where the position control is obtained by the

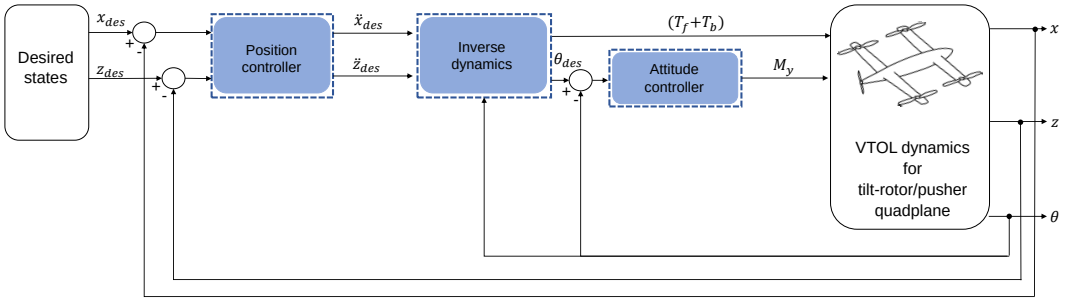

Figure 6.2: VTOL flight control scheme for both configurations. Aerodynamic forces are assumed to be insignificant for the take-off and landing conditions.

outer loop and the attitude control is achieved by the inner loop as shown in Fig. 6.2. The vehicle dynamics is governed by [103]

$$m\ddot{x} = -(T_f + T_b)\sin\theta, \tag{6.1}$$

$$m\ddot{z} = -(T_f + T_b)\cos\theta + mg, \tag{6.2}$$

$$I_{yy}\ddot{\theta} = M_y, \tag{6.3}$$

where x, z show the position of the vehicle in the inertial frame, M_y is the moment around the center of gravity defined by $M_y = T_f x_f - T_b x_b$, and the moment of inertia is denoted by I_{yy}. In order to calculate T_f and T_b, the inverse dynamic relationship between the desired acceleration terms $\ddot{x}_{des}$ and $\ddot{z}_{des}$ and the forces T_f and T_b and pitch angle θ can be written as

$$(T_f + T_b) = m(\ddot{z}_{des} - g)/cos(\theta), \tag{6.4}$$

$$\theta_{des} = \arctan\left(\ddot{x}_{des}/(\ddot{z}_{des} - g)\right). \tag{6.5}$$

Using (6.3), (6.4), and (6.5), T_f and T_b can be obtained.

6.2.2 Pusher rotor configuration control

For longitudinal motion, controllers for the state variables u, θ and z are implemented. Each of these states are controlled independently using a PID controller. The block diagram of this control scheme for both transition types is shown in Fig. 6.3 with the reference values of the desired states u_{des}, θ_{des} and z_{des}. Here, it should be noted that, for a more realistic representation of the actuator dynamics, a delay term is added for the pusher rotor thrust reversal occurring during the backward transition flight. For the pusher rotor dynamic model, there are three inputs corresponding to three controlled variables. The output of the throttle controller is the forward thrust

T_p. For the altitude and attitude control, the outputs δk_1 and δk_2 shown in (6.7) and (6.8) are required, which can be obtained from (4.1), (4.30), and (4.31) as

$$\begin{bmatrix} \dot{u} \\ \dot{w} \\ \dot{q} \end{bmatrix} = \begin{bmatrix} -g\sin\theta - qw + F_{A_X}/m \\ qu + F_{A_Z}/m \\ M_A/I_{yy} \end{bmatrix} + \begin{bmatrix} 1/m \\ 1/m \\ 1/I_{yy} \end{bmatrix} \begin{bmatrix} T_p \\ \delta k_1 \\ \delta k_2 \end{bmatrix}, \tag{6.6}$$

where

$$\delta k_1 = -T_f - T_b + mg\cos\theta \tag{6.7}$$

$$\delta k_2 = T_f x_f - T_b x_b \tag{6.8}$$

These two terms are used for the control of the front rotor thrust T_f and back rotor thrust T_b, respectively. For the backward transition, since the pusher rotor reduces from the steady level flight thrust T_{ss}, the speed controller input is modified as

$$\delta_T = T_p - T_{ss}. \tag{6.9}$$

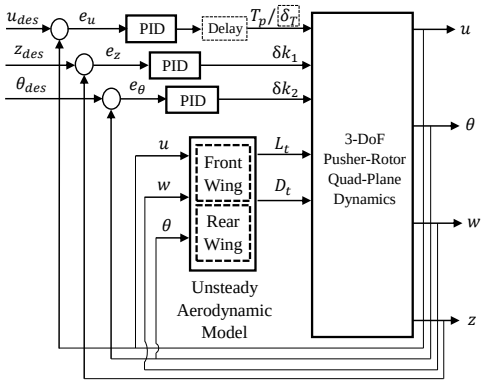

Figure 6.3: Pusher configuration quadplane block diagram for forward and backward transition.

6.2.3 Tilt-rotor configuration control

The tilt-rotor configuration has two front rotors tilting from the vertical position to the horizontal position with a defined tilt rate function. It should be noted that the pusher configuration has one more control input to accomplish a successful transition flight due to the additional pusher rotor, which ensures full attitude and altitude control. However, for the tilt-rotor configuration, the forward and backward transitions are accomplished by controlling different state parameters. The reason of this difference is the different requirements of forward and backward transitions. For transitioning from hover to level flight, it should be guaranteed that the vehicle reaches the trim condition such that sufficient lift is generated for level flight. The aircraft should be kept level during transition to avoid an adverse pitching motion, which may result in aircraft stall. Since there are only two control inputs, the altitude change is accepted and the aircraft is kept level by controlling θ and u as shown in Fig. 6.4a. On the other hand, when transitioning backwards, the final forward flight speed approaches zero as the vehicle approaches the hover condition. However, it should also be ensured that the vehicle maintains altitude during this transition process. Therefore, for the backward transition of tilt-rotor configuration, z and θ are the controlled state parameters (see Fig. 6.4b). Since the rotors are tilted to the vertical position during the backward transition phase, the forward flight speed u naturally reduces to zero due to aerodynamic drag and reduction of thrust force. To control θ for the forward transition, (4.1), (4.30), and (4.32) are used to derive the term δ which represents the change of the vertical forces as given in (6.11). Besides, the front rotor thrust T_f is directly employed to control the forward velocity u. For the backward transition flight, δ_T is derived considering the

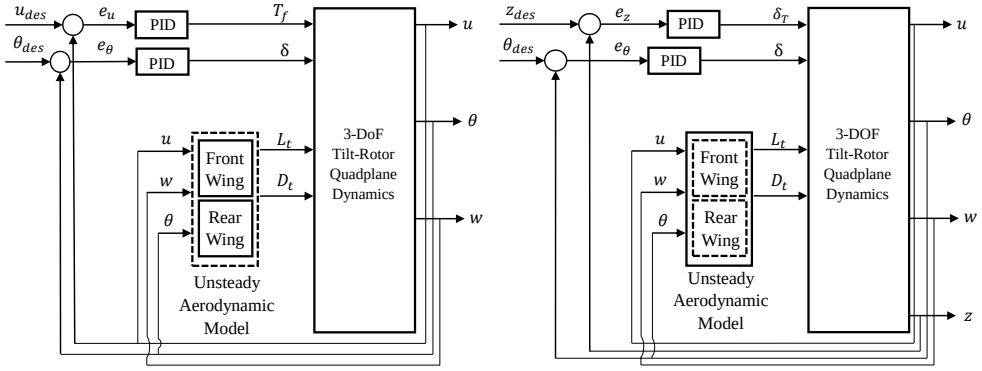

(a) Forward transition. (b) Backward transition.

Figure 6.4: Tilt-rotor quadplane block diagram for forward transition and backward transition flights.

steady level flight thrust of the front rotors T_{ss} as in (6.14).

$$\begin{bmatrix} \dot{u} \\ \dot{w} \\ \dot{q} \end{bmatrix} = \begin{bmatrix} -g\sin\theta - qw + F_{A_X}/m \\ qu + F_{A_Z}/m \\ M_A/I_{yy} \end{bmatrix} + \begin{bmatrix} 1/m \\ 1/m \\ 1/I_{yy} \end{bmatrix} \begin{bmatrix} T_f \sin\tau \\ \delta \\ T_f(x_f\cos\tau - z_f\sin\tau) - T_b x_b \end{bmatrix}, \tag{6.10}$$

where

$$\delta = -T_b - T_f\cos\tau + mg\cos\theta. \tag{6.11}$$

$$\delta_T = T_f - T_{ss}. \tag{6.12}$$

6.3 Results

6.3.1 Transition Flight Simulation Results

In this section, simulation results obtained with the unsteady aerodynamic model are presented. First of all, as discussed in the earlier subsection, it should be noted that the pusher configuration has an extra control input, which guarantees the altitude,

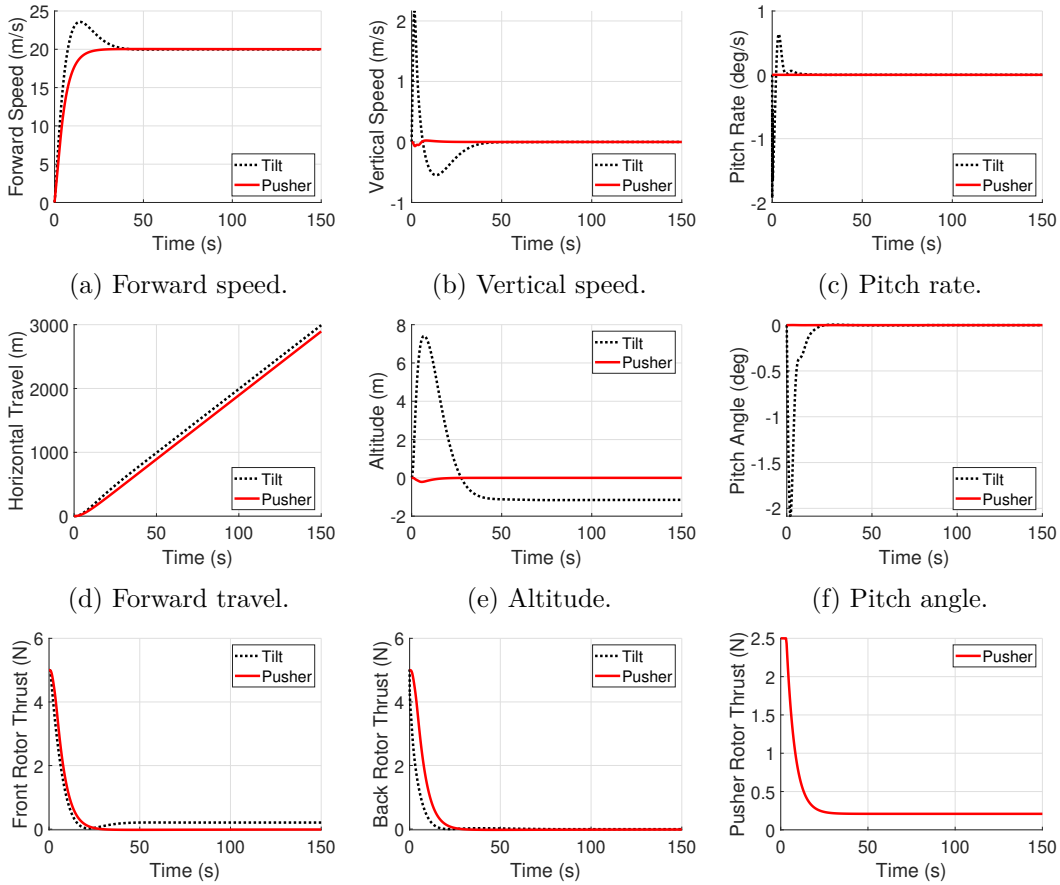

(a) Forward speed. (b) Vertical speed. (c) Pitch rate.

(d) Forward travel. (e) Altitude. (f) Pitch angle.

(g) Front rotor thrust. (h) Back rotor thrust. (i) Pusher rotor thrust.

Figure 6.5: Comparison of forward flight transition parameters of tilting and pusher configurations.

attitude and velocity control; whereas for the tilt-rotor configuration, the forward and backward transitions are accomplished by controlling different state parameters. For the tilt-rotor configuration, the altitude change is accepted as shown in 6.5e and the aircraft is kept level by controlling θ and u. On the other hand, when transitioning backwards, z and θ are controlled and the final altitude is kept constant as in Fig. 6.6e. Other consequences of following this strategy are reflected in Figs. 6.5 and 6.6 and are discussed next.

Figure 6.5a shows the change of u over time. It can be seen that, for both configura-

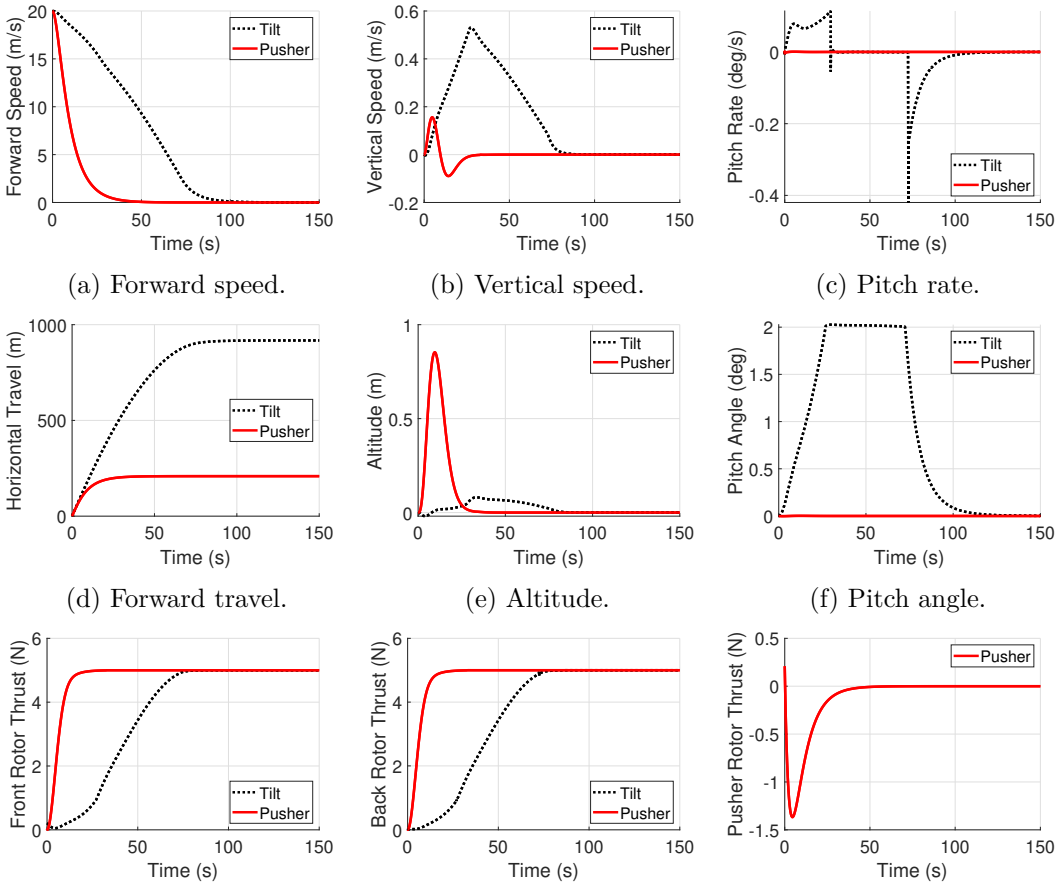

(a) Forward speed. (b) Vertical speed. (c) Pitch rate.

(d) Forward travel. (e) Altitude. (f) Pitch angle.

(g) Front rotor thrust. (h) Back rotor thrust. (i) Pusher rotor thrust.

Figure 6.6: Comparison of backward flight transition parameters of tilting and pusher configurations.

tions, the trim speed is achieved within 50 s. This graph should be evaluated with Fig. 6.5b, where the change of w is shown. For the tilt-rotor configuration, the vehicle -as expected - plunges due to the initiation of the tilt mechanism. This is due to the lack of z control in the tilting case. The overshoot of u in Fig. 6.5a is coupled with the rise and later drop in w as the UAV tries to approach the trim speed. Since the trim speed is accurately selected, w reaches zero in both configurations. To take a closer look at the significance of trim speed sensitivity, Figs. 6.7a - 6.7d should be observed. As can be seen from these figures, the forces and moments in the tilt-rotor configuration can

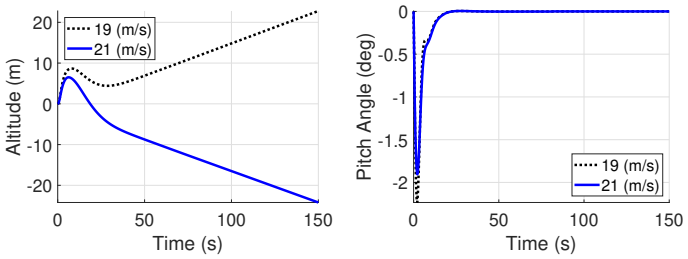

(a) Altitude. (b) Pitch angle.

(c) Forward speed. (d) Vertical speed.

Figure 6.7: Unbalanced altitude change and vertical speed during forward flight transition with inaccurate trim settings (19 and 21 m/s) for the tilt-rotor configuration. This data shows that its flight speed should always be considered along with the tilting function.

be balanced at speeds other than the trim speed. However, the vehicle continuously plunges or rises. In other words, the force and moments can be balanced without trimming the tilt-rotor aircraft at a constant altitude. This phenomenon does not arise in the pusher configuration since the altitude is also controlled, as depicted in Figs. 6.8a - 6.8d. The vehicle can fly at any speed maintaining the altitude and pitch at reference values since the aerodynamic force and moment differences are compensated by vertical rotors. Furthermore, Figures 6.6a and 6.6b highlight the changes in the speed during backward transition. It is evident from the graphs that both vehicles reach the hover condition by trimming u and w at zero. The tilt-rotor aircraft takes a longer time until the tilting of the front rotors are completed.

Pitch angle and rate should be evaluated simultaneously as one is the derivative of the other due to the assumptions made in the modeling section.In Figures 6.5f and

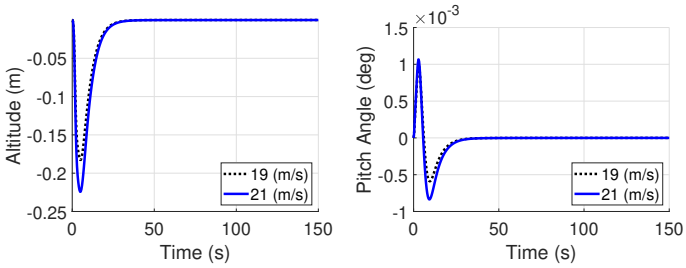

(a) Altitude.

(b) Pitch angle.

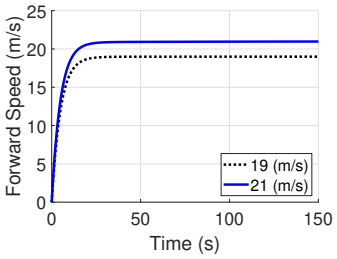

(c) Forward speed.

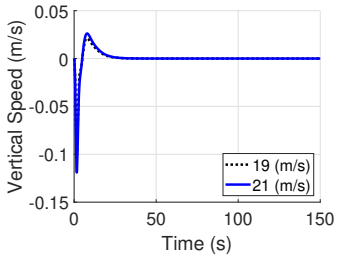

(d) Vertical speed.

Figure 6.8: Balanced altitude change and vertical speed during forward flight transition with other trim settings (19 and 21 m/s) for the pusher rotor configuration. Unlike the tilt-rotor case, the differences between the aerodynamic forces are compensated by the vertically-oriented rotors.

6.5c, the changes of θ and q are shown during the forward transition flight, respectively. The tilt-rotor configuration has a higher initial drop in θ, which is caused by the rapid tilting of the rotors as defined in the tilting function. Since the tilting rate reduces over the course of transition, the pitch-down motion is also recovered and the vehicle reaches the equilibrium condition. On the other hand, in the pusher configuration, the pusher rotor thrust proportionally corrects for the reduction of the thrust generated by the vertically-oriented rotors. Similarly, Figures 6.6f and 6.6c highlight the pitch motion during backward transition. It should be noted that a perching mechanism is added by letting θ increase to 2° to reduce the time needed for the tilt-rotor transition from forward flight to hover. In both transition flights, the pusher configuration shows a better performance, completing the transition with little changes in pitching.

In Figures 6.5d and 6.6d, the distances traveled during forward and backward tran-

sitions are presented. From hover to level flight, both of the configurations cover a distance of 3000 m and show a similar behavior, except for the initial 20 s where the tilt-rotor configuration needs longer time to reach the sufficient forward flight speed. However, for the backward transition, the forward travel distances are significantly different for each configuration. The tilt-rotor configuration requires approximately 900 m while the pusher configuration reaches the hover condition in less than 200 m. This difference can also be interpreted as the fact that the minimum distance required until landing by the tilt-rotor aircraft is almost 4 times longer than the one required for the pusher configuration. Therefore, trajectory planning should be made by accounting for this distance.

The final set of comparison is between the thrust components generated by the quadplane and pusher rotors. Figures 6.5g and 6.5h highlight the sum of the front and back rotor thrust components for the forward transition flight. As can be seen from these graphs, the final back rotor thrust reaches zero in a similar fashion for both configurations. However, the front rotor thrust components approach different values. In the tilt-rotor configuration, it trims at the same magnitude with the pusher rotor thrust of the other configuration, which is shown in Fig. 6.5i. Consequently, the thrust generated by the vertically-oriented rotors of the pusher configuration become eventually zero while the front rotors of the tilt-rotor configuration has to provide the sufficient thrust to remain airborne. Similarly, the changes of the thrust components during the backward transition flight are highlighted in Figs. 6.6g, 6.6h and 6.6i. Both the front and back rotor thrust reach half of the vehicle weight for both of the configurations and the hovering flight is achieved. In accordance with that the weight of the vehicles are balanced by the vertically-positioned rotors, the pusher rotor does not provide any thrust at hover condition.

Tilt-rotor altitude hold autopilot To develop an altitude hold autopilot, the altitude and forward speed are related by the fact that at steady level flight, $m\ddot{z} \cong (T_f + T_b) - mg + Cu^2$ where C is an aerodynamic coefficient. In this case, the rate of altitude change can be related to $m\Delta\ddot{z} = 2Cu\Delta u$ where Δ terms are the time derivatives of each parameter so that the altitude control is carried out after the transition is completed as in (6.13). Let $f(\Delta z)$ be the control input by the altitude controller

$$u_{com} = \begin{cases} u_{des}, & \text{if } \tau \leq \pi/2 \\ f(\Delta z), & \text{otherwise} \end{cases}. \tag{6.13}$$

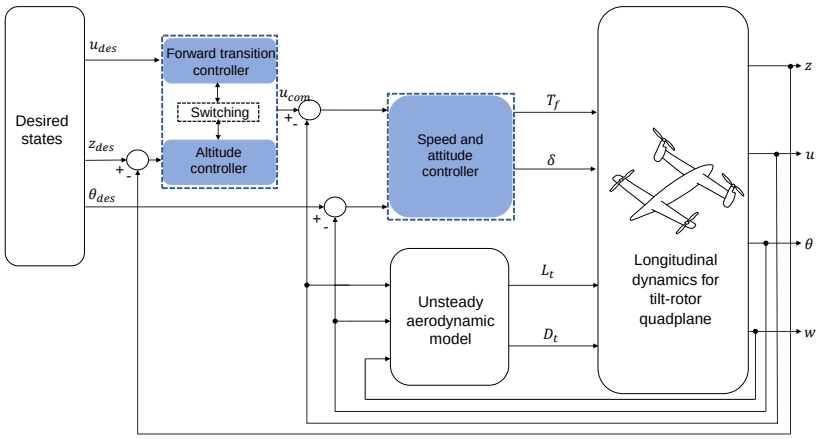

Figure 6.9: Tilt-rotor quadplane block diagram for forward transition and level flight. Initially, the transition controller is activated. After rotor tilting is completed, the altitude controller is switched on to calculate the speed reference. Note that for a cleaner view, actuator constraints are not included in the diagram.

For the backward transition flight, δ_T is derived considering the steady level flight thrust of the front rotors T_{ss} by (6.14).

$$\delta_T = T_f - T_{ss}. \tag{6.14}$$

The tilting function is selected as $\tau = (t/80s)^{0.15} \times \pi/2$ and $\tau = e^{(-1.5t/20s)} \times \pi/2$ for forward and backward transitions, respectively. t is the simulation time and the tilting angle is denoted by τ. For more information about tilting function selection, the reader may refer to [129]. Finally, the selected controller gains are listed for both configuration in Table 6.2.

Table 6.2: PID parameters for the forward and backward transition controllers of both configurations adapted from [8].

Pusher Forward				Pusher Backward			
Parameters	T_P	δk_1	δk_2	Parameters	δ_T	δk_1	δk_2
K_P	0.2	5	10	K_P	0.2	5	5
K_I	0.015	5	5	K_I	0.01	1	0
K_D	0	0.1	10	K_D	0.001	8	10

Tilt Forward			Tilt Backward			Tilt Level			
Parameters	T_f	δ	Parameters	δ_T	δ	Parameters	u_{des}	T_f	δ
K_P	0.3	1	K_P	-5	10	K_P	-1	0.3	1
K_I	0.015	1	K_I	-1.5	10	K_I	0	0.015	1
K_D	0.2	1	K_D	-5	1	K_D	-2	0.2	1

6.3.2 Full Flight Simulation Results

6.3.2.1 Forward Transition Flight under Disturbances

In this subsection, the effect of transition from hover to forward flight for both configurations is discussed in detail. The difference between the control strategies of the two configurations results in different responses. In the tilt-rotor case, as discussed earlier in Section 2, u and θ are the controlled state parameters until level flight condition is achieved. After the forces are trimmed for level flight, the altitude controller is switched on so that the vehicle approaches the desired altitude. On the other hand, for the pusher quadplane, there is one more degree of freedom provided by the pusher rotor, allowing for simultaneous control of u, θ, and z throughout the whole flight. This difference causes a significant change in altitude response of the tilt-rotor quadplane, when compared to its counterpart. In order to reduce the initial altitude loss in the tilt-rotor transition flight, the rotors should be tilted sufficiently fast. Furthermore, to reduce the magnitude of maximum error during tilting, PID gains can be tuned

aggressively. However, actuator responses are limited by their dynamic constraints. At this point, a T2FNN can be employed to learn the system response over the course of transition flight so that the oscillations are avoided without totally saturating the rotors. It is used along with a PD controller, which initially helps to keep the vehicle stable. One should note that PID controller produces very high control input due to the integral wind-up, which causes the UAV to oscillate excessively under varying disturbances. Therefore, instead of PID controller, PD controller is used along with T2FNN.

Another advantage of this type of a learning controller is its performance under uncertain conditions. Considering the dynamic change during transition flight, it is very susceptible to external disturbances. Therefore, in addition to the advantages in the tilt-rotor case, it can also be implemented in the pusher quadplane configuration for a better transition performance under varying disturbances such as wind gusts. For this purpose, the PD controller gains are kept the same as in Table 6.2 but without any integral gains. As for the initial control parameters of T2FNN in tilt-rotor configuration, the centers and deviations are set to $c_u = c_\theta = [-1, 0, 1]^T, \sigma_{1u} = \sigma_{1\theta} = [0.5, 0.5, 0.5]^T, \sigma_{2u} = \sigma_{2\theta} = [0.2, 0.2, 0.2]^T, \alpha_u = 0.001, \alpha_\theta = 0.01$, while the initial condition of time variable weight coefficient, $f_{ij}(0)$ is set to 0.001. The adaptive learning parameters for T2FNN are chosen as $\gamma_u = 0.01, \gamma_\theta = 0.5$. Similarly, for the pusher configuration, the centers and deviations are set to $c_u = c_\theta = c_z = [-1, 0, 1]^T, \sigma_{1u} = \sigma_{1\theta} = \sigma_{1z} = [0.5, 0.5, 0.5]^T, \sigma_{2u} = \sigma_{2\theta} = \sigma_{2z} = [0.2, 0.2, 0.2]^T, \alpha_u = 0.0001, \alpha_\theta = 0.05, \alpha_z = 0.001$, while $f_{ij}(0)$ is again set equal to 0.001. The adaptive learning parameters for T2FNN are chosen as $\gamma_u = \gamma_\theta = 0.05$.

The disturbance is applied onto the front rotors to simulate the effect of a wind gust, pushing the quadplane front rotors backwards. To do this, a 2 N force disturbance with a 0.5 N standard deviation is applied from the beginning of transition flight for the pusher quadplane (see Fig.6.10f) while it is kept at 1 N $\pm$ 0.5 m for the tilt-

rotor quadplane (see Fig. 6.11f). As can be seen in Figs. 6.10c and 6.11c, this causes the vehicles to delay while reaching their forward trim speeds in both configurations. Simultaneously, both configurations lose a portion of their altitude due to the rapidly growing vertical speeds in the first 10 s period (see Figs. 6.10b and 6.11b; 6.10d and 6.11d). After this point, the efficiency of the learning controller becomes more prominent as it takes over the control responsibility from the PD controller. In Figs. 6.10g, 6.10h and 6.10i, it can be seen that the T2FNN contribution to the total control input increases as PD response oscillates around zero. Accordingly, the pusher configuration with the learning controller has a better response in altitude hold as reflected in Fig. 6.10b. The forward speed response in Fig. 6.10c is also improved, especially at the beginning of the transition flight, by reducing the maximum overshoot. Furthermore, the tilt-rotor quadplane results indicate that the PID controller cannot complete the transition. With continuously increasing speed and altitude as highlighted in Figs. 6.11b and 6.11c, the vehicle adversely maneuvers to travel a 10 km distance (see Fig. 6.11a) and 600 m altitude change, which are definitely not desired. Counter-intuitively, the pitch controller still functions under these circumstances as shown in Fig. 6.11e. Similar to the pusher configuration, Figs. 6.11g and 6.11h show that T2FNN produces the main portion of the final control input. Overall control performance comparison between PID and the learning controller for pusher configuration is presented in Table 6.3. Since PID is not able to control the tilt-rotor quadplane under these disturbances, it is not possible to present the results in such a table.

Table 6.3: Performance comparison of proposed controllers for the pusher configuration.

Parameter	PID	PD+T2FNN	Improvement (%)
Max error in θ, e_θ	0.1884°	0.0104°	94.48
Overshoot in u	4.3234 m/s	1.9601 m/s	54.67
Max altitude change Δz	0.2547 m	0.1677 m	34.16
Root mean squred error (RMSE) $RMSE_\theta$	0.0706°	0.0016°	97.73
$RMSE_u$	3.1196 m/s	2.8391 m/s	8.99
$RMSE_z$	0.1115 m	0.0379 m	66.01

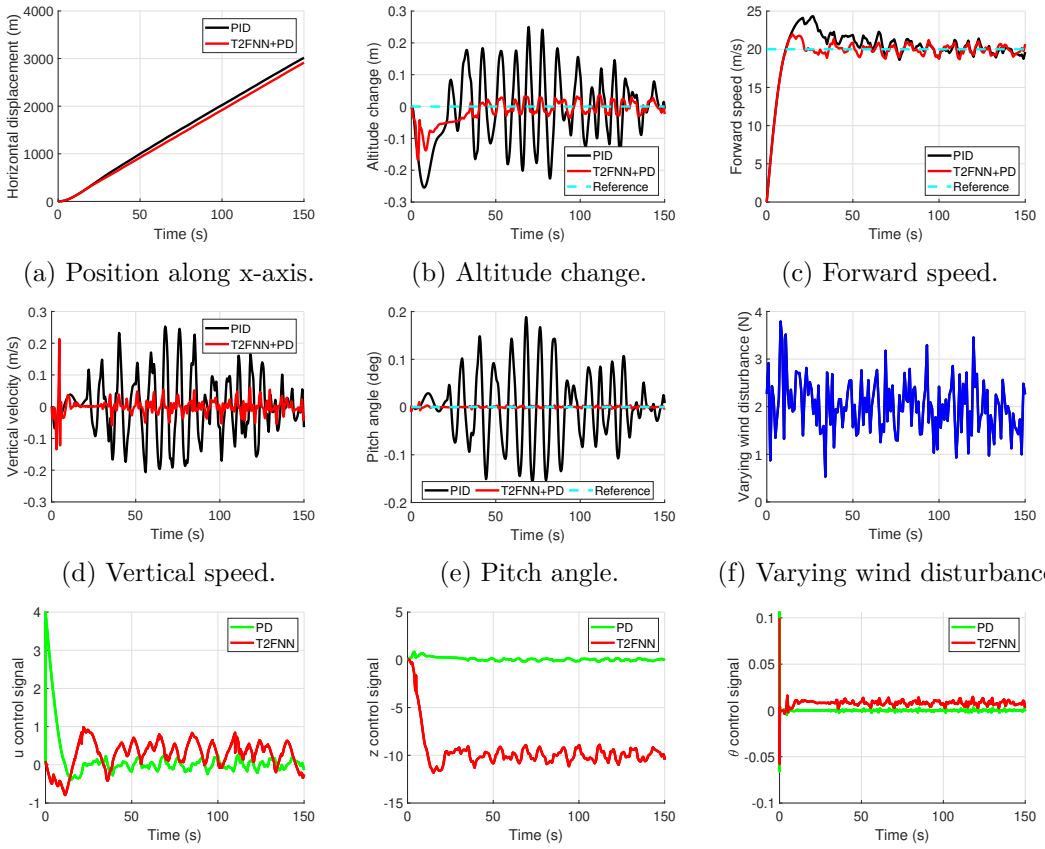

(a) Position along x-axis. (b) Altitude change. (c) Forward speed.

(d) Vertical speed. (e) Pitch angle. (f) Varying wind disturbance.

(g) u control signal. (h) z control signal. (i) θ control signal..

Figure 6.10: Comparison of the pusher configuration at forward transition phase with the disturbance of $\mu_{T_p} = 2N$, $\sigma_{T_p} = 0.5$ at the forward speed controller. Both T2FNN and PID controllers manage to come back to the desired transition trajectory.

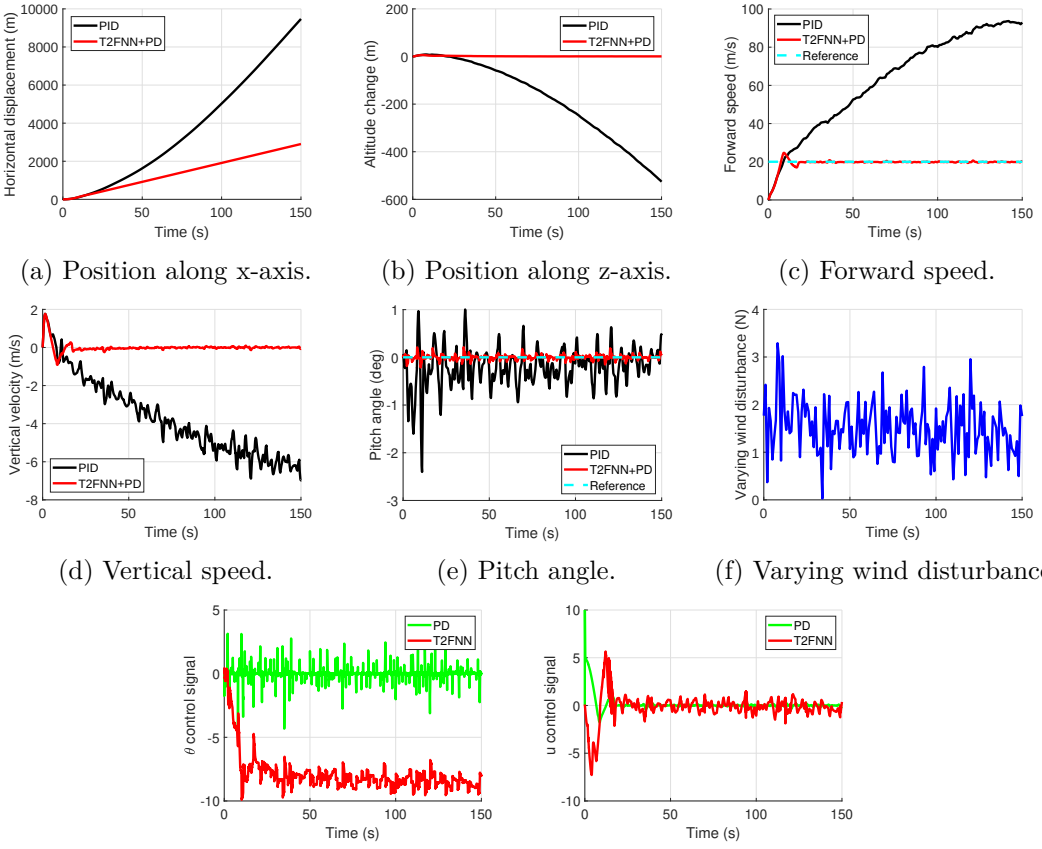

(a) Position along x-axis. (b) Position along z-axis. (c) Forward speed.

(d) Vertical speed. (e) Pitch angle. (f) Varying wind disturbance.

(g) θ control signal. (h) u control signal.

Figure 6.11: Comparison of the tilt-rotor configuration at forward transition phase with the disturbance of $\mu_{T_f} = 1N$, $\sigma_{T_f} = 0.5$ at the forward speed controller. T2FNN controller manages to come back to the desired transition pattern whereas PID controller cannot complete the transition successfully.

6.3.2.2 Full Flight Envelope Results

After the analysis of the learning controller under perturbed conditions, full flight envelope tracking results of both configurations are presented in Figs. 6.13 and 6.14 for the sake of completeness. The trajectory being tracked is as follows: the vehicles first climb up to 10 m altitude, which is followed by a forward transition to level flight. After the forward transition is completed and the level flight is ensured, backward transition to hover is carried out. Approximate trajectories of both quadplane configurations are presented in Fig. 6.12. To start with the interpretation of the simulation results, it is noteworthy that VTOL flight phases are identical for both configurations where only four vertically-oriented rotors are active (see Figs. 6.13a and 6.14a; 6.13b and 6.14b). This similar behavior is due to the assumption of similar inertial properties. For both vertical take-off and vertical landing phases, approximately 40 s are spared. Both quadplanes climb to 10 m in the first 10 s where the altitude control signals reach their peak points as in Figs. 6.13g and 6.14g. Since there is no other maneuver, u and θ control signals remain horizontal as shown in Figs. 6.13f and 6.14f; 6.13h and 6.14h.

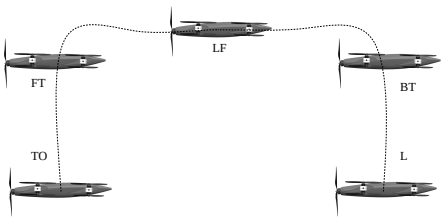

(a) Pusher quadplane approximate trajectory.

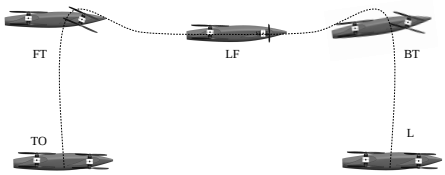

(b) Tilt-rotor quadplane approximate trajectory.

Figure 6.12: Approximate trajectories for both configurations. TO: Take-off, FT: Forward transition, LF: Level flight, BT: Backward transition, L:Landing. LF is included in FT for the rest of the thesis. During FT, the additional control channel provided by the pusher rotor leads to less altitude change in the pusher configuration. The altitude difference in the tilt-rotor configuration is shown with great exaggeration to point out this difference. In addition, during BT, pitch-up motion is critical for the completion of trajectory in the tilt-rotor configuration, which is not required in the pusher configuration.

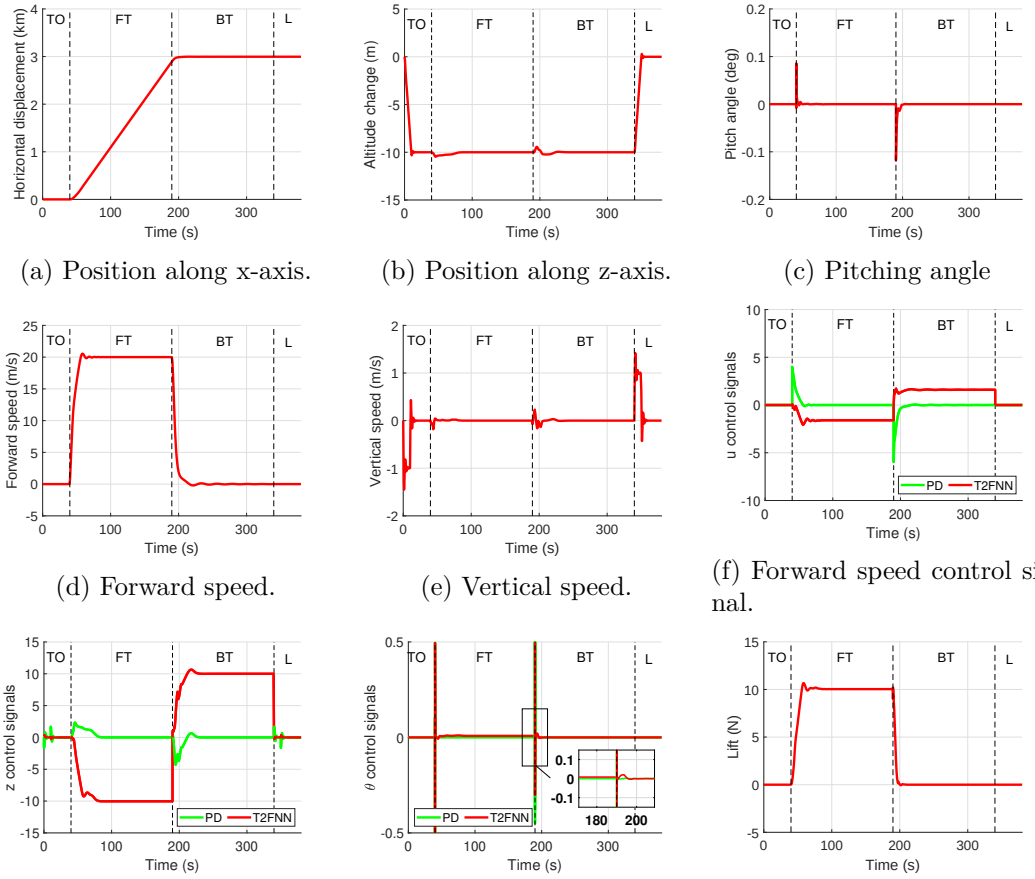

(a) Position along x-axis. (b) Position along z-axis. (c) Pitching angle

(d) Forward speed. (e) Vertical speed. (f) Forward speed control signal.

(g) Altitude control signal. (h) Pitch control signal. (i) Lift force.

Figure 6.13: The pusher configuration aircraft takes off, climbs up to 10 m, starts the transition flight, reaches the steady level flight and transitions back and lands. Unlike tilt-rotor configuration, pusher configuration has control over u, θ, and z during backward and forward transition as reflected in (f), (g), and (h).

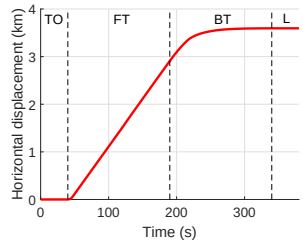

(a) Position along x-axis.

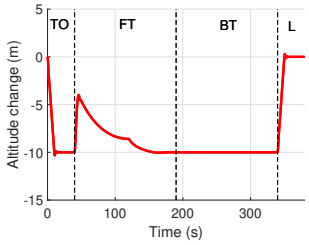

(b) Altitude.

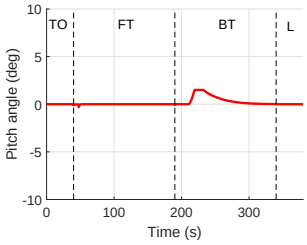

(c) Pitching angle.

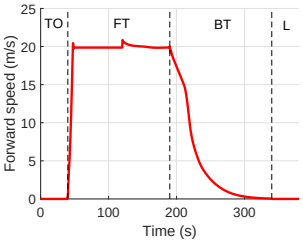

(d) Forward speed.

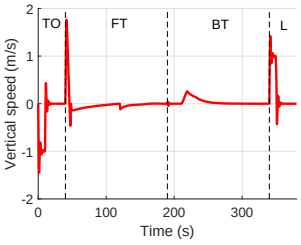

(e) Vertical speed.

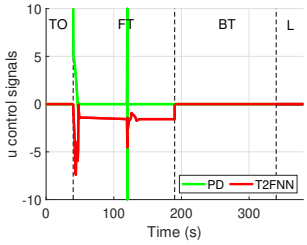

(f) Forward speed control signal.

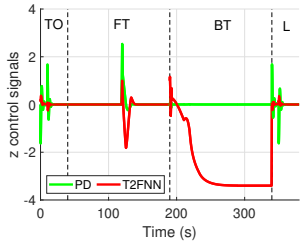

(g) Altitude control signal.

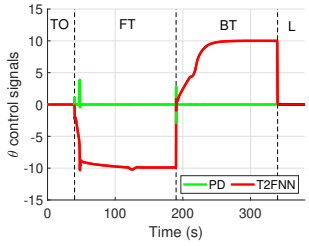

(h) Pitch control signal.

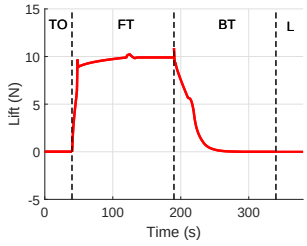

(i) Lift force.

Figure 6.14: The tilt configuration aircraft takes off, climbs up to 10 m, starts the transition flight, reaches the steady level flight and transitions back and lands. Depending on the flight type, controlled parameters are different as reflected in (f), (g), and (h).

After the vertical take-off phase, it is worth noting that the transition periods for tilt-rotor and pusher configurations are significantly different as highlighted in Figs. 6.13b and 6.14b. The tilt-rotor configuration needs another separate level flight algorithm whereas in the pusher configuration, forward flight transition and level flight can be controlled together in a sequel. For the tilt-rotor configuration, as there is no direct altitude controller during transition, the aircraft continues its motion at the trimming altitude after the transition is completed. At this point, the level flight algorithm is activated and the desired altitude is gained back. The crisp change in the altitude in Fig. 6.14b and forward speed in Fig. 6.14d are due to this switch from the transition flight controller to the level flight controller. On the other hand, when Fig. 6.13b is observed, it can be seen that the pusher quadplane does not deviate from the reference altitude of 10 m as much as the tilt-rotor quadplane does. Throughout the transition and level flight, altitude controller is active due to the additional control channel provided by the pusher rotor. Therefore, the altitude changes in the pusher quadplane are reduced significantly when compared to its counterpart. Overall, the forward transition and cruise flight durations altogether are kept in 150 s. The forward travel for both configurations are similar and approximately 2.9 km (see Fig. 6.13a and 6.14a). In following, when transitioning backwards to the hover condition, the control parameters are changed to altitude and pitch angle for the tilt-rotor configuration. With the increasing backward tilting angle, the forward flight speed decreases naturally. However, this behavior continues asymptotically, which results in an impractically long backward transition period. To reduce it to a similar duration required for the pusher quadplane (150 s), a pitch-up motion is needed as in Fig. 6.14c. The corresponding vertical speed change is also seen in Fig. 6.14e. For the pusher quadplane, the pitch angle can be kept zero as in Fig. 6.13c without a significant change in the vertical speed (see Fig. 6.13e). Unlike forward transition, the altitude deviations during backward transition can be kept minimal for both configurations as reflected in Figs. 6.13b and 6.14b. However,

the difference is in the forward travel as the tilt-rotor quadplane takes 0.5 km more than the pusher quadplane until the backward transition is completed. Finally, similar to the take-off phase, both vehicles successfully complete landing maneuver. The total duration for completing the full flight envelope is 380 s.

6.4 Summary

The unsteady aerodynamic model is able to represent the fast changes in the aerodynamic forces during forward and backward transition. In this study, full flight envelope control problems are investigated for two quadplane configurations, namely a pusher and a tilt-rotor configuration with an unsteady aerodynamic model. It is observed that the sensitivity to trim state is observed for both of the configurations. The pusher configuration maintains steady level flight regardless of the trim speed, whereas the tilt-rotor configuration is sensitive to the trim speed. In the second part of the study, noticing that the transition flight phase is the most sensitive segment of the flight envelope to disturbances, T2FNN-based learning controllers are implemented to cope with varying wind gusts. It is evident from the results that the learning controller outperforms PID controller in case of disturbances. In the PID-controlled pusher configuration, the disturbances cause excessive oscillations in all state parameters, whereas the learning controller rejects the disturbances much faster and reduces the noise level significantly.

Chapter 7

Conclusion and Future Work

7.1 AM for Small-Scale Aerial Vehicles

AM techniques were examined in this thesis for the manufacture of VTOL UAVs. Different AM methods are explored; different build orientations, print orientations and bending samples were tested in the lab to determine the strength and flexural stiffness. A FE model obtained by the experimental data was later used to explore several optimization trends. The selected internal structure is then compared with periodic cellular structures in terms of weight and strength. An objective of this research was to examine the possibility of manufacturing the complete VTOL UAV using AM as literature suggested that AM is mostly used to manufacture functional parts. A few key conclusions from this study on the use of AM are

1. Mechanical characterization of the FDM parts carried out by manufacturing using ABS in different build (edge-up, face-up and straight-up) and print orientations (0–90°) was conducted. Flexural behavior of flat and curved CLFDM samples in different build and print orientations were experimentally investigated by calculating the bending stiffness coefficient (F/d). It is concluded that the build orientation has a larger impact than print orientation on the elastic deformation of an FDM printed part. Hence, an averaged isotropic simulation model can be

used for different print orientations but not for different build orientations due to the varying flexural stiffness coefficient, which is found to be more than 10% in all tests.

2. An optimal rib–spar–skin thickness combination is achieved via FE and the above-mentioned analyses, which is then compared to a body consisting of periodic structures - in terms of structural weight. As periodic structures, diamond honeycomb and 3D-Kagome are tested for their bending performances and it is concluded that diamond honeycomb is more favorable with AM. By using diamond honeycomb as interior structure, the overall structural weight is reduced by approximately 35% of the rib–spar model weight. It is also noted that, for FDM, joining methods are critical for the structural integrity and periodic structures cured together showed superior strength when compared to mechanical joints.

7.2 Modeling and Control

Two different aerodynamic models are utilized to estimate the forces during transition. In the first model, a quasi-steady model is used to determine the forces for a database (CFD and DATCOM). In the second model, an unsteady lumped vortex model is used to determine the forces by solving and coupling the flow equations to the dynamic equations.

Quasi-Steady Aerodynamic Model: Flying Wing

The quasi-steady aerodynamic model is used for a tilt-rotor flying-wing vehicle. The control surfaces and differential thrust between the rotors are used as control inputs simultaneously. The nonlinear model is linearized at ten different tilt angles over the course of transition flight. Conventional PID controllers are designed for these models and tuned by minimizing a pre-defined cost function. For the angles in-between the linearizations, linear interpolations are carried out to calculate the controller gains. The

effect of varying tilting rate is also investigated with this model, which is manipulated by a fuzzy logic based algorithm. Finally, a T2FNN-based learning controller is tested under disturbances and its performance is compared with the linear controllers. The key findings of this study are:

1. Since controllers are designed at linearization points and then interpolated for the angles in-between, the quasi-steady simulation with gain-scheduling indicated that the controller gains were affected not only by the tilting motion but also by the propeller stream; however, the overall transition motion was not interrupted or stalled due to the propeller downstream.

2. The varying tilting rate is manipulated by a fuzzy logic algorithm, which decelerates the tilting motion when oscillations were present and vice versa when the oscillations were negligible. Without loss of generality, it can be claimed that the discontinuities between the models could be reduced by varying the transition rate.

3. A T2FNN-assisted PD controller is applied to the vehicle to evaluate its performance under disturbances. To avoid any unstable conditions, PD gains could be tuned roughly to bring the system to an –at least– marginally stable condition and the rest of the control action would be adjusted by T2FNN. In conformity with the theory, the learning controller helped to attenuate the altitude oscillations caused by the disturbances whereas conventional PIDs could not. The algorithm update rate is kept at 20 Hz for future hardware implementations, which is less than 50 Hz of current data update/transmission rate, an average acceptable rate for onboard computers.

Unsteady Aerodynamic Model: Quadplanes

Full flight envelope control problem for two quadplane configurations (a pusher and a tilt-rotor) is investigated using an unsteady lumped vortex model. PID and

the learning controller are tested at nominal conditions as well as under disturbances. Below are the conclusions drawn from the simulations:

1. Since the aerodynamic nonlinearity is directly implemented in this model, it mainly eliminates the need for a quasi-steady aerodynamic model with gain scheduling by representing the fast changes in the aerodynamic forces during forward and backward transitions.

2. The simulations indicate that the transition duration heavily depends on the inertia of the model, aerodynamic lag effects during transition or disturbances, and availability of excess thrust, which is used for rapidly balancing the system.

3. The significance of the unsteady aerodynamic effects at the beginning and end of transition motion is clearly shown. Yet, their effect could be reduced with more aggressive controller gain selection.

4. The tilt-rotor quadplane had significant challenges in terms of control than its counterpart did. The tilt-rotor configuration had a significant 1 m altitude change for forward transition and took longer time to reach the steady hover after backward transition. Unlike the pusher vehicle, the tilt-rotor system was also sensitive to the trim speed.

5. The simulations indicate that PID controllers could stabilize the pusher but not the tilt-rotor configuration during forward transition and the nonlinear controller had to be implemented for the latter vehicle.

7.3 Future Work

There are several design options for a hybrid VTOL vehicle such as tail-sitters, tilt-wings or tilt-rotors and quadplanes. In this thesis, tilt-rotor and quadplane configurations are selected as their bodies remain horizontal during transition flight, which

enhances their stability. However, it should be noted that the design stage can be further extended; various configurations can be compared, tested and aerodynamically more efficient structures can be achieved. For instance, a tilt-wing system would have a more complicated aerodynamic model, requiring extensive analyses at high angles of attack. Unlike a tilt-rotor system, a tail-sitter would be more prone to crosswinds and disturbances during transitioning but would have more options for optimal transition trajectories. In short, alternative VTOL vehicles could be tested in the future for finding more efficient designs applicable to real-time engineering problems.

For near future, validation of the control strategies can be implemented and tested on a VTOL UAV optimized for weight and manufactured using an AM technique. Tests can be conducted to:

1. Show that the optimization of weight is achievable using cellular periodic structures. To do this, FE models of cellular structures can be prepared using the material data collected in this study. By this manner, structural weight of the vehicle can be further reduced.

2. The designs in this thesis lack of the impact resistance analyses, which became a significant problem during landing tests. In the future, when designing an AM vehicle body, this parameter should also be included in the design stage as FDM components are proven to be prone to high impact loads during landing. Furthermore, to improve the design quality, a full flight load analysis could be conducted to determine the highest load factor acting on the body during operation.

3. Compare unsteady aerodynamic models to quasi-steady models for controlling a vehicle for full flight envelope. The effects of the assumptions made for the models can be investigated by experimenting a suddenly accelerating system in a wind tunnel. However, the wind tunnel should be equipped with the necessary fixtures to measure the differences between the static and dynamic tests.

4. Extend the unsteady analysis to lateral-directional motion. Furthermore, the model can fully account for the interference effects between the wings and the unsteady upwash and downwash in the new model.

5. Check the robustness of different controller implementations such as PID vs T2FNN based controller for various flight conditions. To do this, a realistic simulation environment such as Gazebo platform can be used so that the hardware testing phase can be accelerated. However, the Gazebo aerodynamic scripts should be replaced with the proposed aerodynamic models and the differences between them should also be investigated.

6. Monte Carlo or another batch simulation technique can be benefited for (i) determination of linearization points of the quasi-steady model, (ii) selection of controller gains and (iii) control of the vehicle under uncertain conditions such as wind gust or irregularities with thrust generation, e.g., rotor failure or damaged propeller. By this manner, instead of linearizations with 10-degree intervals, optimal locations of models and their corresponding controller gains could be detected for a better model representation and control performance. On the other hand, when an unsteady model to be implemented, this method would be used only for an optimal gain selection as no linear models would be required anymore.

7. Consider how to improve the transition trajectory for different scenarios such as for best range or for best endurance. Accordingly, alternative flight trajectories may be developed by manipulating various parameters such as tilting duration, start of the tilting motion, initial lift-off velocity.

Appendix A

Design of Flying Wing

A.1 CAD Model

The requirements for the maximum take-off weight of the UAV is estimated to fall between 3.5-4 kg. The aspect ratio (AR) is computed by knowing the wing span of the UAV, considering it as a design requirement. In this calculation, wingspan (b) is limited to 1 m to cut down the manufacturing cost and the duration of 3D printing. V_{stall} and C_{Lmax} are 12 m/s and 1.2 for safety. The minimum surface area (S) and the AR are calculated to be 0.426 m^2 and 2.7, respectively.

The chord lengths and positions of the point masses are adjusted such that the longitudinal static stability requirement ($C_{m_\alpha} < 0$) is satisfied while keeping the trim angle in the desired range. For this purpose, wings are also swept backwards with a 22.5° sweep angle.

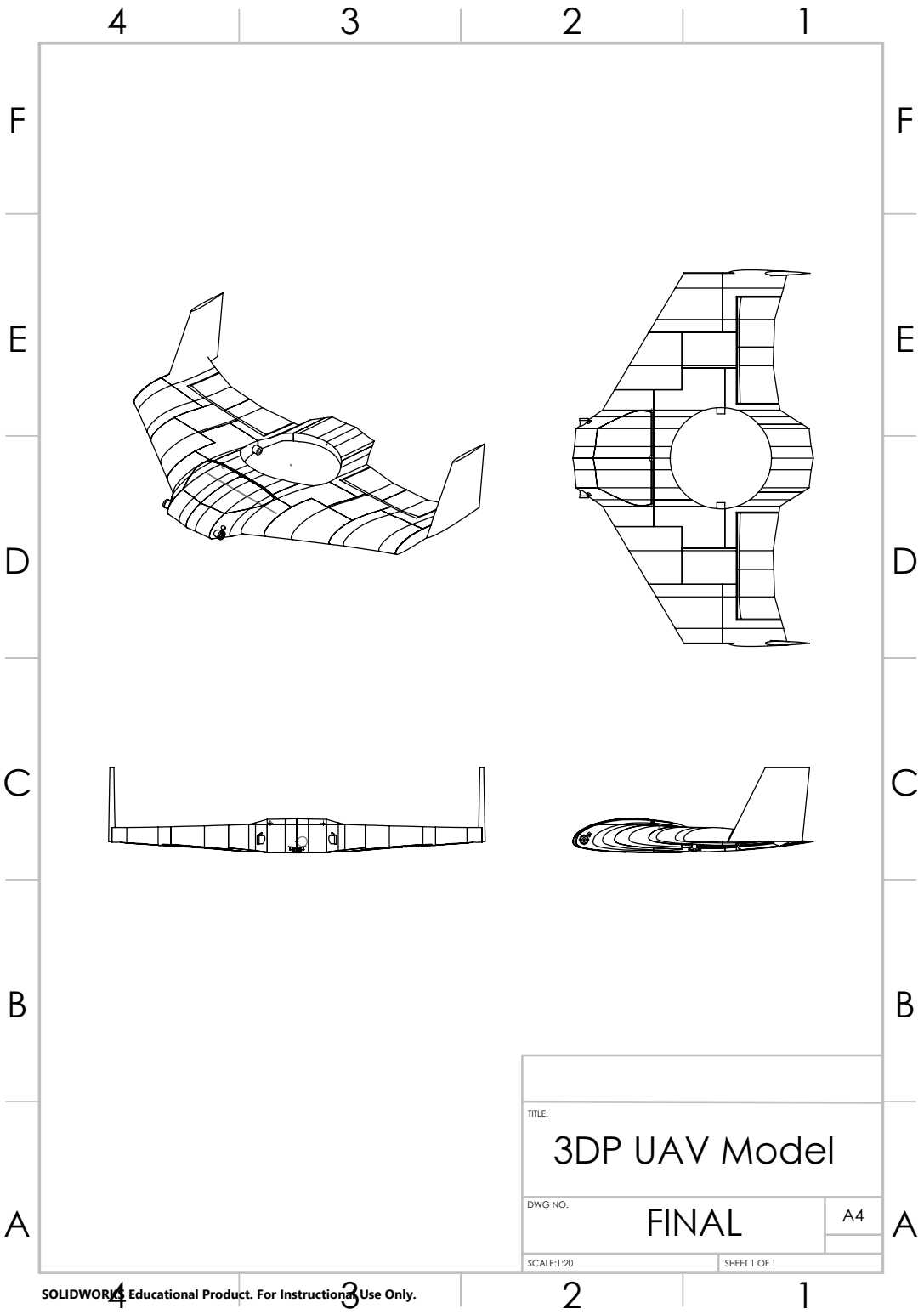

Figure A.1: CAD model of the 3D-printed UAVs.

A.2 Airfoil Selection

The pitching characteristics of conventional airfoils are mostly destabilizing along the longitudinal axis of a plane and the pitching moment increases with angle of attack, i.e. $C_{m_\alpha} > 0$ [130]. This problem can be rectified by the attachment of a horizontal tail unit to balance the pitching moment for conventional planes. For a flying wing, either airfoil or some other structural modification techniques such as back-sweeping of the wings or twisting are needed to compensate for lack of tail [131]. In this context, reflexed airfoils are one of the commonly used solutions. Unlike conventional airfoils, reflexed airfoils have a negative camber at the trailing edge region which results in a self-balancing pitching moment by the airfoil, which has a lower lift efficiency compared to a cambered airfoil [132]. Consequently, a group of candidate reflexed airfoils are considered (Fauvel, S5010, S5020 and Wortmann FX05-H-126) and simulated in XFLR5, to determine an appropriate airfoil that provides sufficient lift at an achievable trim angle of attack, while maintaining longitudinal stability.

XFLR5 analyzes the stability of the vehicle by (i) performing a 2D airfoil analysis and (ii) a 3D vortex lattice aerodynamic analysis of the model. For the 2D airfoil analysis, each airfoil is analyzed using the semi-empirical models implemented by XFOIL [133] in a range of Reynolds number and angle of attack. In order to cover the whole possible range of flight, the Reynolds number range is 30,000 to 2,500,000 and angle of attack of [-10°,10°]. Figure A.2 depicts the C_L vs α , C_L vs C_D, C_m vs α characteristics of the airfoils.

Fauvel airfoil is selected as the main profile of the wing to be designed. Most importantly, Fauvel has a better lift performance compared to the other candidate airfoils. Besides, as it will be seen later, having a slightly positive moment coefficient at 0° of angle of attack enhances the longitudinal stability of a plane. This is due to the easier achievement of a positive trim angle of attack at a reasonable cruise flight

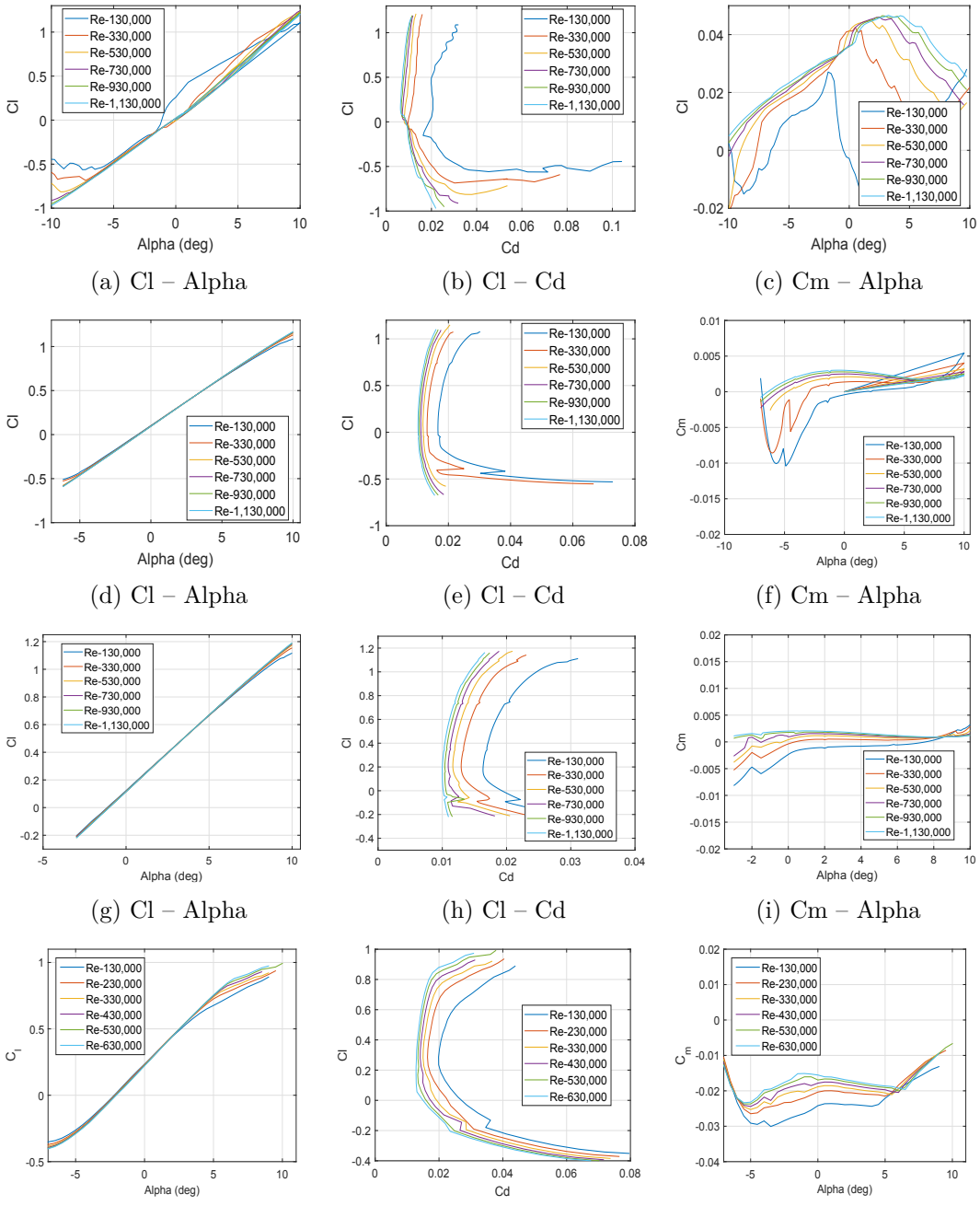

(a) Cl – Alpha (b) Cl – Cd (c) Cm – Alpha

(d) Cl – Alpha (e) Cl – Cd (f) Cm – Alpha

(g) Cl – Alpha (h) Cl – Cd (i) Cm – Alpha

(j) Cl – Alpha (k) Cl – Cd (l) Cm – Alpha

Figure A.2: Airfoil characteristics for Fauvel (a), (b), (c); S5010 (d), (e), (f); S5020 (g), (h), (i); and Wortmann FX05-H-126 (j), (k), (l).

speed.

3D analysis of the flying wing is then performed to determine the vehicle stability and trim conditions. The fixed lift analysis is selected for this study. The appropriate mass distributions are imported from the CAD file so that the correct trim and stability derivatives can be calculated.

From the performance curves shown in Fig. A.3, the trim angle of attack is found to be 6.4. The cruise $C_L, L/D$ and the flight speed is found to be 0.388, 16.25 and 16.6 m/s, respectively. After obtaining the longitudinal static stability, lateral and directional static stability requirements ($C_n > 0$ and $C_l < 0$) are also satisfied for a side-slip angle range of -25° to 25°. The lateral and directional stability analyses are conducted by varying the side-slip angle, keeping the velocity (16.6 m/s) and the angle of attack (6.4) constant.

Other than the non-structural masses, static and dynamic longitudinal stability characteristics are manipulated by several design parameters as well. For instance, the presence of dihedral and the wing-tip plates aid in the directional stability of the flying wing UAV. Thus, a sufficiently large wingtip plate with the symmetric NACA 0009 airfoil are attached to the trailing edge of the wingtips provided the desired performance. For this purpose, a 2D analysis for the NACA 0009 is also carried out. After the modifications mentioned above, the Dutch roll mode is also finally stabilized. The root loci of the corresponding modes are seen in Fig. A.3.

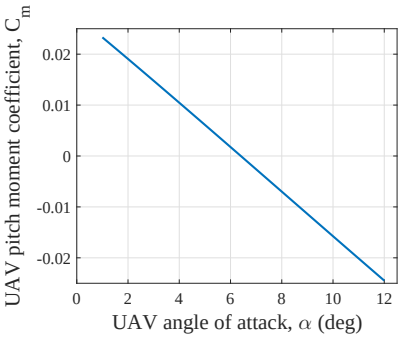

(a) Longitudinal stability plot.

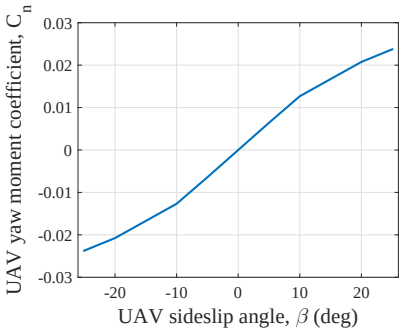

(b) Directional stability plot.

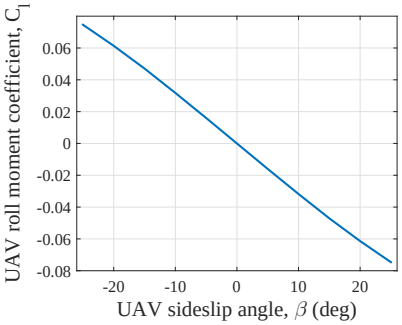

(c) Lateral stability plot.

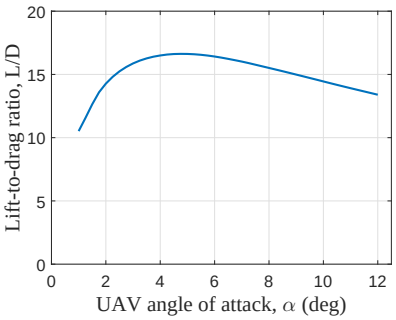

(d) Lift to drag ratio.

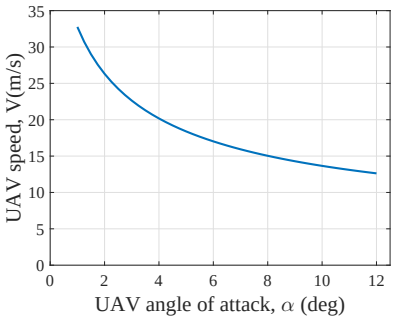

(e) Velocity vs the AOA.

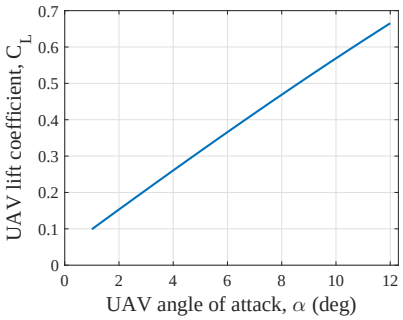

(f) Lift coefficient vs AOA.

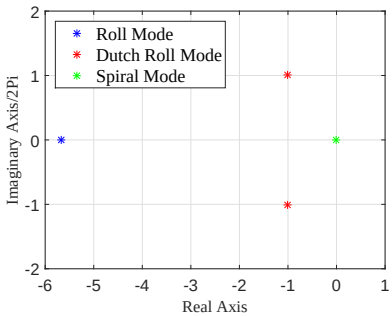

(g) Lateral and directional.

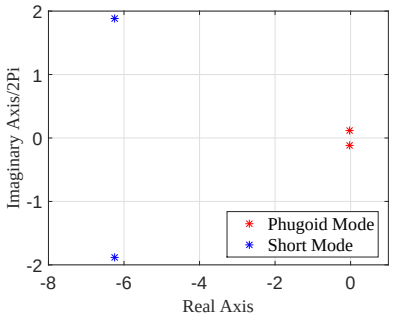

(h) Longitudinal.

Figure A.3: Performance and root locus plots of the planform design.

A.3 Fixture for Bending Testing and Testing Procedure

The bending tests are carried out using the Shimadzu Autographer Universal testing machine. One cantilever beam fixture is manufactured using Aluminium 6061 specifically to clamp the cantilever beam in position so that it does not shift in the transverse direction from the longitudinal axis of the beam during an experiment. In Fig. A.4, the fixture along with a specimen mounted on the testing machine is shown. The experiments are carried out at a testing speed of 1.3mm/min with a stroke limit of 50mm. Normally, the testing is completed when a brittle fracture occurs at the cantilever beam root. This shows that the core structure distributes the load from the edge to the root of the cantilever beam as planned. In some rare cases, the core material fails due to the compression instead of bending, which indicates that there are some printing defects and the sample needs to be discarded. Each experiment is repeated at least 3 times to obtain a reliable result, excluding the discarded samples.

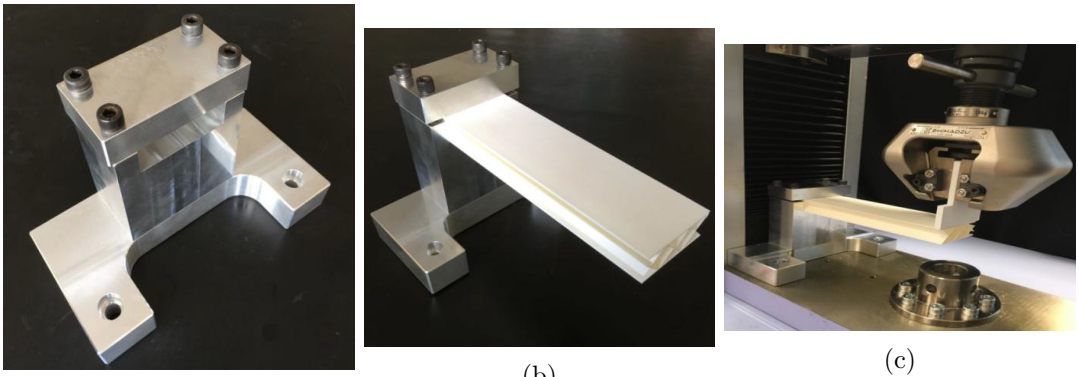

(a) (b) (c)

Figure A.4: Cantilever beam fixture (left), Cantilever beam attached to fixture (middle). Cantilever beam experimental set-up (right) [72].

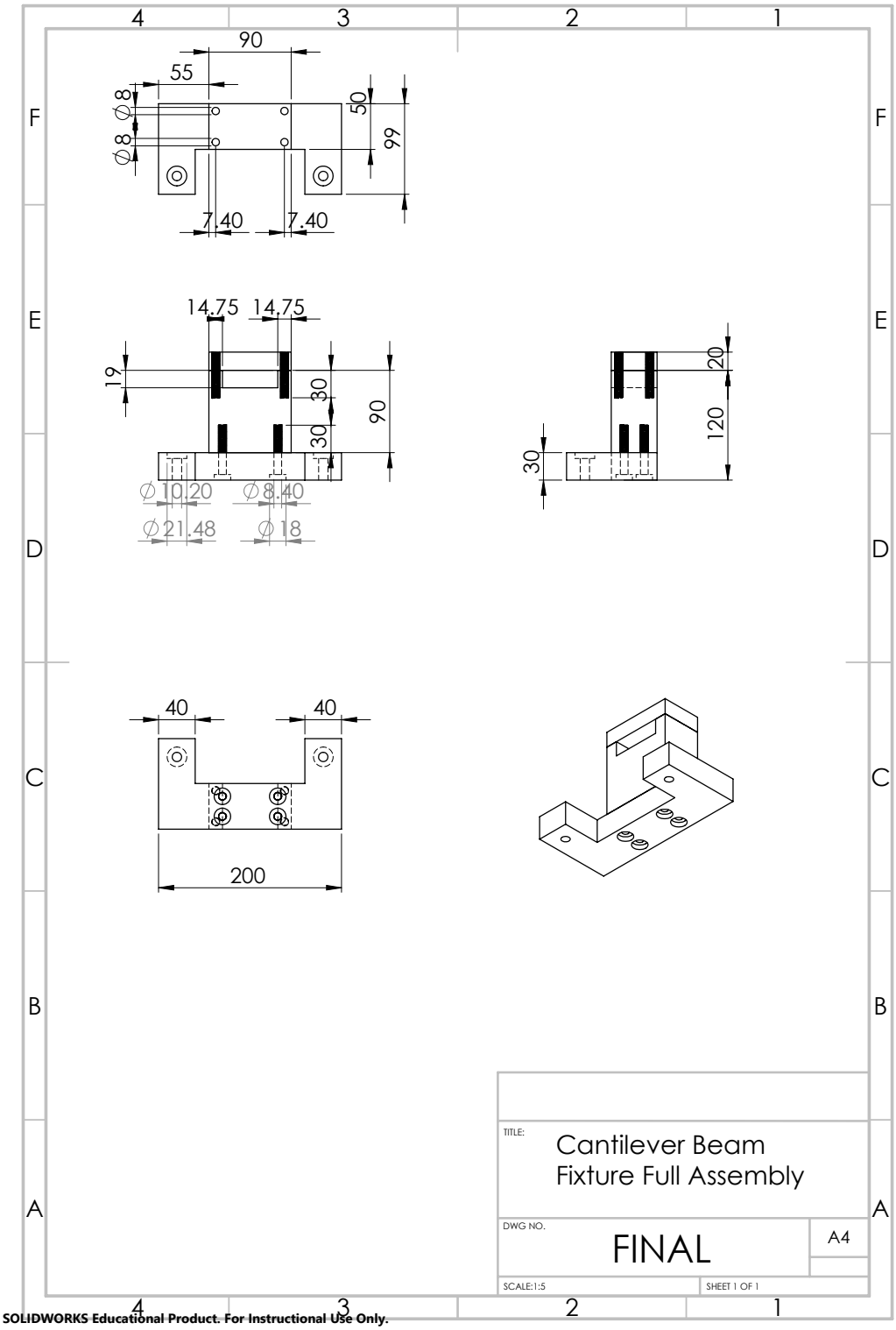

Figure A.5: CAD model of the fixture for bending testing adapted from [119].

Appendix B

Wind Tunnel Tests

Experimental results obtained from wind tunnel tests are presented to compare with XFLR5. The main purpose is to validate the numerical data in the range of 0° to 10° as it is difficult to obtain experimental data for all the stability derivatives.

B.1 Wind Tunnel

Given the pitch angle limitation in the wind tunnel, in order to obtain the high angles of attack data, wind tunnel tests are conducted with 3 models, each covering different ranges of angle of attack. Basically, the extruded cut in the middle of each model is changed so that it is mounted directly onto the wind tunnel strain gauge. An illustration of this concept is presented in Fig. B.1. The infill rates are adjusted to keep the CG of the models at the same location, 99 mm behind the tip of the body. Other common properties of proposed designs are detailed in Table B.1.

B.1.1 Wind Tunnel Facility

The wind tunnel utilized is a low speed, closed-loop wind tunnel, with test speeds varying from 3-90 m/s. The wind tunnel is equipped with multiple meshes and a high

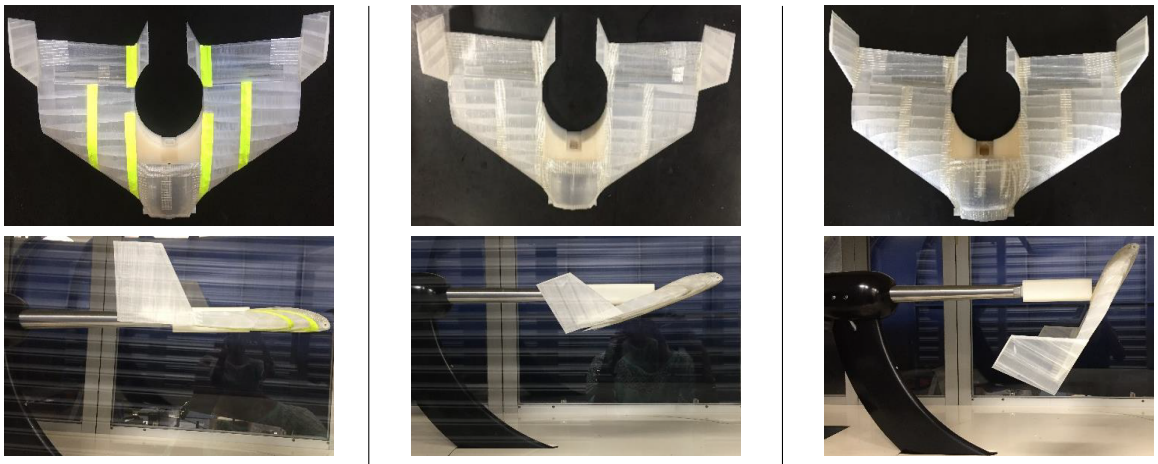

Model 1: Mounted at 0°	Model 2: Mounted at 25°	Model 3: Mounted at 60°
Range of α for testing 0°-25°	Range of α for testing 25°-50°	Range of α for testing 60°-85°

Figure B.1: Concept of proposed design for high angles of attack testing.

Table B.1: Important common features of the wind tunnel models [134].

Parameter	**Value**
Wing Span (b)	0.500 m
Mean Aerodynamic Chord (c)	0.230 m
Centre of Gravity	(0.099, 0.0005, 0) m
Area (S)	0.0910 m
Aspect Ratio (AR)	2.75

contraction ratio to ensure low turbulence level of approximately 0.1 %. It has a test section size of $0.780 \times 0.720 \times 2.000m$. It is equipped with a sting support and a six-component internal balance which is capable of measuring the axial, normal and side forces as well as roll, yaw and pitch moments. The model positioning system is capable of rotating the model about the roll, pitch and yaw axes. The maximum magnitude of forces measured are 500, 1000, and 800 N, respectively for the axial, normal and side force. The deflection ranges are [-45°, +45°], [-40°, +40°] and [-15°, +25°], respectively for roll, yaw, and pitch.

B.1.2 Test Procedure and Experimental Setup

Tunnel corrections such as blockage and wall corrections to raw data obtained are accounted for [135]. Moreover, the forces and moments measured at the balance centre of the wind tunnel strain gauge are transferred to the CG of the model for further analysis of the aerodynamic properties. These corrections and transformation of forces and moments are detailed in the following sections.

Solid Blockage and Wake Blockage Corrections. Solid blockage (ε_{sb}) is the ratio of the frontal area of the model exposed to the flow to the cross-sectional area of the flow. Wake blockage (ε_{wb}) refers to effect arising from the size of the wake of the UAV after the incoming air has passed over it. The solid blockage and wake blockage can be summed up as total blockage (ε_t) as $\varepsilon_t = \varepsilon_{sb} + \varepsilon_{wb}$ [135], where

$$\varepsilon_t = \frac{1}{4} \times \frac{\text{frontal area of model}}{\text{cross - sectional area of test section}} \tag{B.1}$$

Since the frontal area of the model varies with the angle of attack, the total blockage correction factor also varies with the angle of attack, as shown in Fig. B.2. The total

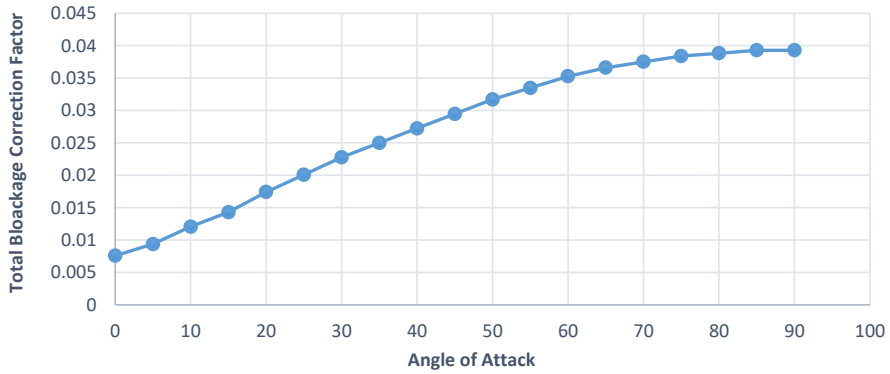

Figure B.2: Variation of Total Blockage Correction against Angle of Attack for UAV model.

blockage correction factor is used to calculate the corrected velocity (v_c) and corrected

dynamic pressure (q_c) as shown in at each angle of attack tested [135]:

$$\begin{aligned} v_c &= v_a\,(1+\varepsilon_t) \\ q_c &= q_a\,(1+\varepsilon_t)^2 \end{aligned} \tag{B.2}$$

where v_a is the actual velocity and q_a is the actual dynamic pressure. The corrected dynamic pressure is used in the calculation of the lift, drag and moment coefficients which are elaborated in the following sections.

Correction for Wall Induced Effects. Wall induced effects are present in wind tunnel testing as they interfere with the flow field. Hence, wall corrections had to be made to the angle of attack, drag coefficient and pitching moment coefficient. The span wise distribution of the lift can either be assumed as elliptic or uniform in order to determine the boundary correction factor (δ). For the UAV model in this study, the lift distribution is assumed to be closer to an elliptic rather than a uniform distribution. Other ratios, i.e., k and λ, are used to determine the appropriate boundary correction factor through interpolation [134] as $k = \frac{\text{wing span}}{\text{width of test section}} = 0.642$ and $\lambda = \frac{\text{tunnel height}}{\text{tunnel width}} = 0.923$, respectively. The corrected angle of attack (α_C) is calculated by

$$\alpha_C = \alpha_g + \Delta\alpha_{up} + \Delta\alpha_w \tag{B.3}$$

where α_g is the geometric angle of attack measured, $\Delta\alpha_{up}$ is the wind tunnel up wash angle to be neglected in this case and $\Delta\alpha_w$ is the additional angle due to the wall induced effects via

$$\Delta\alpha_w = \delta\frac{S}{C}(57.3)C_{LW} \tag{B.4}$$

where δ is determined as 0.143 from [134], S is the wing planform area, C is the flow cross sectional area and C_{LW} is the lift coefficient of the wing. Since the UAV model is of a flying wing configuration, its wings are the primary generator of the lift and

hence, C_{LW} is substituted with C_L. In following, the corrected drag coefficient C_{D_c} is calculated as:

$$C_{D_C} = C_{D_U} + \Delta C_{D,up} + \Delta C_{D_W} \tag{B.5}$$

where C_{D_U} is the uncorrected drag coefficient; $\Delta C_{D,up}$ is the additional drag coefficient due to the wind tunnel up wash angle [134] and ΔC_{D_W} is the additional drag coefficient due to the wall induced effects.

$$\begin{aligned} \Delta C_{D,up} &= C_{LW} \Delta \alpha_{up} \\ \Delta C_{D_W} &= \delta \frac{S}{C} C_{LW}^2 \end{aligned} \tag{B.6}$$

The corrected pitching moment coefficient (C_M) is calculated as:

$$C_M = C_{M_{Y@CG_U}} + \Delta C_{M_{Y@CG_t}} \tag{B.7}$$

where $C_{M_{Y@CG_U}}$ is the uncorrected pitching moment coefficient and $\Delta C_{M_{Y@CG_t}}$ is the additional pitching moment coefficient proportional to the change in angle of attack of the tail unit [134], which is neglected as the UAV is of a flying wing configuration.

B.2 Experimental Results

Figure B.3 illustrates the $C_L - \alpha, C_D - \alpha$ and $C_M - \alpha$ (measured at CG). The stall angle of attack is 19°. From the $C_M - \alpha$ curve, it can be observed that the UAV is longitudinally stable.

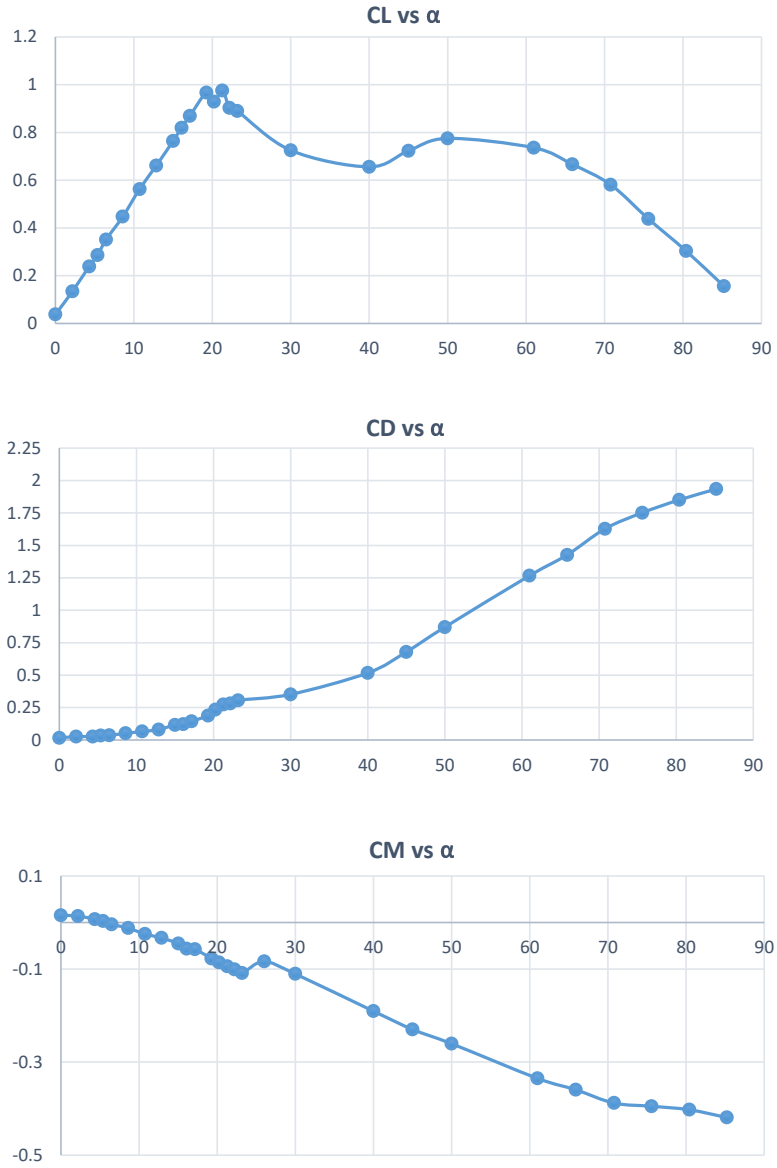

Figure B.3: C_L vs α, C_D vs α and $C_{MY@CG}$ vs α graphs for the UAV model.

Appendix C

CFD Analysis

The results obtained from CFD are compared to XFLR5 to determine whether XFLR5 is reliable. XFLR5 simulations are unable to predict values after 15° for U=20m/s and after 10° for U=5m/s. Figures C.1a and C.1b show that C_L and C_D obtained from CFD simulation are constantly higher than XFLR5 simulations. $C_{L\alpha}$ from CFD and XFLR5 are similar. XFLR5 results are independent of flow velocity, whereas CFD has some Re variability as seen from the plots. Stall is not possible in XFLR5. XFLR5 underestimates C_D when compared to CFD. Figure C.1c shows that C_m curve obtained from XFLR5 trims at a high angle but the plots that were obtained from CFD have lower trim angles. $C_{m\alpha}$ for CFD and XFLR5 are different. C_m obtained from XFLR5 does not have a large difference with varying velocities at the same α. However, CFD shows that C_m values have a larger difference in values when velocity is varied at the same α. XFLR5 is also unable to simulate for the increase in C_m after stall angles.

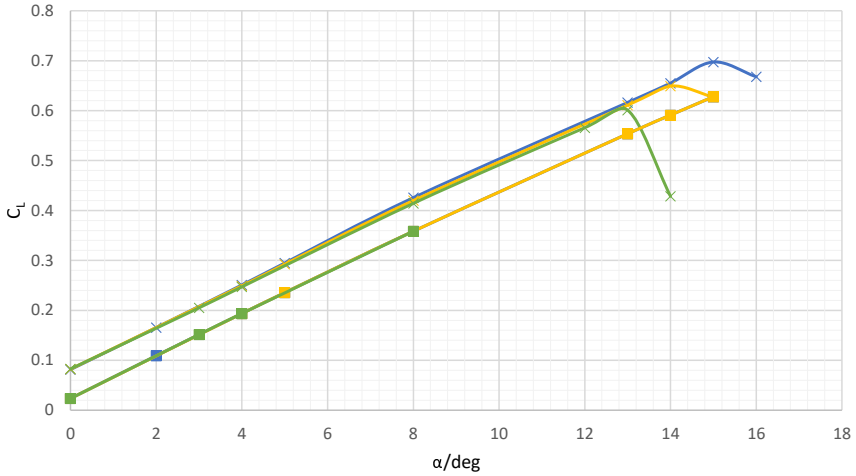

(a) $C_D - \alpha$.

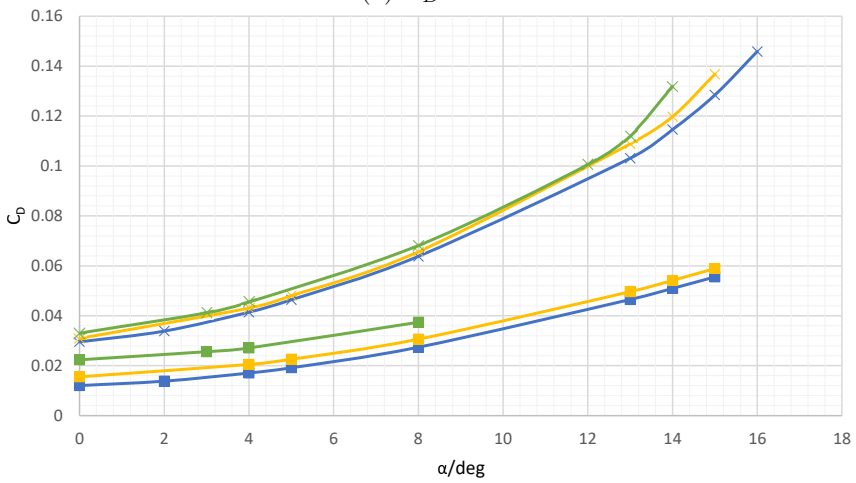

(b) $C_D - \alpha$.

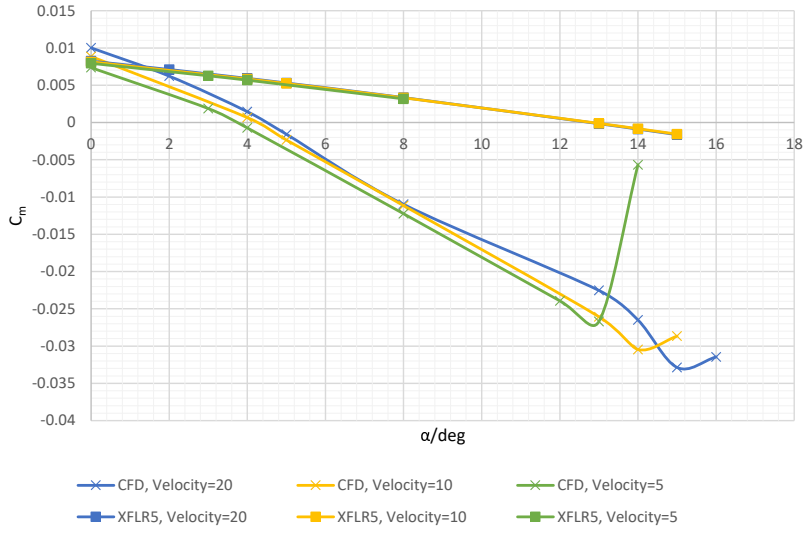

(c) $C_D - \alpha$.

Figure C.1: Comparison of $C_L - \alpha$, $C_D - \alpha$, $C_m - \alpha$ at different velocities between CFD and XFLR5.

References

[1] Milestones. https://160.singpost.com/milestones/. Accessed: 2019-04-18. 2

[2] Rapid Response From the Air: Medicines Successfully Delivered using a Parcel Drone in East Africa. https://www.logistics.dhl/global-en/home/press/press-archive/2018/rapid-response-from-the-air-medicines-successfully-delivered-using-a-parcel-drone-in-east-africa.html. Accessed: 2019-04-18. 2

[3] Navy planning to get its own V-22 Osprey fleet. https://www.stripes.com/news/pacific/navy-planning-to-get-its-own-v-22-osprey-fleet-1.336199. Accessed: 2019-04-18. 3

[4] GD Goh, S Agarwala, GL Goh, V Dikshit, SL Sing, and WY Yeong. Additive manufacturing in unmanned aerial vehicles (uavs): Challenges and potential. *Aerospace Science and Technology*, 63:140–151, 2017. 3, 18, 19, 45

[5] Zoran Vasić, Stevan Maksimović, and Dragutin Georgijević. Applied integrated design in composite uav development. *Applied Composite Materials*, pages 1–16, 2017. 3

[6] Chee Kai Chua, Kah Fai Leong, and Chu Sing Lim. *Rapid Prototyping: Principles and Applications2nd Edition (with Companion CD-ROM)*, volume 1. World Scientific Publishing Co Inc, 2003. 3, 12, 16, 19

[7] Yunus Govdeli, Anh Tuan Tran, and Erdal Kayacan. Multiple Modeling and Fuzzy Switching Control of Fixed-Wing VTOL Tilt-Rotor UAV. In *Fuzzy Techniques: Theory and Applications*, pages 270–284, Cham, 2019. Springer International Publishing. 4, 77, 110

[8] Y. Govdeli, S. Muzaffar, R. Raunak, B. Elhadidi, and E. Kayacan. Unsteady Aerodynamic Modeling and Control of Pusher and Tilt-Rotor Quadplane Configurations. In *Aerospace Science and Technology*, under review. 4, 111, 123

[9] Joseph Katz and Allen Plotkin. *Low-Speed Aerodynamics*. Cambridge Aerospace Series. Cambridge University Press, 2 edition, 2001. doi: 10.1017/CBO9780511810329. 4, 22, 72

[10] S. Verling, B. Weibel, M. Boosfeld, K. Alexis, M. Burri, and R. Siegwart. Full Attitude Control of a VTOL tailsitter UAV. In *2016 IEEE International Conference on Robotics and Automation (ICRA)*, pages 3006–3012, May 2016. doi: 10.1109/ICRA.2016.7487466. 4, 22

[11] A. T. Tran, N. Sakamoto, M. Sato, and K. Muraoka. Control augmentation system design for quad-tilt-wing unmanned aerial vehicle via robust output regulation method. *IEEE Transactions on Aerospace and Electronic Systems*, 53(1): 357–369, Feb 2017. ISSN 0018-9251. doi: 10.1109/TAES.2017.2650618. 4, 23, 26, 110

[12] Haiyang Chao, Yongcan Cao, and YangQuan Chen. Autopilots for small fixed-wing unmanned air vehicles: A survey. In *Mechatronics and Automation, 2007. ICMA 2007. International Conference on*, pages 3144–3149. IEEE, 2007. 8

[13] Utku Eren, Anna Prach, Başaran Bahadır Koçer, Saša V Raković, Erdal Kayacan, and Behçet Açıkmeşe. Model predictive control in aerospace systems: Current state and opportunities. *Journal of Guidance, Control, and Dynamics*, 2017. 8

[14] Sheikh Moheed bin Muzaffar. Nonlinear modelling and control of a quadplane. Master's thesis, NTU, 2018. 9, 110

[15] A. S. Saeed, A. B. Younes, S. Islam, J. Dias, L. Seneviratne, and G. Cai. A review on the platform design, dynamic modeling and control of hybrid UAVs. In *2015 International Conference on Unmanned Aircraft Systems (ICUAS)*, pages 806–815, June 2015. doi: 10.1109/ICUAS.2015.7152365. 10, 68

[16] J. A. Bautista, A. Osorio, and R. Lozano. Modeling and analysis of a tricopter/flying-wing convertible uav with tilt-rotors. In *2017 International Conference on Unmanned Aircraft Systems (ICUAS)*, pages 672–681, June 2017. doi: 10.1109/ICUAS.2017.7991502. 10

[17] Andrew J Keane, András Sóbester, and James P Scanlan. *Small Unmanned Fixed-wing Aircraft Design: A Practical Approach*. John Wiley & Sons, 2017. 11, 12

[18] Aeronautics Guide. `https://www.aircraftsystemstech.com/p/fixed-wing-aircraft-fuselage-fuselage.html`. Accessed: 2020-06-14. 11

[19] Thomas Henry Gordon Megson. *Aircraft structures for engineering students*. Butterworth-Heinemann, 2016. 12

[20] Barry Berman. 3-d printing: The new industrial revolution. *Business Horizons*, 55(2):155 – 162, 2012. ISSN 0007-6813. doi: https://doi.org/10.1016/j.bushor.2011.11.003. URL `http://www.sciencedirect.com/science/article/pii/S0007681311001790`. 12

[21] Thomas Campbell, Christopher Williams, Olga Ivanova, and Banning Garrett. Could 3d printing change the world. *Technologies, Potential, and Implications of Additive Manufacturing, Atlantic Council, Washington, DC*, 2011. 12

[22] Seung Ki Moon, Yu En Tan, Jihong Hwang, and Yong-Jin Yoon. Application of 3d printing technology for designing light-weight unmanned aerial vehicle wing structures. *International Journal of Precision Engineering and Manufacturing-Green Technology*, 1(3):223–228, 2014. 16

[23] David Walker and David Liu. *Topology Optimization of an Aircraft Wing*. doi: 10.2514/6.2015-0976. URL `https://arc.aiaa.org/doi/abs/10.2514/6.2015-0976`. 13

[24] D Brackett, I Ashcroft, and R Hague. Topology optimization for additive manufacturing. In *Proceedings of the solid freeform fabrication symposium, Austin, TX*, volume 1, pages 348–362, 2011. 13

[25] Ji-Hong Zhu, Wei-Hong Zhang, and Liang Xia. Topology optimization in aircraft and aerospace structures design. *Archives of Computational Methods in Engineering*, 23(4):595–622, 2016.

[26] C. Emmelmann, P. Sander, J. Kranz, and E. Wycisk. Laser additive manufacturing and bionics: Redefining lightweight design. *Physics Procedia*, 12:364 – 368, 2011. ISSN 1875-3892. doi: https://doi.org/10.1016/j.phpro.2011.03.046. URL `http://www.sciencedirect.com/science/article/pii/S1875389211001258`. Lasers in Manufacturing 2011 - Proceedings of the Sixth International WLT Conference on Lasers in Manufacturing. 13

[27] L. Henderson, T. Glaser, and F. Kuester. Towards bio-inspired structural design of a 3d printable, ballistically deployable, multi-rotor uav. In *2017 IEEE Aerospace Conference*, pages 1–7, 2017. 13

[28] Chris Banfield, James Kidd, and Jamey D. Jacob. *Design and Development of a 3D Printed Unmanned Aerial Vehicle*. doi: 10.2514/6.2016-2029. URL `https://arc.aiaa.org/doi/abs/10.2514/6.2016-2029`. 14, 18

[29] Joseph T Belter and Aaron M Dollar. Strengthening of 3d printed fused deposition manufactured parts using the fill compositing technique. *PloS one*, 10(4), 2015. 14

[30] Stephen J Furst, George Bunget, and Stefan Seelecke. Design and fabrication of a bat-inspired flapping-flight platform using shape memory alloy muscles and joints. *Smart Materials and Structures*, 22(1):014011, 2012. 16

[31] Charles Richter and Hod Lipson. Untethered hovering flapping flight of a 3d-printed mechanical insect. *Artificial life*, 17(2):73–86, 2011. 16

[32] YL Yap and WY Yeong. Shape recovery effect of 3d printed polymeric honeycomb: This paper studies the elastic behaviour of different honeycomb structures produced by polyjet technology. *Virtual and Physical Prototyping*, 10(2):91–99, 2015. 16

[33] Dror Artzi and Ehud Kroll. Lessons from wind tunnel models made by rapid prototyping. In *Proc 50th Israel Annual Conference on Aerospace Sciences*, 2010. 16

[34] GD Kim and YT Oh. A benchmark study on rapid prototyping processes and machines: quantitative comparisons of mechanical properties, accuracy, roughness, speed, and material cost. *Proceedings of the Institution of Mechanical Engineers, Part B: Journal of Engineering Manufacture*, 222(2):201–215, 2008. 16

[35] Robert C Michelson and Steven Reece. Update on flapping wing micro air vehicle research-ongoing work to develop a flapping wing, crawling entomopter. In *13th Bristol International RPV/UAV Systems Conference Proceedings, Bristol England*, volume 30, pages 30–1, 1998. 16

[36] L Jyothish Kumar and CG Krishnadas Nair. Current trends of additive man-

ufacturing in the aerospace industry. In *Advances in 3D Printing & Additive Manufacturing Technologies*, pages 39–54. Springer, 2017. 16

[37] Mario Ferraro, Andrew Lock, James P Scanlan, and Andy J Keane. Design and flight test of a civil unmanned aerial vehicle for maritime patrol: the use of 3d-printed structural components. 2014. 16

[38] Daniel Kuehme, Nicholas R. Alley, Caleb Phillips, and Bruce R. Cogan. *Flight Test Evaluation and System Identification of the Area-I Prototype-Technology-Evaluation Research Aircraft (PTERA)*. doi: 10.2514/6.2014-2577. URL `https://arc.aiaa.org/doi/abs/10.2514/6.2014-2577`. 16

[39] R Udroiu and LA Mihail. Experimental determination of surface roughness of parts obtained by rapid prototyping. In *8th WSEAS International Conference on Circuits, Systems, Electronics, Control and Signal Processing, Puerto De La Cruz, Tenerife, Canary Islands, Spain*, pages 283–286, 2009. 16

[40] Pete Mangum, Zachary Fisher, K Daniel Cooksey, Dimitri Mavris, Eric Spero, and John W Gerdes. An automated approach to the design of small aerial systems using rapid manufacturing. In *ASME 2015 International Design Engineering Technical Conferences and Computers and Information in Engineering Conference*, pages V02BT03A042–V02BT03A042. American Society of Mechanical Engineers, 2015. 16

[41] Ashu Garg, Anirban Bhattacharya, and Ajay Batish. Chemical vapor treatment of abs parts built by fdm: Analysis of surface finish and mechanical strength. *The International Journal of Advanced Manufacturing Technology*, 89(5-8):2175–2191, 2017. 16

[42] Suraj Ravindrababu, Yunus Govdeli, Zhuo Wei Wong, and Erdal Kayacan. Evaluation of the influence of build and print orientations of unmanned aerial

vehicle parts fabricated using fused deposition modeling process. *Journal of Manufacturing Processes*, 34:659 – 666, 2018. ISSN 1526-6125. doi: https://doi.org/10.1016/j.jmapro.2018.07.007. URL `http://www.sciencedirect.com/science/article/pii/S1526612518308764`. 16

[43] Steven Easter, Jonathan Turman, David Sheffler, Michael Balazs, and Jonathan Rotner. Using advanced manufacturing to produce unmanned aerial vehicles: a feasibility study. *SPIE Defense, Security, and Sensing, International Society for Optics and Photonics*, pages 874204–874204, 2013.

[44] Biranchi N Panda, K Shankhwar, Akhil Garg, and Zhang Jian. Performance evaluation of warping characteristic of fused deposition modelling process. *The International Journal of Advanced Manufacturing Technology*, 88(5-8):1799–1811, 2017. 17

[45] Stefan Junk and Werner Schröder. Application of sustainable design in additive manufacturing of an unmanned aerial vehicle. In *Sustainable Design and Manufacturing 2016*, pages 375–385. Springer, 2016. 17

[46] Tao Zhang, Chaoying Zhou, and Steven Su. Design and development of bio-inspired flapping wing aerial vehicles. In *Advanced Robotics and Intelligent Systems (ARIS), 2015 International Conference on*, pages 1–6. IEEE, 2015. 17

[47] Jean-Pierre Kruth, Ben Vandenbroucke, v J Vaerenbergh, and Peter Mercelis. Benchmarking of different sls/slm processes as rapid manufacturing techniques. 2005. 17

[48] William E Frazier. Metal additive manufacturing: a review. *Journal of Materials Engineering and Performance*, 23(6):1917–1928, 2014. 17

[49] Yuwei Zhai, Diana A Lados, and Jane L LaGoy. Additive manufacturing: making imagination the major limitation. *Jom*, 66(5):808–816, 2014.

[50] Donald A Klosterman, Richard P Chartoff, Brian Priore, Nora Osborne, George Graves, Allan Lightman, Sung S Pak, and Jerry Weaver. Structural Composites via Laminated Object Manufacturing (LOM). In *1996 International Solid Freeform Fabrication Symposium*, 1996. 17

[51] Ruzy Haryati Hambali, HK Celik, PC Smith, AEW Rennie, and M Ucar. Effect of build orientation on fdm parts: a case study for validation of deformation behaviour by fea. In *IN: Proceedings of iDECON 2010—international conference on design and concurrent engineering, Universiti Teknikal Malaysia Melaka, Melaka*, pages 224–228, 2010. 18, 21

[52] Sung-Hoon Ahn, Michael Montero, Dan Odell, Shad Roundy, and Paul K Wright. Anisotropic material properties of fused deposition modeling abs. *Rapid prototyping journal*, 8(4):248–257, 2002. 18

[53] Jingchao Jiang, Jonathan Stringer, and Xun Xu. Support Optimization for Flat Features via Path Planning in Additive Manufacturing. *3D Printing and Additive Manufacturing*, 6(3):171–179, 2019. doi: 10.1089/3dp.2017.0124. URL `https://doi.org/10.1089/3dp.2017.0124`. 18

[54] Helge Klippstein, Alejandro Diaz De Cerio Sanchez, Hany Hassanin, Yahya Zweiri, and Lakmal Seneviratne. Fused deposition modeling for unmanned aerial vehicles (uavs): A review. *Advanced Engineering Materials*, 20(2):1700552, 2018. doi: 10.1002/adem.201700552. URL `https://onlinelibrary.wiley.com/doi/abs/10.1002/adem.201700552`. 18

[55] Maksimov, Peter, Smetannikov, Oleg, Dubrovskaya, Aleksandra, Dongauzer, Konstantin, and Bushuev, Leonid. Numeric simulation of aircraft engine parts additive manufacturing process. *MATEC Web Conf.*, 224:01065, 2018. doi:

10.1051/matecconf/201822401065. URL https://doi.org/10.1051/matecconf/201822401065. 18

[56] Yunus Govdeli, Zhuo Wei Wong, and Erdal Kayacan. Additive manufacturing of unmanned aerial vehicles: current status, recent advances, and future perspectives. In *Proceedings of 2nd International Conference on PRO-AM Progress in Additive Manufacturing*, 2016. 18

[57] S Agarwala, G L Goh, and W Y Yeong. Optimizing aerosol jet printing process of silver ink for printed electronics. *IOP Conference Series: Materials Science and Engineering*, 191, 2017. doi: 10.1088/1757-899x/191/1/012027. 19

[58] Ker Chin Ang, Kah Fai Leong, Chee Kai Chua, and Margam Chandrasekaran. Investigation of the mechanical properties and porosity relationships in fused deposition modelling-fabricated porous structures. *Rapid Prototyping Journal*, 12(2):100–105, 2006. 21

[59] Candice Majewski and Neil Hopkinson. Effect of section thickness and build orientation on tensile properties and material characteristics of laser sintered nylon-12 parts. *Rapid Prototyping Journal*, 17(3):176–180, 2011. 21

[60] Wenzheng Wu, Peng Geng, Guiwei Li, Di Zhao, Haibo Zhang, and Ji Zhao. Influence of layer thickness and raster angle on the mechanical properties of 3d-printed peek and a comparative mechanical study between peek and abs. *Materials*, 8 (9):5834–5846, 2015. 21

[61] Behzad Rankouhi, Sina Javadpour, Fereidoon Delfanian, and Todd Letcher. Failure analysis and mechanical characterization of 3d printed abs with respect to layer thickness and orientation. *Journal of Failure Analysis and Prevention*, 16 (3):467–481, 2016. 21

[62] F Xu, HT Loh, and YS Wong. Considerations and selection of optimal orientation for different rapid prototyping systems. *Rapid Prototyping Journal*, 5(2):54–60, 1999. 21

[63] MS Uddin, MFR Sidek, MA Faizal, Reza Ghomashchi, and Alokesh Pramanik. Evaluating mechanical properties and failure mechanisms of fused deposition modeling acrylonitrile butadiene styrene parts. *Journal of Manufacturing Science and Engineering*, 139(8):081018, 2017. 21

[64] Anna Bellini and Selçuk Güçeri. Mechanical characterization of parts fabricated using fused deposition modeling. *Rapid Prototyping Journal*, 9(4):252–264, 2003. 21

[65] Miquel Domingo-Espin, Josep M Puigoriol-Forcada, Andres-Amador Garcia-Granada, Jordi Lluma, Salvador Borros, and Guillermo Reyes. Mechanical property characterization and simulation of fused deposition modeling polycarbonate parts. *Materials & Design*, 83:670–677, 2015. 21

[66] A Sherif El-Gizawy, Shan Corl, and Brian Graybill. Process-induced properties of fdm products. In *Proceedings of the ICMET, International Conference on Mechanical Engineerings and Technology Congress & Exposition*, 2011. 21

[67] Hui Zhou, Ping Xu, Suchao Xie, Zhejun Feng, and Da Wang. Mechanical performance and energy absorption properties of structures combining two nomex honeycombs. *Composite Structures*, 185:524 – 536, 2018. ISSN 0263-8223. doi: https://doi.org/10.1016/j.compstruct.2017.11.059. URL `http://www.sciencedirect.com/science/article/pii/S0263822317319207`. 14, 48

[68] A-J Wang and DL McDowell. In-plane stiffness and yield strength of periodic metal honeycombs. *Journal of engineering materials and technology*, 126(2):137–156, 2004. 14, 15

[69] Lorna J. Gibson and Michael F. Ashby. *Cellular Solids: Structure and Properties*. Cambridge Solid State Science Series. Cambridge University Press, 2 edition, 1997. doi: 10.1017/CBO9781139878326. 14, 15, 46

[70] Jai-Hwang Joo and Ki-Ju Kang. Stability assessments of single-layered space frames. In *International Conference on Sustainable Building Asia SB10*, pages 299–304, 2010. 15

[71] MJAM Walters, MGD Geers, J Wismans, WJ Witteman, and FHM Swartjes. *Designing and Analysing Kagome Structures for Crash Safety Applications*. Technische Universiteit Eindhoven, 2005. 15

[72] Jing Ming Low. Internal Structure Design and Manufacturing of 3D-Printed Unmanned Aerial Vehicle. Master's thesis, NTU, 2018. 15, 47, 48, 146

[73] Bai gang Mi, Hao Zhan, and Si si Lu. An extended unsteady aerodynamic model at high angles of attack. *Aerospace Science and Technology*, 77:788 – 801, 2018. ISSN 1270-9638. doi: https://doi.org/10.1016/j.ast.2018.03.035. 22

[74] Ertugrul Cetinsoy, Cevdet Hancer, Kaan T. Oner, Efe Sirimoglu, and Mustafa Unel. Aerodynamic Design and Characterization of a Quad Tilt-Wing UAV via Wind Tunnel Tests. *Journal of Aerospace Engineering*, 25(4):574–587, 2012. doi: 10.1061/(ASCE)AS.1943-5525.0000161. 22

[75] B. Yuksek, A. Vuruskan, U. Ozdemir, M. A. Yukselen, and G. Inalhan. Transition Flight Modeling of a Fixed-Wing VTOL UAV. *Journal of Intelligent & Robotic Systems*, 84(1):83–105, Dec 2016. ISSN 1573-0409. doi: 10.1007/s10846-015-0325-9. 22, 26, 60

[76] Kristoffer Gryte. High Angle of Attack Landing of an Unmanned Aerial Vehicle. Master's thesis, NTNU, 2015. 22

[77] Randal W Beard and Timothy W McLain. *Small unmanned aircraft: Theory and practice*. Princeton university press, 2012. 22

[78] Masayuki Sato, Koji Muraoka, and Koki Hozumi. Flight control design and demonstration of unmanned airplane for radiation monitoring system. *IFAC Proceedings Volumes*, 47(3):2527–2532, 2014. 22, 23, 26, 78, 110

[79] Jubaraj Sahu. Parallel CFD Simulations of Unsteady Control Maneuver Aerodynamics. In *Parallel Computational Fluid Dynamics 2007*, pages 417–424, Berlin, Heidelberg, 2009. Springer Berlin Heidelberg. ISBN 978-3-540-92744-0. 22

[80] Kai Zhou and Chao Zhou. Unsteady effects of vortex interaction on tip leakage vortex breakdown and its loss mechanism. *Aerospace Science and Technology*, 82-83:363 – 371, 2018. ISSN 1270-9638. doi: https://doi.org/10.1016/j.ast.2018.09.019. 22

[81] Si Chen, Hao Li, Shijun Guo, Mingbo Tong, and Bing Ji. Unsteady aerodynamic model of flexible flapping wing. *Aerospace Science and Technology*, 80:354 – 367, 2018. ISSN 1270-9638. doi: https://doi.org/10.1016/j.ast.2018.07.017. 22

[82] Michael S Vest and Joseph Katz. Unsteady Aerodynamic Model of Flapping Wings. *AIAA journal*, 34(7):1435–1440, 1996. 22

[83] Jian feng Tan and Hao wen Wang. Simulating unsteady aerodynamics of helicopter rotor with panel/viscous vortex particle method. *Aerospace Science and Technology*, 30(1):255 – 268, 2013. ISSN 1270-9638. doi: https://doi.org/10.1016/j.ast.2013.08.010. 22

[84] A. Oosedo, S. Abiko, A. Konno, T. Koizumi, T. Furui, and M. Uchiyama. Development of a quad rotor tail-sitter VTOL UAV without control surfaces and experimental verification. In *2013 IEEE International Conference on Robotics*

and Automation, pages 317–322, May 2013. doi: 10.1109/ICRA.2013.6630594. 23

[85] A. Bhanja Chowdhury, A. Kulhare, and G. Raina. A generalized control method for a Tilt-rotor UAV stabilization. In *2012 IEEE International Conference on Cyber Technology in Automation, Control, and Intelligent Systems (CYBER)*, pages 309–314, May 2012. doi: 10.1109/CYBER.2012.6392571. 23

[86] Zhiwei Kong and Qiang Lu. Mathematical Modeling and Modal Switching Control of a Novel Tiltrotor UAV. *Journal of Robotics*, 2018, 2018. 23

[87] Satoshi Suzuki, Ren Zhijia, Yoshikazu Horita, Kenzo Nonami, Gaku Kimura, Toshio Bando, Daisuke Hirabayashi, Mituhiro Furuya, and Kenta Yasuda. Attitude control of quad rotors qtw-uav with tilt wing mechanism. *Journal of System Design and Dynamics*, 4(3):416–428, 2010. 23, 26

[88] Tengfei Guo, Honglun Wang, and Wendong Gai. Transition flight control for Canard Rotor/Wing rotorcraft. In *2011 2nd International Conference on Artificial Intelligence, Management Science and Electronic Commerce (AIMSEC)*, pages 875–880, Aug 2011. doi: 10.1109/AIMSEC.2011.6010405. 23

[89] Giuseppe Notarstefano and John Hauser. Modeling and Dynamic Exploration of a Tilt-Rotor VTOL Aircraft. *IFAC Proceedings Volumes*, 43(14):119 – 124, 2010. ISSN 1474-6670. doi: https://doi.org/10.3182/20100901-3-IT-2016.00182. 8th IFAC Symposium on Nonlinear Control Systems. 23

[90] X. Lyu, H. Gu, J. Zhou, Z. Li, S. Shen, and F. Zhang. A hierarchical control approach for a quadrotor tail-sitter VTOL UAV and experimental verification. In *2017 IEEE/RSJ International Conference on Intelligent Robots and Systems (IROS)*, pages 5135–5141, Sep. 2017. doi: 10.1109/IROS.2017.8206400. 23

[91] Jeffrey J Dickeson, David Miles, Oguzhan Cifdaloz, Valana L Wells, and Armando A Rodriguez. Robust lpv h∞ gain-scheduled hover-to-cruise conversion for a tilt-wing rotorcraft in the presence of cg variations. In *Decision and Control, 2007 46th IEEE Conference on*, pages 2773–2778. IEEE, 2007. 23

[92] Wei Zhao and Craig Underwood. Robust transition control of a martian coaxial tiltrotor aerobot. *Acta Astronautica*, 99:111–129, 2014. 23

[93] Farid Kendoul, Isabelle Fantoni, and Rogelio Lozano. Modeling and control of a small autonomous aircraft having two tilting rotors. *IEEE Transactions on Robotics*, 22(6):1297–1302, 2006. 24

[94] Sergio Salazar-Cruz, Farid Kendoul, Rogelio Lozano, and Isabelle Fantoni. Real-time stabilization of a small three-rotor aircraft. *IEEE Transactions on aerospace and electronic systems*, 44(2), 2008. 24

[95] Cheng Peng, Xin Min Wang, and Xiao Chen. Design of tiltrotor flight control system in conversion mode using improved neutral network pid. In *Advanced Materials Research*, volume 850, pages 640–643. Trans Tech Publ, 2014. 24

[96] Rolf T Rysdyk and Anthony J Calise. Adaptive model inversion flight control for tilt-rotor aircraft. *Journal of Guidance Control and Dynamics*, 22:402–407, 1999. 24

[97] Changjie Yu, Jihong Zhu, and Zengqi Sun. Nonlinear adaptive internal model control using neural networks for tilt rotor aircraft platform. In *Soft Computing in Industrial Applications, 2005. SMCia/05. Proceedings of the 2005 IEEE Mid-Summer Workshop on*, pages 12–16. IEEE, 2005. 24

[98] Boo-Min Kim, Kwangchan Choi, and Byoung Soo Kim. Trajectory tracking controller design using neural networks for tiltrotor uav. In *AIAA Guidance, Navigation and Control Conference and Exhibit*, pages 20–23, 2007. 24

[99] Oscar Castillo, Leticia Cervantes, Jose Soria, Mauricio Sanchez, and Juan R. Castro. A generalized type-2 fuzzy granular approach with applications to aerospace. *Information Sciences*, 354:165 – 177, 2016. ISSN 0020-0255. doi: https://doi.org/10.1016/j.ins.2016.03.001. 24

[100] Kevin Tai, Abdul-Rahman El-Sayed, Mohammad Biglarbegian, Claudia Gonzalez, Oscar Castillo, and Shohel Mahmud. Review of recent type-2 fuzzy controller applications. *Algorithms*, 9(2):39, 2016. 24

[101] Erdal Kayacan and Mojtaba Ahmadieh Khanesar. *Fuzzy neural networks for real time control applications: concepts, modeling and algorithms for fast learning.* Butterworth-Heinemann, 2015. 24, 96, 97, 98, 103

[102] E. Kayacan, O. Cigdem, and O. Kaynak. Sliding Mode Control Approach for Online Learning as Applied to Type-2 Fuzzy Neural Networks and Its Experimental Evaluation. *IEEE Transactions on Industrial Electronics*, 59(9):3510–3520, Sep. 2012. ISSN 0278-0046. doi: 10.1109/TIE.2011.2182017. 24

[103] R. Maslim, H. Chaoyi, Z. Yixi, J. Linhao, B. B. Kocer, and E. Kayacan. Performance evaluation of adaptive and nonadaptive fuzzy structures for 4D trajectory tracking of quadrotors: A comparative study. In *2015 IEEE International Conference on Fuzzy Systems (FUZZ-IEEE)*, pages 1–7, Aug 2015. doi: 10.1109/FUZZ-IEEE.2015.7337945. 24, 113

[104] Christos Papachristos, Kostas Alexis, and Anthony Tzes. Model predictive hovering-translation control of an unmanned tri-tiltrotor. In *Robotics and Automation (ICRA), 2013 IEEE International Conference on*, pages 5425–5432. IEEE, 2013. 26

[105] Ertuğrul Çetinsoy, Serhat Dikyar, Cevdet Hançer, KT Oner, E Sirimoglu, M Unel,

and MF Aksit. Design and construction of a novel quad tilt-wing uav. *Mechatronics*, 22(6):723–745, 2012. 26

[106] Walter Castro Smith and Richard W Dean. Structural characteristics of fused deposition modeling polycarbonate material. *Polymer testing*, 32(8):1306–1312, 2013. 29

[107] Bin Huang and Sarat Singamneni. Raster angle mechanics in fused deposition modelling. *Journal of Composite Materials*, 49(3):363–383, 2015. 30

[108] Jun Du, Zhengying Wei, Xin Wang, Jijie Wang, and Zhen Chen. An improved fused deposition modeling process for forming large-size thin-walled parts. *Journal of Materials Processing Technology*, 234:332–341, 2016. 33

[109] Sarat Singamneni, Asimava Roychoudhury, Olaf Diegel, and Bin Huang. Modeling and evaluation of curved layer fused deposition. *Journal of Materials Processing Technology*, 212(1):27–35, 2012. 35

[110] Bin Huang and Sarat Singamneni. Curved layer fused deposition modeling with varying raster orientations. In *Applied Mechanics and Materials*, volume 446, pages 263–269. Trans Tech Publ, 2014.

[111] D Adams and CJ Turner. An implicit slicing method for additive manufacturing processes. *Virtual and Physical Prototyping*, pages 1–6, 2017. 35

[112] Michael Dawoud, Iman Taha, and Samy J Ebeid. Mechanical behaviour of abs: An experimental study using fdm and injection moulding techniques. *Journal of Manufacturing Processes*, 21:39–45, 2016. 37

[113] Chun-Li Lin, Jian-Hong Yu, Heng-Liang Liu, Chih-Hao Lin, and Yang-Sung Lin. Evaluation of contributions of orthodontic mini-screw design factors based on fe

analysis and the taguchi method. *Journal of biomechanics*, 43(11):2174–2181, 2010. 38

[114] Turgay Kıvak. Optimization of surface roughness and flank wear using the taguchi method in milling of hadfield steel with pvd and cvd coated inserts. *Measurement*, 50:19–28, 2014. 38

[115] David Locascio, Coline Ramee, Eric Schaus, Kenneth D Cooksey, Eric Spero, and Dimitri N Mavris. A framework for integrated analysis, design, and rapid prototyping of small unmanned airplanes. In *16th AIAA Aviation Technology, Integration, and Operations Conference*, page 3447, 2016. 40

[116] F Hürlimann, R Kelm, M Dugas, and G Kress. Investigation of local load introduction methods in aircraft pre-design. *Aerospace Science and Technology*, 21(1): 31–40, 2012. 40

[117] Dassault Systèmes. Abaqus analysis user's manual. *Simulia Corp. Providence, RI, USA*, 2007. 40

[118] International Standard ISO 1209-1. Rigid cellular plastics - Determination of flexural properties- part : Basic bending test. *International Standard ISO Reference number ISO 1209-1:2007(E)*, 2007. 45

[119] Jing Ming Low, Yunus Govdeli, Suraj Ravindrababu, and Erdal Kayacan. On the comparison of diamond honeycomb and 3d-kagome structures for 3d printed uavs. In *Proceedings of 3rd International Conference on PRO-AM Progress in Additive Manufacturing*, 2018. 49, 50, 51, 52, 147

[120] Marcello R Napolitano. *Aircraft dynamics: From modeling to simulation*. J. Wiley, 2012. 56, 57, 58

[121] Wayne Johnson. *Rotorcraft Aeromechanics*. Cambridge Aerospace Series. Cambridge University Press, 2013. doi: 10.1017/CBO9781139235655. 64

[122] Hung D Nguyen, Liu Yu, and Koichi Mori. Aerodynamic characteristics of quadrotor helicopter. In *AIAA Flight Testing Conference*, page 3141, 2017. 64, 66

[123] PB Sujit, Srikanth Saripalli, and Joao Borges Sousa. Unmanned aerial vehicle path following: A survey and analysis of algorithms for fixed-wing unmanned aerial vehicles. *IEEE Control Systems*, 34(1):42–59, 2014. 94

[124] E. Kayacan and R. Maslim. Type-2 Fuzzy Logic Trajectory Tracking Control of Quadrotor VTOL Aircraft With Elliptic Membership Functions. *IEEE/ASME Transactions on Mechatronics*, 22(1):339–348, Feb 2017. ISSN 1083-4435. doi: 10.1109/TMECH.2016.2614672. 95

[125] Erdal Kayacan, Mojtaba Ahmadieh Khanesar, Jaime Rubio-Hervas, and Mahmut Reyhanoglu. Learning control of fixed-wing unmanned aerial vehicles using fuzzy neural networks. *International Journal of Aerospace Engineering*, 2017, 2017. 97

[126] VI Utkin. Sliding modes in optimization and control problems, 1992. 98

[127] Swati Swarnkar, Hardik Parwana, Mangal Kothari, and Abhishek Abhishek. Biplane-Quadrotor Tail-Sitter UAV: Flight Dynamics and Control. *Journal of Guidance, Control, and Dynamics*, 41(5):1049–1067, 2018. 110

[128] Raunak Raj. Modelling and controller design for tilt quadplane. Master's thesis, NTU, 2018. 110

[129] Y. Govdeli, S. Muzaffar, R. Raunak, B. Elhadidi, and E. Kayacan. Learning Control of Tandem-Wing Tilt-Rotor UAV with Unsteady Aerodynamic Model. In *2019 IEEE International Conference on Fuzzy Systems (FUZZ-IEEE)*, in press. 123

[130] Robert C Nelson. *Flight stability and automatic control*, volume 2. WCB/McGraw Hill New York, 1998. 142

[131] Karl Nickel and Michael Wohlfahrt. *Tailless aircraft in theory and practice*. Amer Inst of Aeronautics &, 1994. 142

[132] Eastman N Jacobs and Robert M Pinkerton. Tests in the variable-density wind tunnel of related airfoils having the maximum camber unusually far forward. 1936. 142

[133] André Deperrois. XFLR5 Analysis of foils and wings operating at low Reynolds numbers. *Guidelines for XFLR5*, 2009. 142

[134] Daveena Raju Kripalani. Wind Tunnel Testing of a 3D Printed Flying Wing VTOL UAV. Master's thesis, NTU, 2018. 149, 151, 152

[135] Jewel B Barlow, William H Rae Jr, and Alan Pope. *Low speed wind tunnel testing*, volume 3. Wiley, 1999. 150, 151